CFD in support of development and optimization of the MIT LEU fuel element design

by

Mihai Aurelian Diaconeasa

B.Sc. Mathematics, Physics, Chemistry, University College Utrecht, 2010

SUBMITTED TO THE DEPARTMENT OF NUCLEAR SCIENCE AND ENGINEERING IN PARTIAL FULFILLMENT OF THE REQUIREMENTS FOR THE DEGREE OF

MASTER OF SCIENCE IN NUCLEAR SCIENCE AND ENGINEERING
AT THE
MASSACHUSETTS INSTITUTE OF TECHNOLOGY

SEPTEMBER 2014

Signature redacted

Signature of Author: _____
Department of Nuclear Science and Engineering
August 7, 2014

Signature redacted

Certified by: _____
Emilio Baglietto
Assistant Professor of Nuclear Science and Engineering
Thesis Supervisor

Signature redacted

Certified by: _____
Lin-wen Hu
Associate Director of Research Development and Utilization at the NRL
Thesis Supervisor

Signature redacted

Accepted by: _____
Mujid S. Kazimi
TEPCO Professor of Nuclear Engineering
Chairman, Committee for Graduate Studies

CFD in support of development and optimization of the MIT LEU fuel element design

by

Mihai Aurelian Diaconeasa

Submitted to the Department of Nuclear Science and Engineering
on August 7, 2014 in Partial Fulfillment of the Requirements for the
Degree of Master of Science in Nuclear Science and Engineering

ABSTRACT

The effect of lateral power distribution of the MITR LEU fuel design was analyzed using Computational Fluid Dynamics. Coupled conduction and convective heat transfer were modeled for uniform and non-uniform lateral power distributions. It was concluded that, due to conduction, the maximum heat flux ratio on the cladding surface is 1.16, compared to the maximum volumetric power generation ratio of 1.23. The maximum cladding temperature occurs roughly 0.5 inches from the edge of the support plate, while the peak volumetric power generation is located at the end of the fuel meat, about 0.1 inches from the edge of the support plate. Although the heat transfer coefficient is lower in the corner of the coolant channel, this has a negligible effect on the peak cladding temperature, i.e. the peak cladding temperature is related to heat flux only and a "channel average" heat transfer coefficient can be adopted. Moreover, coolant temperatures in the radial direction are reasonably uniform, which is indicative of good lateral mixing. Finally, a quasi-DNS study has been performed to analyze the effect of the fuel grooves on the local heat transfer coefficient. The quasi-DNS results bring useful insights, showing two main effects related to the existence of the grooves. First, the increased surface leads to an increase in the pressure drop and further, the flow aligned configuration of the grooves limits the ability of the near wall turbulent structures to create mixing, leading to a noticeable reduction in the local heat transfer coefficient at the base of the grooves. Overall, this leads to an effective decrease in the local heat transfer coefficient, but due to the increased heat transfer surface the global heat transfer is enhanced in comparison to the flat plate configuration. The improved understanding of the effects of grooves on the local heat transfer phenomena provides a useful contribution to future fuel design considerations. For example, the increase in pressure drop, together with the reduction in the local heat transfer coefficient indicated that the selection of a grooved wall channel instead of a smooth wall channel might not necessarily be optimal, particularly if fabrication issues are taken into account, together with the concern that grooved walls may promote oxide growth and crud formation during the life of the fuel.

Thesis Supervisor: Emilio Baglietto
Title: Assistant Professor of Nuclear Science and Engineering

Thesis Supervisor: Lin-wen Hu
Title: Associate Director of Research Development and Utilization at the NRL

Acknowledgments

I would like to express my gratitude to my supervisor, Prof. Emilio Baglietto, for the many hours spent guiding and teaching me to critically analyze my results. Also, his cluster proved pivotal in completing the second part of the thesis in a reasonable and timely manner.

Furthermore, I would also like to thank Dr. Lin-wen Hu, my other supervisor, for her availability, advice and constructive review of the thesis.

Also, I would like to acknowledge Dr. Koroush Shirvan for his assistance with running the STAR-CCM+ code.

I deeply appreciate the support and feedback of the CFD group and, in particular, for their patience in accommodating the many nodes on the cluster that I needed to run my long simulations. It was an arduous task and their patience made it possible.

In addition, I would like to mention that this work was sponsored by the U.S. Department of Energy, National Nuclear Security Administration Office of Global Threat Reduction.

Finally, I would like to thank my wife for helping me find strength in the most critical moments and for her constant source of inspiration through endless constructive discussions.

Table of Contents

List of Figures

List of Tables

1. Introduction

In 1978 the U.S. Department of Energy (DOE) started the Reduced Enrichment for Research and Test Reactor (RERTR) Program, which targets the development of the required technology to allow the conversion of civilian facilities using high-enriched uranium (HEU – equal or more than 20% U-235) to low-enriched uranium (LEU – less than 20% U-235) fuels. Up to date, over 40 research reactors have already been converted from HEU to LEU fuels and 5 others will be converted by 2016 [1].

The MIT Reactor (MITR) is the second largest university research reactor in the US. It has been operating at 6 MW since November 2010 after the 20-year license renewal authorized by US Nuclear Regulatory Commission. It is a tank-type research reactor that is owned and operated by MIT. The MITR is composed of two concentric tanks: an outer one with heavy water (as reflector), an inner one with light water (as coolant/moderator) and a graphite reflector enclosing the heavy water tank to minimize neutron leakage. The HEU fuel used has a plate-type design cladded with grooved 6061 aluminum alloy material. Fifteen such fuel plates are assembled into a rhomboid-shaped fuel element. The reactor core has a close-packed hexagonal geometry to maximize the thermal neutron flux in the heavy water reflector region. The core region has 27 positions and is nominally loaded with twenty-four rhomboidal fuel elements and three dummy elements or in-core experiments. Six boron-impregnated stainless-steel shim blades and one cadmium regulating rod provide the reactor control (Figure 1.1). A more detailed description of the reactor design including various passive safety features can be found in the MITR Reactor Systems Manual [2].

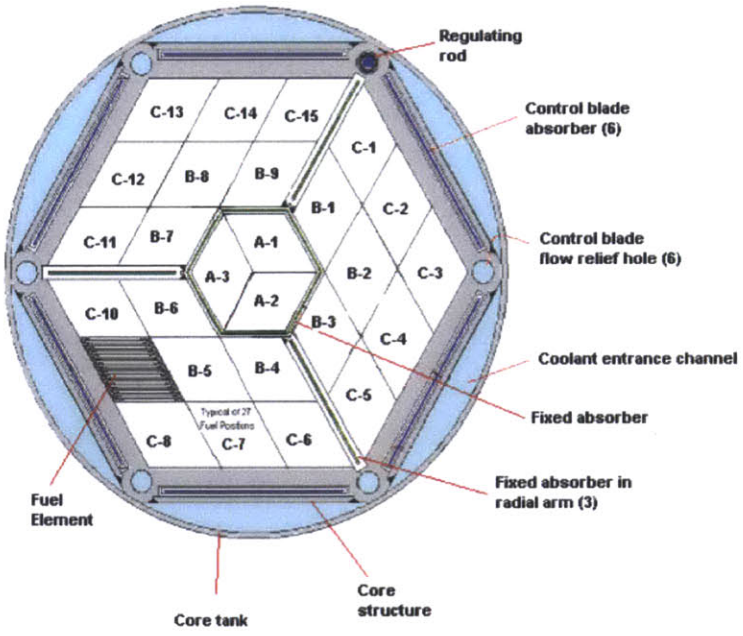

Figure 1.1 MITR Core map showing fuel element position designations and major core structures [2]

The reactor operates at atmospheric pressure with a nominal primary coolant flow rate of 2000 gpm and an average temperature of about 50 °C. The compact hexagonal core structure of about 15 inches across and with an active fuel length of about 23 inches has an average power density of about 80 kW/l. The current HEU fuel plate is designed with longitudinal grooves on the cladding to increase the heat transfer area (Figure 1.2). The unique grooved fuel plate design was adopted in 1970's during the re-design of the MITR-II. The MITR is the only research reactor in the world that uses this unique fuel design.

In the studies performed by Newton [3] on the conversion to LEU fuel at the MITR it was concluded that the conversion is possible if the high density LEU fuel becomes available. The proposed fuel with sufficient uranium density is the monolithic uranium-molybdenum (U-Mo) with molybdenum content of 10%. A new configuration, keeping the same outer fuel element geometry, but with 18 fuel plates, thinner fuel meat and cladding, was evaluated. This design may pose fabrication difficulties (i.e. meet the tolerances required), especially considering the decrease in the thickness of the fuel plate and consequently a decrease in the dimensions of the grooves.

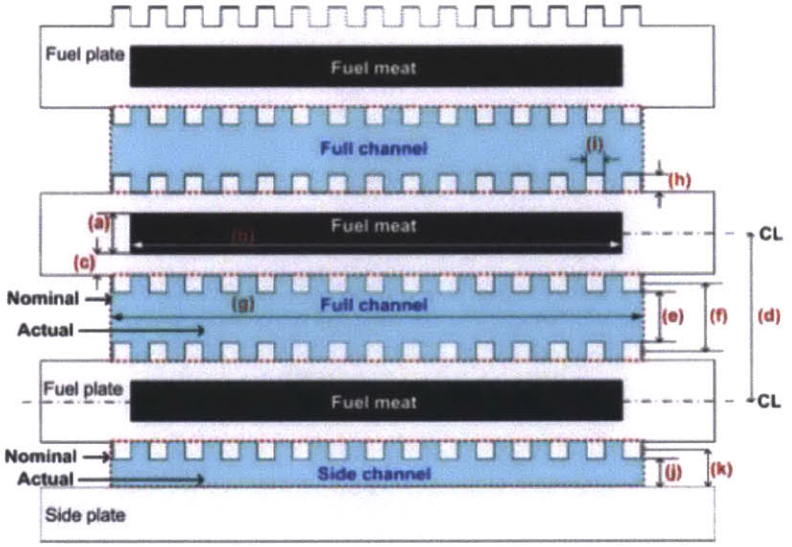

Figure 1.2 Schematic of flow channel configuration of MITR (only 3 fuel plates and 1 supporting plate are shown in the schematic) [4]

Various thermal-hydraulic analyses have been performed for the LEU conversion of the MITR. One of them is the study by Wang [5] in which the PLTEMP/ANL code was used. The program essentially calculates a 2-dimensional temperature solution: a 1-dimensional solution across the fuel element at the entrance region that is repeated for each axial node along the length of the channel. In this study, two approaches were used to model the enhanced heat transfer due to the grooved fuel plates: by employing the Carnavos correlations and by using the Wong's friction factor (obtained exclusively for the MITR [6]), and the Dittus-Boelter correlation with a 1.9 enhancement factor to account for the area of the grooves. This approach may be useful in

determining the safety margins of the reactor, however it lacks the ability to capture three-dimensional local phenomena that are important in the optimization process. Moreover, the 1.9 heat transfer augmentation factor has not been experimentally or computationally validated. As a consequence, a three-dimensional model may prove to be more suitable.

A versatile approach to model three-dimensional fluid flow and heat transfer problems is represented by computational fluid dynamics (CFD). In this work, a commercially available finite-volume (FV) based solver, STAR-CCM+, was used for accurate CFD modeling of the fuel assemblies design.

2. Objectives

Full three-dimensional models have been developed using STAR-CCM+ for thermal-hydraulics analysis with fine axial and lateral nodalization for each fuel plate and coolant channel. As a first approximation, the geometry of the fuel plate was designed without the grooves (i.e. flat plate), in order to save computational time and because of the limited understanding of heat transfer in micro-grooves (this will be part of the next objective). The objective of this task is to model the conduction in the fuel plate and variation in the convective heat transfer rate in the axial and lateral direction of a coolant channel.

For computational efficiency, a minimal unit section has been investigated. It contains the fuel element with two water half-channels enclosing the fuel plate that contains the fuel meat (Figure 2.1). On the free sides of the water channels symmetry boundary conditions shall be imposed and an additional water region will be added under the section in order to capture the entrance effects. It should be noted that periodic boundaries would be more appropriate for the free sides, but sensitivity studies showed no measurable difference when adopting the simpler symmetric boundary.

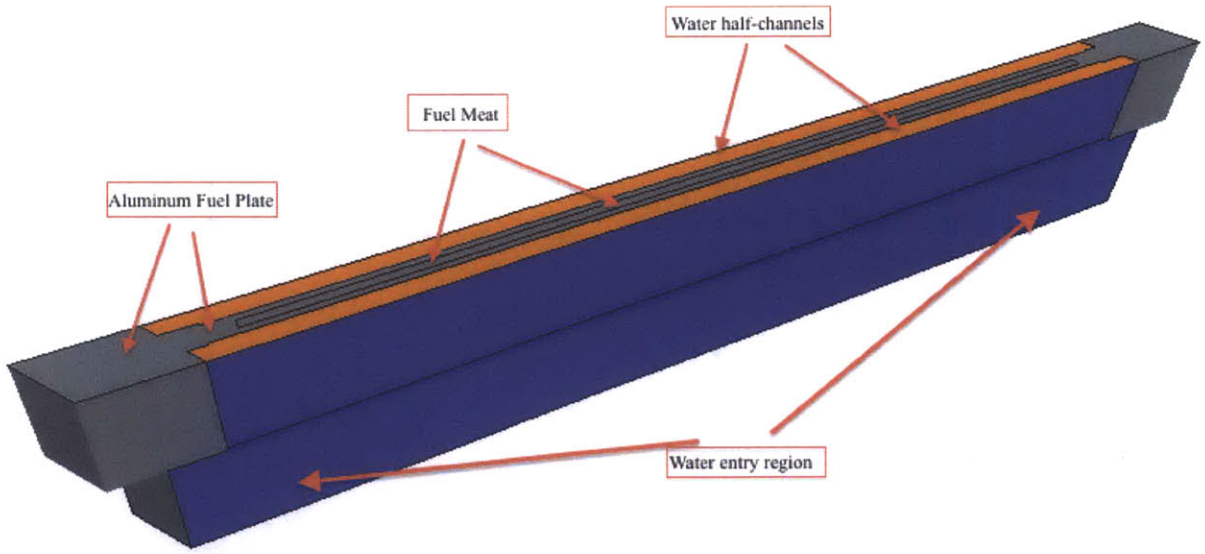

Figure 2.1 Perspective view of the section of the modified (without grooves) flow channel configuration

The actual heating of the system is implemented as a volumetric heat source in the fuel meat region. This represents the most accurate modeling approach and allows the simulation of the correct heat transfer and temperature distributions in the meat, aluminum plate and coolant channels.

The other objective of this project is to study and quantify the effect of the grooves. The MITR fuel element incorporates longitudinal grooves to augment heat transfer. The grooved surface

area is twice that of a flat surface. A study in 1990's by S. Parra concluded that the heat transfer enhancement factor is roughly 90% higher than that of the flat surface, however an empirical correlation predicted lower heat transfer enhancement ~ 60%. Due to the extremely small dimension of the grooves, which is comparable to the viscous sublayer thickness, it is extremely difficult to effectively quantify the heat transfer improvement. The dominant effect is expected to be an increase in the turbulence, which will lead to an increase in the heat transfer; however, its magnitude is uncertain. There is no literature that provides us with detailed quantification of this effect; therefore, a direct numerical simulation approach is the only available alternative to high accuracy experiments.

The STAR-CCM+ (v. 8.06) code was used to simulate in a quasi-DNS[1] fashion the effect of the grooves. The approach in completing this task is two-fold: 1. first, perform a quasi-DNS calculation of a smooth channel flow and validate it against known databases; 2. finally, run a quasi-DNS calculation of the grooved channel flow and compare it to the smooth channel flow case.

[1] See the last paragraph on page 21 for a discussion on the definition of "quasi-DNS".

3. Numerical Methods and Discretization Schemes

3.1 Governing Equations

The most general form of the Navier-Stokes equations for continuity and momentum in continuous integral form solved in STAR-CCM+ is given below:

$$\frac{\partial}{\partial t}\int_V \rho\chi\, dV + \oint_A \rho(\vec{v}-\vec{v}_g)d\vec{a} = \int_V S_u\, dV \tag{3.1}$$

$$\frac{\partial}{\partial t}\int_V \rho\chi\vec{v}\, dV + \oint_A \rho\vec{v}\otimes(\vec{v}-\vec{v}_g)d\vec{a} = -\oint_A p\vec{I}\, d\vec{a} + \oint_A \vec{T}\, d\vec{a} + \int_V \left(\vec{f}_r + \vec{f}_g + \vec{f}_p + \vec{f}_u + \vec{f}_\omega\right)dV \tag{3.2}$$

In eq. (3.1) the terms, from left to right, are the transient term, the convective flux and, respectively, the volumetric source term. In eq. (3.2), following the same direction, the following terms are present: the transient term, the convective flux, the pressure gradient term, the viscous flux and the body force terms.

3.2 Solution Algorithms

While CFD is an extremely powerful simulation technique, its rigorous applications requires verification of the accuracy of the numerical and modeling methods. In this work, scrupulous sensitivities to all discretization, solution and modeling approaches have been performed to guarantee the quality of the simulations. The general approach of this technique is briefly discussed here.

First, the spatial solution domain is subdivided into a finite number of contiguous control volumes (CV) that can be of an arbitrary shape. STAR-CCM+ provides methods for generating different types of grids: tetrahedral, polyhedral or trimmed hexahedral. The selection of a specific type of grid depends on the specific geometrical and flow configurations and may change even from one component to another (e.g. for large aspect ratio geometries). In our models, hexahedral dominant meshes offer optimal discretization and have, therefore, been used throughout the work.

The accuracy of the finite-volume solution is strongly related to the manner in which the flow equations are discretized and solved. STAR-CCM+ employs methodologies that are based on the extensive work of Ferziger and Peric [7]. All approximations, including time and space discretization used in this work are consistently of second-order accuracy. The solution of the resulting algebraic system of equations is accomplished using a segregated iterative method based on the original SIMPLE algorithm. The linearized momentum equations are solved first, after which the pressure-correction equation is solved, and finally the temperature and turbulence quantities are solved.

STAR-CCM+ uses the semi-implicit method for the pressure-linked equations (i.e. SIMPLE algorithm) to control the overall solution (Figure 3.1). Until convergence, for each solution update the following steps are executed:

- first, the boundary conditions are set
- the reconstruction gradients of velocity and pressure are calculated
- the velocity and pressure gradients are computed
- the discretized momentum equation is solved in order to create the intermediate velocity field
- the uncorrected mass fluxes at faces are computed
- the pressure correction equation is solved to obtain the cell values of the pressure correction and to update the pressure field (at this step the under-relaxation factor is used to add only a portion of the pressure correction to the previous iteration in order to improve the convergence)
- the boundary pressure corrections are updated
- the face mass fluxes are corrected
- finally, the cell velocities are corrected.

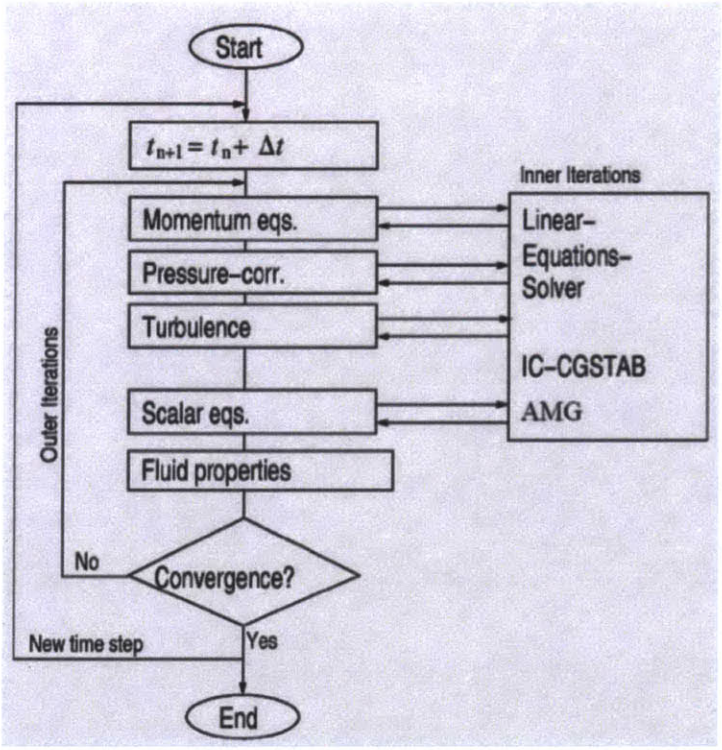

Figure 3.1 The SIMPLE scheme is embedded in an iterative flow solver

While the consistency in the accuracy of the numerical and solution schemes is a fundamental component in the prediction of accurate heat transfer, the other fundamental component is the

adequacy of the turbulence modeling. The extensive work of Baglietto [8] regarding turbulence modeling for fuel assembly simulations will be the starting point of obtaining an accurate representation of the flow fields, turbulent viscosities, and where the turbulent heat flux is obtained from the simple eddy diffusivity assumption.

3.3 Discretization schemes

STAR-CCM+ adopts a finite volume approach for the discretized solution of the Navier-Stokes equations. In this method the computational domain is partitioned into a finite number of control volumes that match the cells of the computational grid. Thus, eq. (3.1) and (3.2) need to be discretized and applied to each control volume in a consistent manner.

Finally, a set of linear algebraic equations is obtained with the total number of unknowns in each system of scalar equations given by the number of cells in the computational grid. It is solved with an algebraic multigrid solver (AMG).

Further, an example is given to describe the way in which the finite volume discretization methods are used in STAR-CCM+: the transport of a simple scalar quantity. The governing equation in continuous integral form is given as:

$$\frac{\partial}{\partial t}\int_V \rho\chi\phi\, dV + \oint_A \rho\phi(\vec{v}-\vec{v}_g)d\vec{a} = \oint_A \Gamma\nabla\phi\, d\vec{a} + \int_V S_\phi\, dV \tag{3.3}$$

The only difference between eq. (3.1) and (3.3) is the additional diffusive flux term. By applying this transport equation to a cell-centered control volume for cell-0 the following form is derived:

$$\frac{d}{dt}(\rho\chi\phi V)_0 + \sum_f [\rho\phi(\vec{v}\cdot\vec{a}-G)]_f = \sum_f (\Gamma\nabla\phi\cdot\vec{a})_f + (S_\phi V)_0 \tag{3.4}$$

where G is the grid flux computed from the mesh motion, but can be set to zero for our interests.

The transient term, the first term in eq (3.4), is used only in the unsteady (transient) calculations. The second-order temporal discretization scheme found in the implicit unsteady solver uses the solution of the current time level, *n+1*, together with two previous time levels, *n*, and *n-1*, in the following way:

$$\frac{d}{dt}(\rho\chi\phi V)_0 = \frac{3(\rho_0\phi_0)^{n+1} - 4(\rho_0\phi_0)^n + (\rho_0\phi_0)^{n-1}}{2\Delta t} V_0 \tag{3.5}$$

STAR-CCM+ also offers the possibility to choose a first-order temporal scheme for slow transients applications. However, in the current study, the second-order scheme is the optimal choice for unsteady flow simulations and particularly quasi-DNS.

The convection term, the second term in eq. (3.4), is the most challenging term to discretize as it has a tremendous effect on the accuracy and convergence of the numerical scheme. First, it is discretized in the following simple way:

$$\left[\rho\phi(\vec{v}\cdot\vec{a}-G)\right]_f=(\dot{m}\phi)_f=\dot{m}_f\phi_f \tag{3.6}$$

where it is defined as the product of the scalar values and the mass flow rates at the face. The difficulty comes in when the scalar value at the face (ϕ_f) is calculated from the cell values. Several methods are available in STAR-CCM+ among which the following need to be mentioned and described: first-order upwind, second-order upwind, central-differencing and bounded central-differencing.

In the first-order upwind scheme, the convective flux is defined as:

$$(\dot{m}\phi)_f=\begin{cases}\dot{m}_f\phi_0 & \text{for } \dot{m}_f\geq 0\\ \dot{m}_f\phi_1 & \text{for } \dot{m}_f<0\end{cases} \tag{3.7}$$

First-order convection introduces a considerable amount of numerical dissipation that stabilizes the solver, yet it is not desirable in simulations where discontinuities are not aligned with the grid lines. The dissipation error has the effect of smearing the discontinuities, thus decreasing the accuracy of the solution, but this scheme is, in general, quite robust even if it is used only when the second-order upwind scheme is not available or does not reach convergence.

When second-order accuracy is demanded, the second-order upwind scheme is required. In STAR-CCM+, it is computed in the following way:

$$(\dot{m}\phi)_f=\begin{cases}\dot{m}_f\phi_{f,0} & \text{for } \dot{m}_f\geq 0\\ \dot{m}_f\phi_{f,1} & \text{for } \dot{m}_f<0\end{cases} \tag{3.8}$$

where

$$\begin{cases}\phi_{f,0}=\phi_0+\vec{s}_0\cdot(\nabla\phi)_{r,0}\\ \phi_{f,1}=\phi_1+\vec{s}_1\cdot(\nabla\phi)_{r,1}\end{cases} \tag{3.9}$$

are linearly interpolated from the cell values on either side of the face. Also, it was used that:

$$\begin{cases}\vec{s}_0=\vec{x}_f-\vec{x}_0\\ \vec{s}_1=\vec{x}_f-\vec{x}_1\end{cases} \tag{3.10}$$

were multiplied by their limited reconstruction gradients in cells 0 and 1, respectively. The limiting of the reconstruction gradients is important in reducing the local extrema. However, although it is less dissipative than the first-order upwind scheme, it still introduces more dissipation than a central-differencing scheme.

The convective flux in the central-differencing scheme, which is also second-order accurate, is given as:

$$(\dot{m}\phi)_f = \dot{m}_f\left[f\phi_0 + (1-f)\phi_1\right] \tag{3.11}$$

where f is the geometry weighting factor. This factor is correlated to the mesh stretching factor, thus for a uniform computational grid it would have a value of 0.5.

The clear benefit of using the central-differencing scheme over the second-order upwind is seen in applications where the turbulent kinetic energy needs to be conserved. Therefore, in LES calculations, the central-differencing is more appropriate because in the upwind schemes the turbulent kinetic energy decays quite fast.

For the RANS calculations, the second-upwind scheme is still the most appropriate as the central-differencing is susceptible to dispersive error that leads to stability problems for most steady-state simulations.

The last method for discretizing the convective flux is the bounded central-differencing:

$$(\dot{m}\phi)_f = \begin{cases} \dot{m}\phi_{fou} & \text{for } \varsigma < 0 \text{ or } 1 < \varsigma \\ \dot{m}\left[\sigma\phi_{cd} + (1-\sigma)\phi_{sou}\right] & \text{for } 0 \le \varsigma \le 1 \end{cases} \tag{3.12}$$

where at the face f, the values of the scalar quantity, ϕ, are as follows: ϕ_{fou} for the first-order upwind scheme, ϕ_{sou} for the second-order upwind scheme and ϕ_{cd} for the central-differencing scheme. σ is a smooth and monotone function of ζ (the Normalized-Variable Diagram value, calculated based on local conditions) which satisfies the following conditions:

$$\sigma(0) = 0 \tag{3.13}$$

and

$$\sigma(\varsigma) = 1 \text{ for } \varsigma_{ubf} \le \varsigma \cdot \varsigma_{ubf} \tag{3.14}$$

where ζ_{ubf} is called the upwind blending factor. A smaller value of ζ_{ubf} ensures better accuracy, while a larger value increases the stability of the scheme. This method is not fully second-order accurate as the central-differencing scheme because, when the boundedness criterion is not satisfied, the scheme turns into the first-order upwind one. Thus, on coarser meshes, the bounded central differencing scheme is expected to be more dissipative than the central-differencing

scheme; however, on computational grids required by LES simulations, that should not be an issue.

In the case of complex turbulent flows, this method is more accurate than the second-order upwind scheme and more stable due to the boundedness criterion. This makes the bounded central-differencing scheme along with a second order implicit scheme for temporal discretization the optimal choice for the DNS calculations of complex turbulent flows, such the studied grooved channel flow is expected to be.

The applicability of these discretization schemes to eddy resolving methods has been verified with a simple vortex test (Appendix D). In this test, a vortex is convected by a uniform flow on a periodic mesh. After a convective time, given that no interactions between the various vortices on the infinite domain are allowed, the vortex profile should be the same as the initial one. The numerical error introduced by the discretization schemes was quantified by the L2 norm of the difference between the initial profile and the profile after the convection. Thus, the conclusions found in the literature appropriate for our study were checked and confirmed for this version of STAR-CCM+. For more details, see the User Manual of STAR-CCM+ [10].

4. Turbulence Models

4.1 The Improved Anisotropic Turbulence Model

The Navier-Stokes equations for the instantaneous pressure and velocity fields are split into a mean and a fluctuating component in order to obtain the RANS equations. For the steady-state calculations, after time averaging, the obtained equations for the mean quantities are almost similar to the original equations, except for one more term in the momentum transport equation, the Reynolds stress tensor:

$$T_t \equiv -\rho\overline{v'v'} \tag{4.1}$$

Therefore, the Reynolds stress tensor needs to be modeled in order to close the system of governing equations. One of the approaches widely used is the eddy viscosity models, with the assumption that the Reynolds stress tensor is proportional to the mean strain rate:

$$T_t \equiv 2\mu_t S \tag{4.2}$$

It introduces the concept of turbulent viscosity (μ_t) that is derived from some additional scalar quantities, each transported by their own equation. For example, in the case of the K-Epsilon turbulence model, two transport equations are solved for the turbulent kinetic energy (k) and its dissipation rate (ε).

Accurate flow and temperature predictions require the use of adequate turbulence modeling, which still remains the most challenging component of the CFD application. In particular, the often overlooked turbulence anisotropy can have very noticeable effects on fuel assembly flow and heat transfer behavior. Among the possible effects of the anisotropy of the Reynolds stresses, one that is more evident is the formation of turbulence driven secondary flows in non-circular ducts. These secondary motions, also known as secondary flow of Prandtl second kind, although of small magnitude, highly contribute to the turbulence redistribution inside the sub-channels where the transport in the circumferential direction related to the secondary vortex is of the same order of magnitude of the turbulent transport.

In order to accurately predict turbulence in the fuel geometry, the Improved Anisotropic Turbulence Model was used [8]. Thus, instead of the customary eddy-viscosity assumption, a quadratic stress-strain relation is employed (4.3):

$$\rho\overline{u_i u_j} = \frac{2}{3}\rho k\delta_{ij} - \mu_t S_{ij} + C_1\mu_t\frac{k}{\varepsilon}\left(S_{ik}S_{kj} - \frac{1}{3}\delta_{ij}S_{kl}S_{kl}\right) + C_2\mu_t\frac{k}{\varepsilon}\left(\Omega_{ik}S_{kj} + \Omega_{jk}S_{ki}\right) + C_3\mu_t\frac{k}{\varepsilon}\left(\Omega_{ik}\Omega_{jk} - \frac{1}{3}\delta_{ij}\Omega_{kl}\Omega_{kl}\right)$$

where the formulation of the coefficients multiplying the quadratic terms respects the realizability conditions:

$$C_1 = \frac{c_{NL1}}{\left(c_{NL4} + c_{NL5}S^3\right)C_\mu} \tag{4.4}$$

$$C_3 = \frac{c_{NL3}}{\left(c_{NL4} + c_{NL5} S^3\right) C_\mu} \tag{4.5}$$

$$C_2 = \frac{c_{NL2}}{\left(c_{NL4} + c_{NL5} S^3\right) C_\mu} \tag{4.6}$$

and the adopted coefficients c_{NL1}, c_{NL2}, c_{NL3}, c_{NL4}, c_{NL5} are given in Table 5.

Table 4.1 Quadratic coefficients used in the Anisotropic Turbulence Model

Coefficient	Value
c_{NL1}	0.8
c_{NL2}	11
c_{NL3}	4.5
c_{NL4}	1000
c_{NL5}	1.0

4.2 Quasi-DNS

The accuracy of the DNS studies lies in the fact that the Navier-Stokes equations are numerically solved without any modeling; therefore, no turbulence model is required. In fact, DNS simulations are often used to validate the turbulence models. With this simulation technique all the length scales of turbulence are resolved: from the integral length scale, associated with the geometrical features of the boundaries, up to the smallest dissipative scales (i.e. Kolmogorov length scales). Thus, defining a sufficiently fine mesh is vital in order to obtain an accurately resolved solution.

Another aspect of a DNS analysis is related to the selection of the numerical schemes. In general, the DNS studies are performed with fourth order numerical schemes in order to reduce the numerical errors. Nonetheless, in this study, second order schemes were used for both spacial and temporal discretizations. As a consequence, it is important to note here that this approach to doing DNS calculations is reasonable; however, its accuracy is not fully verifiable as the DNS standards would normally require. Thus, this variation of the DNS method is referred to as quasi-DNS [11].

5. RANS Analysis

5.1 CAD Geometry

The CAD geometry from Figure 2.1 was built using the 3D-CAD parametric solid modeler of the STAR-CCM+ package. The three geometrical projections (front, top and side) are given below in Figure 5.1. The geometry is based on the MIT LEU design (Appendix A). All the dimensions were taken from the MITR Reactor Systems Manual [2], except for the height of the column (that is, the flow or z direction). This is because, in order to achieve an optimal mesh distribution, the outlet sections of the three materials (i.e. aluminum, water, UO_2) were extruded. A number of 150 layers with a stretching factor of 1.75 was used. Moreover, the boundary interface conditions implemented are given in Table 5.1.

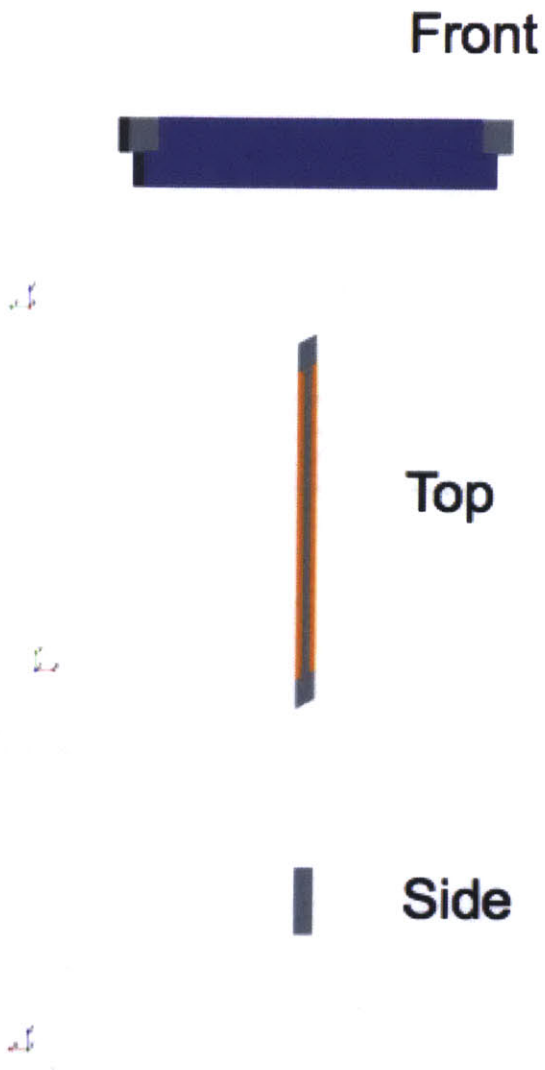

Figure 5.1 Isometric views of CAD model.The blue and orange colors represent the water region while the aluminum fuel plate is shown in gray

Table 5.1 Boundary conditions for the CFD model

Surface Region	Boundary	Thermal Specification	Shear Stress Specification
Fuel Meat	Wall	Conjugate heat transfer (volumetric heat source)	-
Aluminum Plate	Wall	Adiabatic	-
Water Inlet	Velocity	-	-
Water Sides	Symmetry Plane	-	-
Water/Aluminum Plate interface	Wall	Adiabatic	No-Slip
Water Outlet	Pressure Outlet	-	-

The main difference between this CAD model and the MIT LEU design (Appendix A) is that the grooves with a depth of 10 mils featured on the cladding surface were removed. Also, the cladding width was increased by 5 mils on each side such that the effective interior channel thickness is preserved (see Figure 5.5 for a zoomed in section showing the absence of the grooves).

5.2 Mesh

5.2.1 Volume Mesh

The user driven, automatic meshing tools in STAR-CCM+ have been used to generate the optimal geometrical discretization. For this design, the trimmed cell mesher and the prism layer mesher were used. The latter is used only in the water regions to create the necessary orthogonal prismatic cells near the wall boundaries in order to improve the accuracy of the flow solution in the boundary layer region. For the rest of the regions, the former method produced a predominantly hexahedral mesh with minimal cell skewness and adequate local refinement for accurately modeling the various local features. The parameters and values used in generating the mesh are given in Table 5.2. Moreover, as it was mentioned in the previous section, the outlet sections of the three materials (i.e. aluminum, water, UO_2) and the inlet section of the entry water channel were extruded from the inlet and outlet plane mesh surface. The details are given in Table 5.3 and Table 5.4 and a side section is given in Figure 5.2 to show the results, while Figure 5.3 offers a better perspective of where the section from Figure 5.2 is positioned. The thickness of the near-wall prism layer, the total prism layer thickness and the number of prism layers were obtained iteratively by analyzing the wall y+ (see definition in Eq. 6.3) values obtained from running the simulation (further details given in section 5.2.3). The fine grid obtained can be seen in Figure 5.4 where a zoomed-in section is plotted (close to the corner of the fuel meat). Finally, in Figure 5.5 a top view horizontal section is given for more insight.

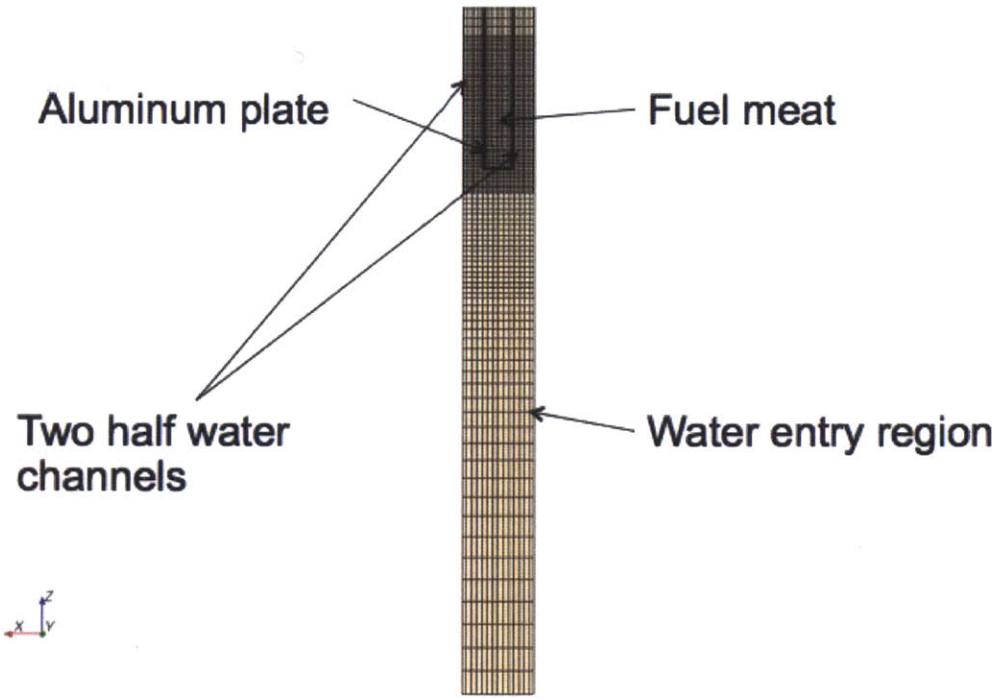

Figure 5.2 Zoomed in side section showing the grid after extrusion (the lower part from Figure 5.3)

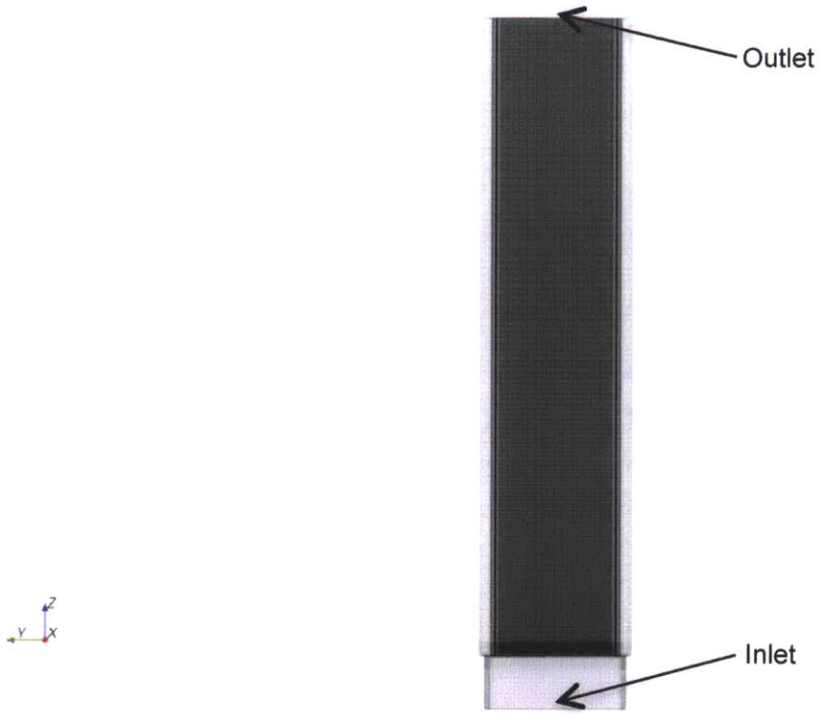

Figure 5.3 Front view of the full geometry after the grid was generated (transparency set to 1%)

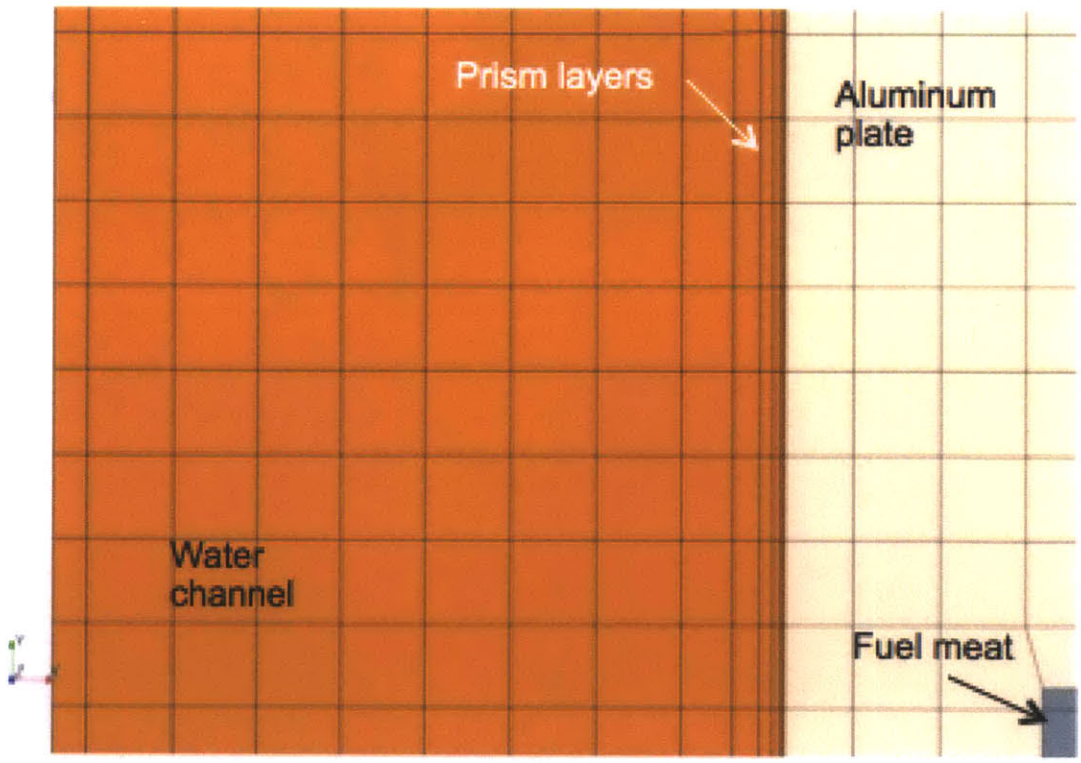

Figure 5.4 Top view of a zoomed in section after the grid was generated where the prism layers are showed

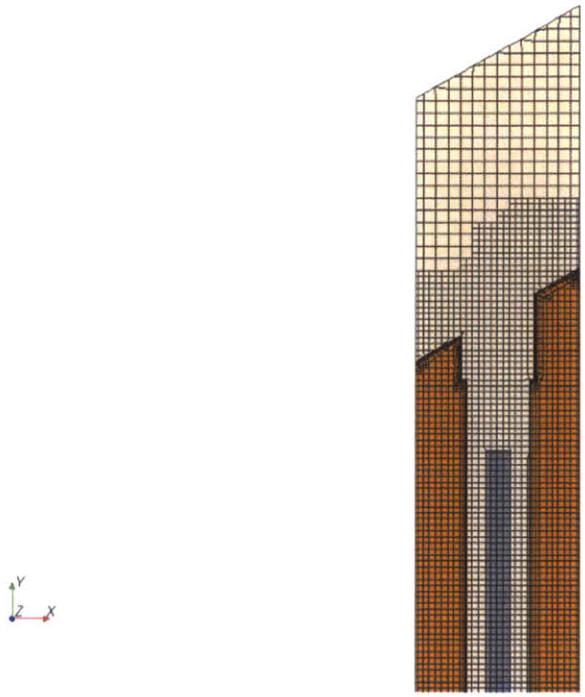

Figure 5.5 Top view of a horizontal section zoomed in

Table 5.2 Meshing parameters and values

Parameter	Value
Base Size	0.005 in (0.127 mm)
Maximum Cell Size (Relative to Base)	200%
Number of Prism Layers	6
Prism Layer Thickness	0.006 in (0.1524 mm)
Thickness of Near Wall Prism Layer	0.0001 in (0.00254 mm)
Surface Growth Rate	1.5
Template Growth Rate	Fast
Custom Boundary Growth Rate	8

Table 5.3 Extrusion parameters and values for extrusion in the +z direction

Parameter	Value
Extrusion Type	Hyperbolic tangent
Number of Layers	150
Stretching	1.75

Table 5.4 Extrusion parameters and values for extrusion in the -z direction

Parameter	Value
Extrusion Type	Hyperbolic tangent
Number of Layers	25
Stretching	1.25

5.2.2 Model Shakedown Testing

In order to test the model performance, verify any potential issue with grid quality, optimize the grid, particularly in the near wall regions, and perform the necessary sensitivity studies, a first set of runs were performed with a uniform heat flux as a first approximation. The data are given in Table 5.5. The material properties used are given in Appendix B.

Table 5.5 Initial conditions parameters and values

Parameter	Value
Inlet Velocity	3 m/s
Inlet Temperature	40 °C
Turbulent Intensity	20%
Turbulent Length Scale	0.2525 in (6.4135 mm)
Turbulent Velocity Scale	1 m/s
Pressure	1 atm

5.2.3 Near Wall Prism Layer

Given the challenging low Reynolds number flow conditions of this application (i.e. laminar and transition flow), and the importance of accurate hear transfer coefficient prediction, the use of wall functions was discarded in favor of a more rigorous near wall modeling. The transport

equations are solved all the way to the wall in what is usually referred to as a low y+ approach or wall resolved method. Therefore, in order to accurately resolve the viscous sublayer, a fine grid had to be generated. Accordingly, the thickness of the near the wall prism layer, the total prism layer thickness and the number of prism layers were evaluated. Finally, as shown in Table 5.2, 6 prism layers were used to resolve the y+ 40 region (the edge of the viscous sublayer) and the y+ was kept below 0.5 at the first cell near the wall (Figure 5.6). This approach allows further applicability of this computational mesh to laminar and transitional cases.

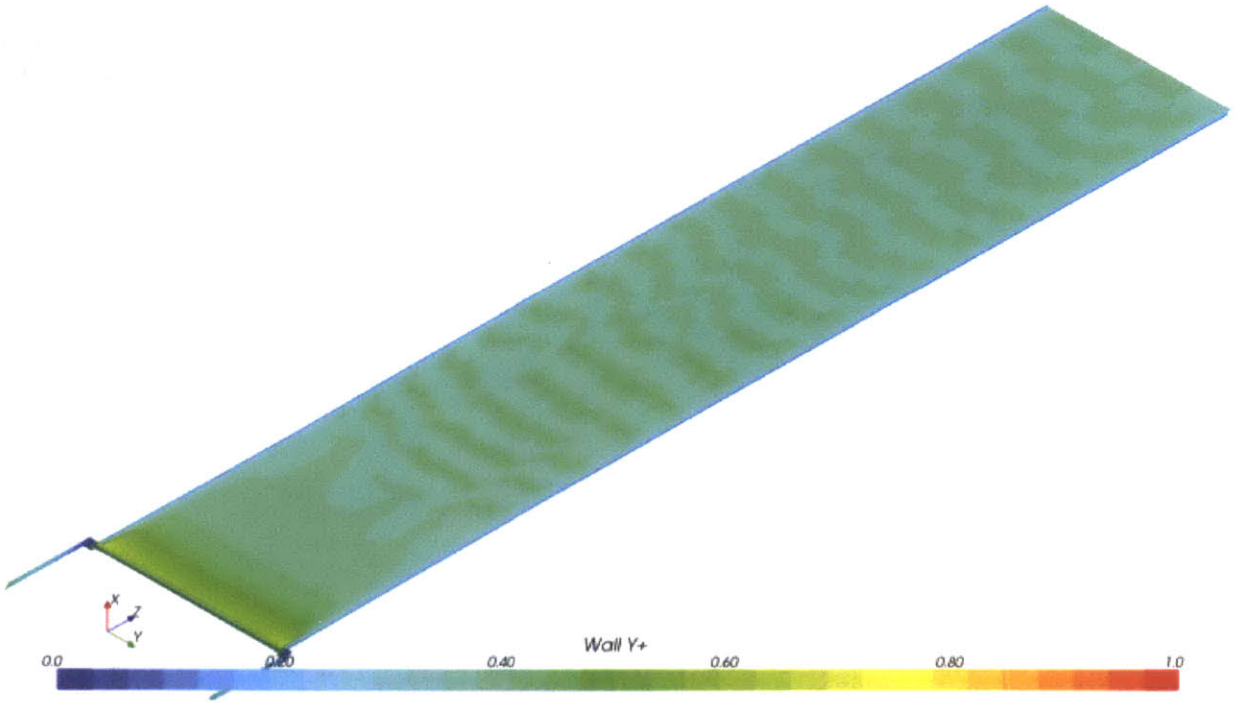

Figure 5.6 Wall y+ values on the fuel element surface plotted in a perspective view

5.2.4 Grid Convergence

A grid sensitivity study is required in order to evaluate the cell base size that optimizes the simulation speed while minimizing computational usage, and more importantly, the discretization error. Various parameters are analyzed to check the grid convergence.

First, the water temperature profiles as a function of the radial position for various base sizes from 0.003 to 0.0075 in were plotted along a line probe normal to the wall at a height of 12 in (fully developed region, see Figure 5.10 for the line probe position). From the plot (Figure 5.7), it can be observed how fine grid sizes (between 0.003 and 0.005 in) produce very similar results, which is indicated by the almost perfect overlap of the profiles. However, it is interesting to note that as the base size is increased to 0.007 in and 0.0075 in different values are obtained. This sudden change is a good demonstration of the modeling challenges related to the low Reynolds number and the need for grid evaluation.

As a further confirmation, using the same line probe, the axial velocity was plotted against the radial position for the same base sizes as above (Figure 5.8). Again, the profiles for the base sizes between 0.003 and 0.005 are in excellent agreement, while the higher base sizes show lower velocity profiles.

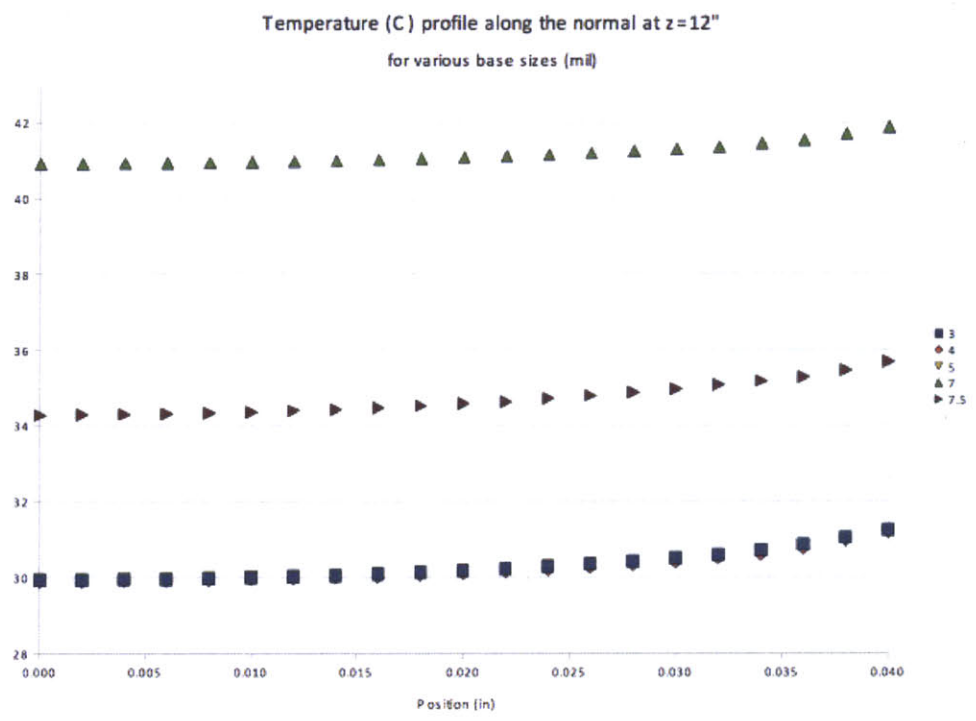

Figure 5.7 Water temperature profile as a function of the radial position for various grid sizes

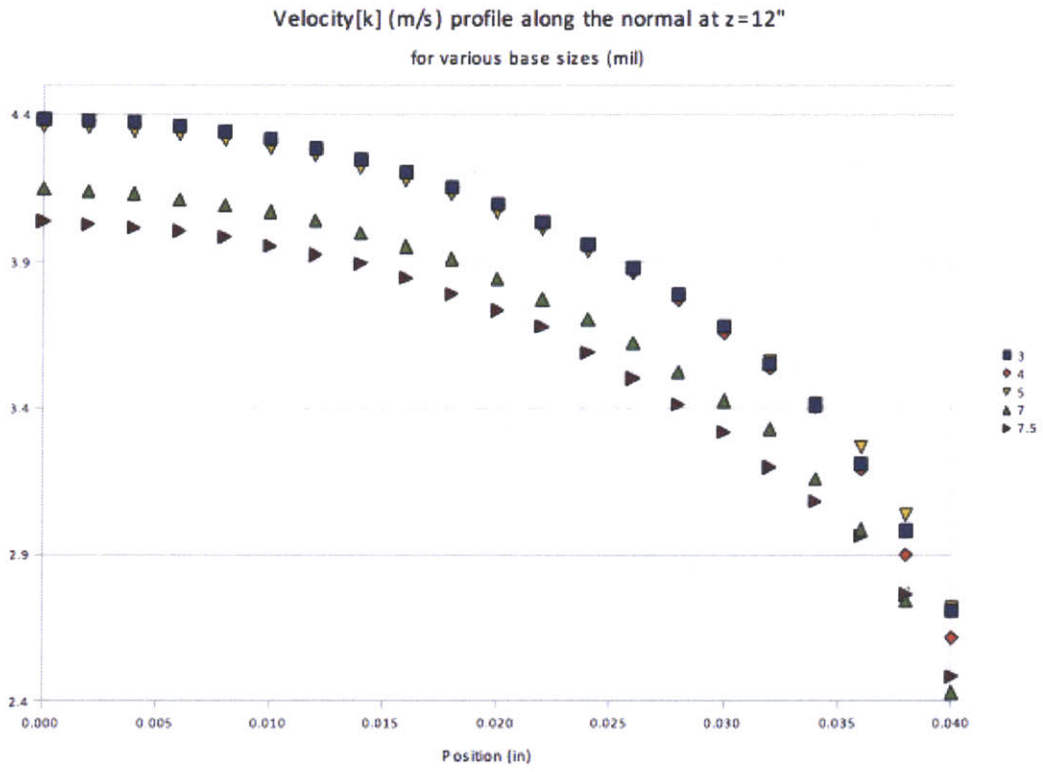

Figure 5.8 Water axial velocity profile as a function of the radial position for various grid sizes

Based on the results, the base size of 0.005 in was chosen as it provides optimal computational economy while producing highly accurate predictions. One final check was performed by looking at the pressure drop for the same base sizes from 0.003 to 0.0075 in (encircled in red) as shown in Figure 5.9. While the pressure drop shows smaller sensitivity to the grid quality, the same two outliers for base sizes 0.007 in and 0.0075 in are found.

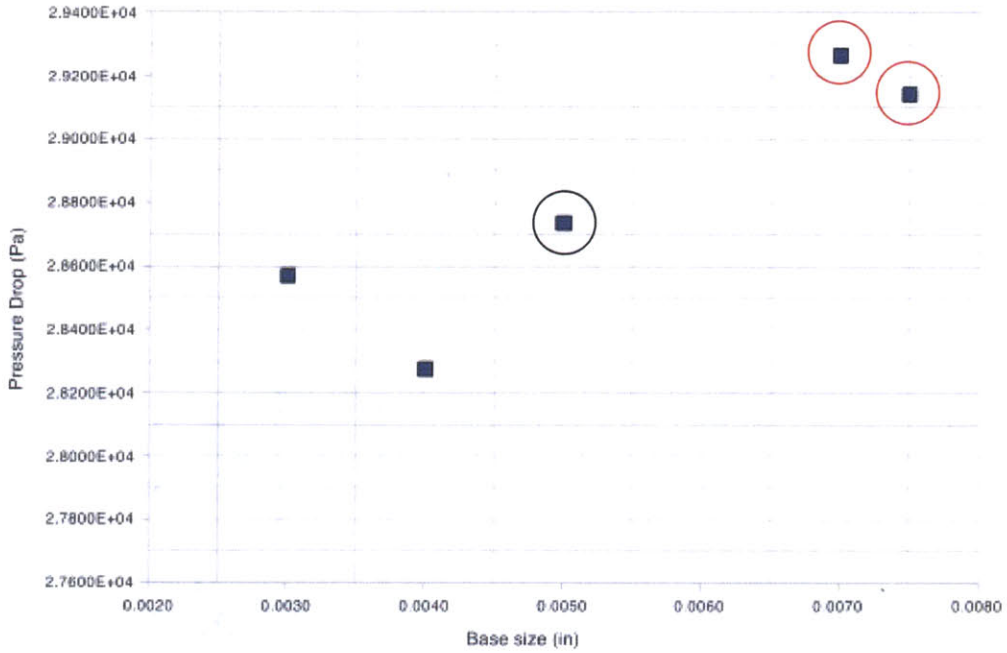

Figure 5.9 Pressure drop as a function of the base size (chosen base size encircled in black, outliers encircled in red)

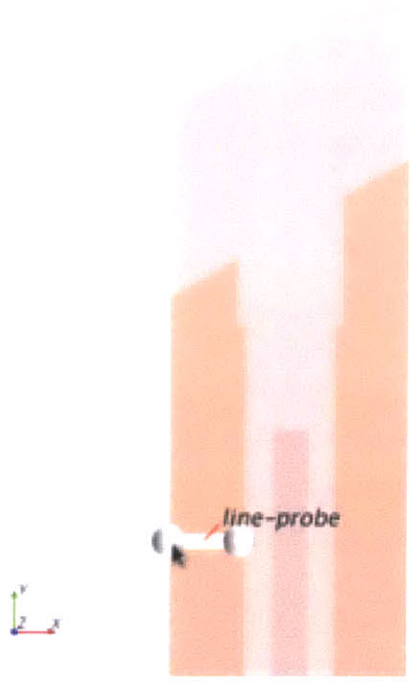

Figure 5.10 Line probe normal to the flow direction at z=12 in

5.3 Flow features

Although the inlet velocity is 3 m/s at the entrance channel, because the flow is split into two half-channels (see Figure 5.11 for streamlines that follow individual seed points from the inlet to the outlet, or even better, in a zoomed in section Figure 5.12) the streamwise velocity approximately doubles. In order to see this, the velocity magnitude was plotted by showing one side of the coolant channel (Figure 5.13).

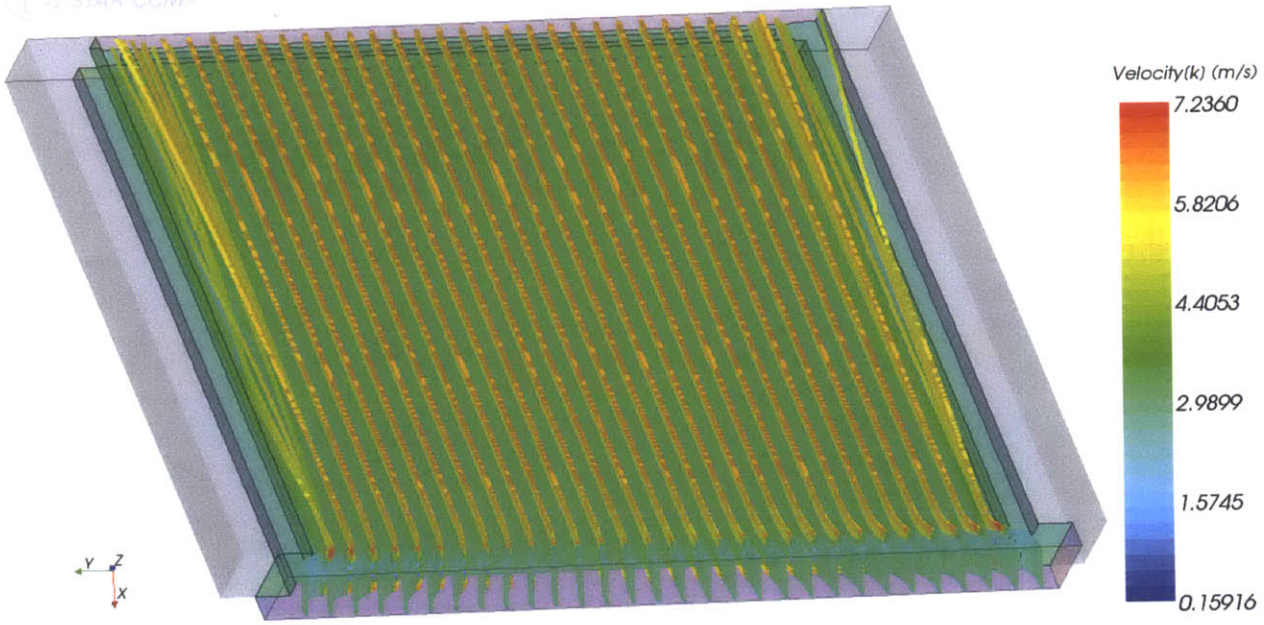

Figure 5.11 Perspective view of streamlines of the velocity along the z direction from the inlet to the outlet

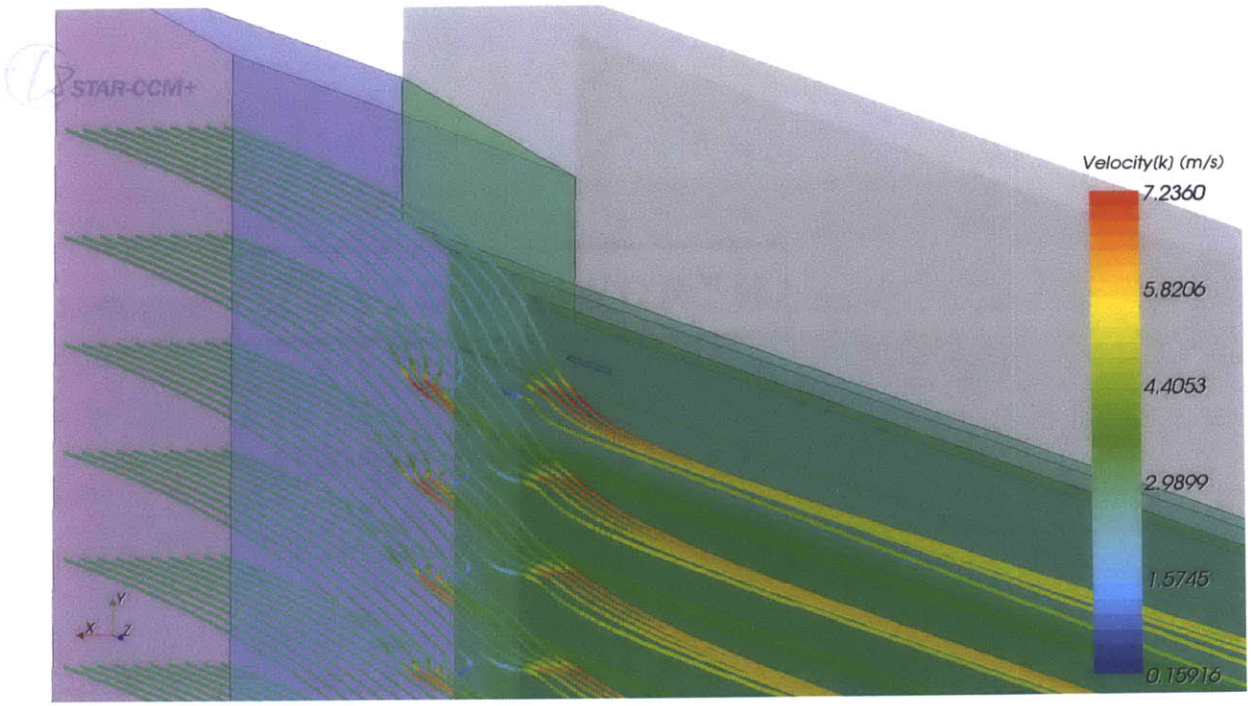

Figure 5.12 Zoomed in section around the corner inlet region of Figure 5.11

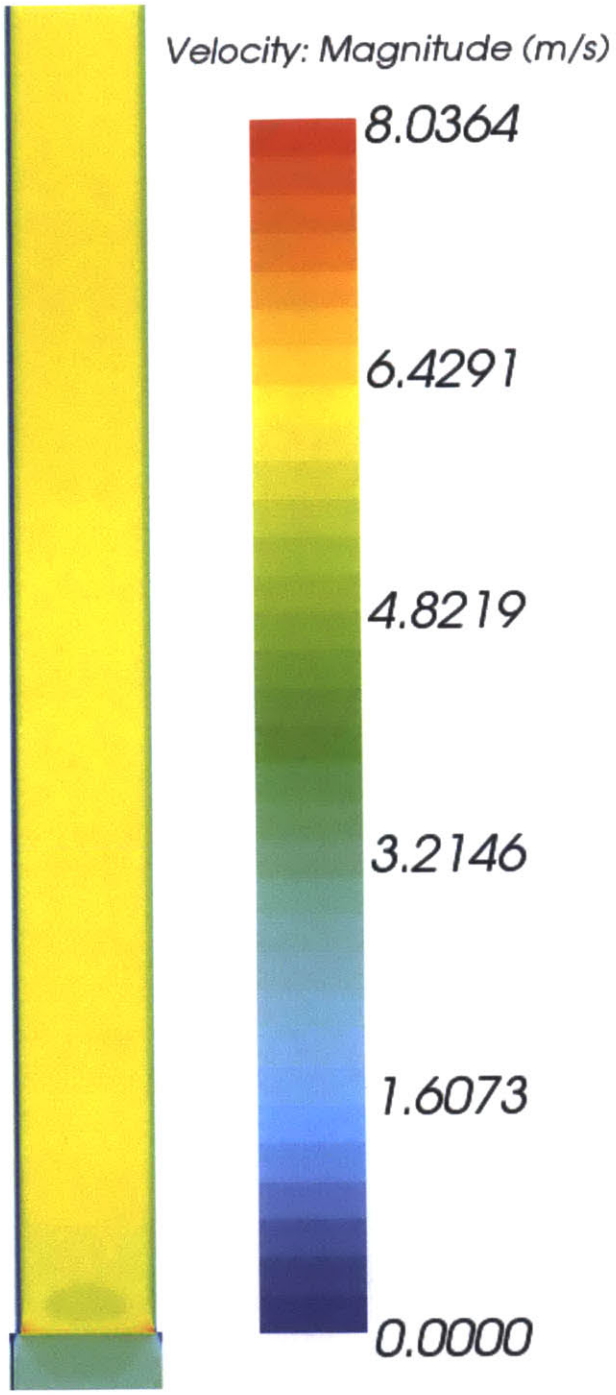

Figure 5.13 Velocity magnitude of the coolant from the inlet to the outlet

In Figure 5.11 and Figure 5.12 it can be seen that, on the edges of the lateral direction (y), the streamlines do not follow a straight direction parallel to the z direction, but they shift in various directions. This is because the improved anisotropic turbulence model used is able to capture the secondary recirculation flows (Figure 5.14). Given that the maximum magnitude of the

tangential velocity is about 8% of the inlet velocity, it was confirmed that the secondary flows need to be included for the accurate prediction of the flow and temperature distributions.

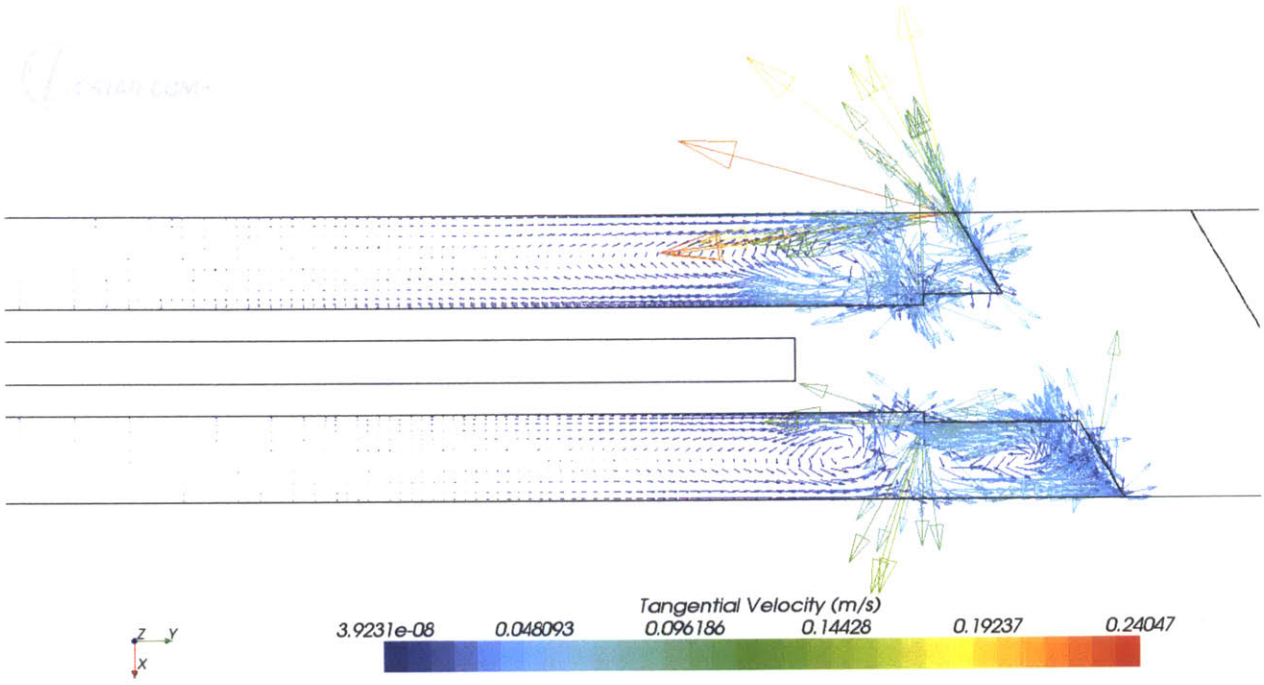

Figure 5.14 Cross section in the (x,y) plane showing the tangential velocity patterns at the corners

5.4 Results

Finally, the boundaries representing the operating power were implemented. The volumetric power generation was implemented both as uniform and non-uniform in the lateral direction, as is shown in Figure 5.15. In order to have the consistent results, the uniform lateral power was obtained from the given non-uniform lateral power distribution by keeping the area under the curves constant.

For further guidance in the results section, is important to note that the width of the fuel meat has a length of 2.082 in (from 0.36926 in to 2.451226 in on the y-axis).

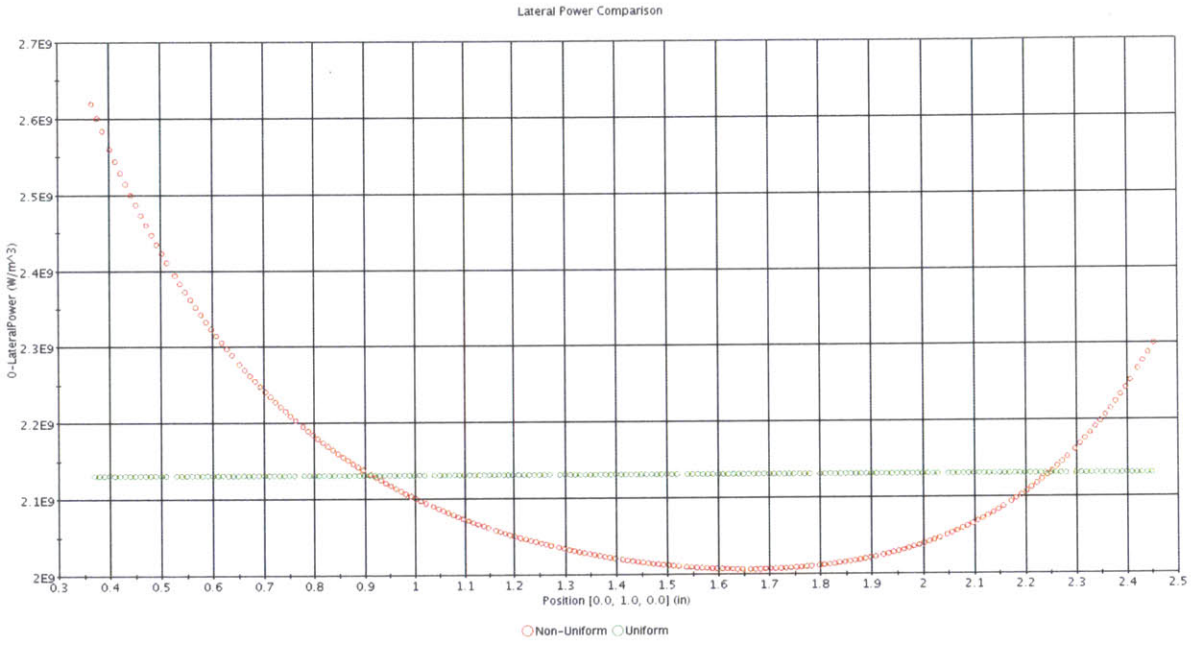

Figure 5.15 Lateral power distribution in the uniform and non-uniform cases

5.4.1 Uniform Volumetric Power Generation

The uniform power generation case results are given first. In what follows, the various temperature profiles are checked.

The cladding temperature along the axial direction is plotted in order to check the convergence of the simulation up to the outlet (Figure 5.16). It can be seen that the cladding temperature profile in the lateral direction is the same along the full length of the channel.

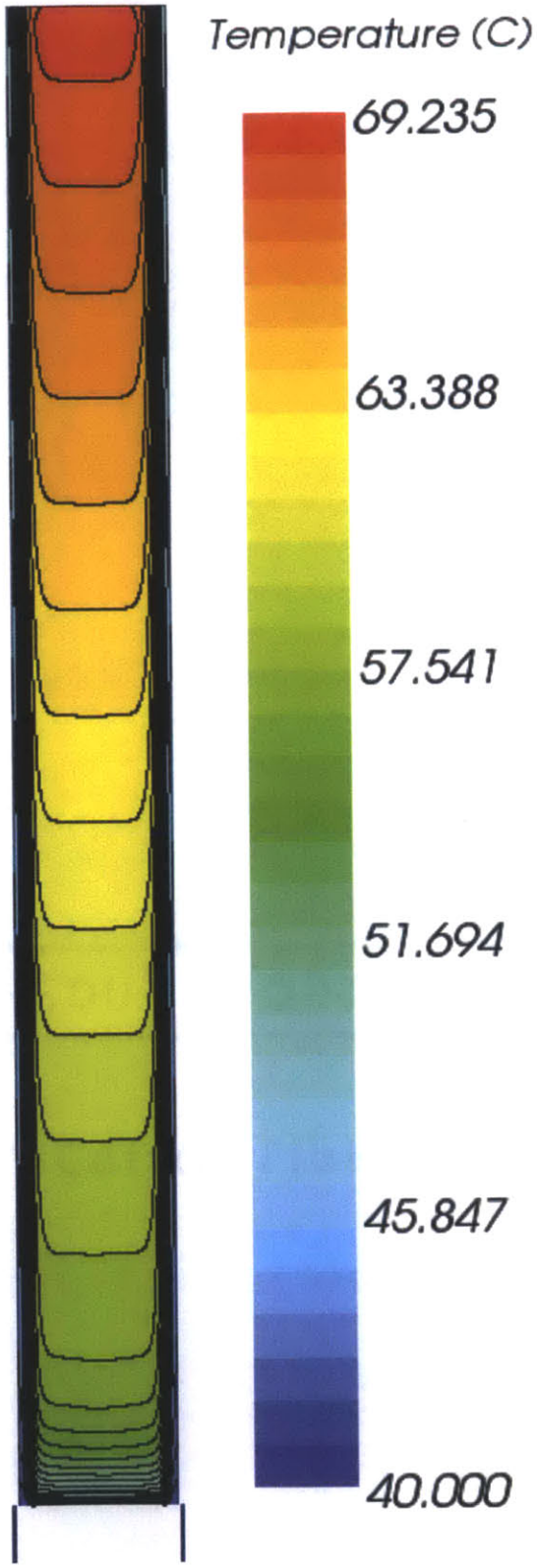

Figure 5.16 Cladding temperatures along the axial direction

In order to see the heating patterns in all the materials, a cross section was cut radially at a height of 20 in (Figure 5.17). As it can be seen, the fuel meat has a peak temperature of 73 °C, the aluminum plate has a temperature of about 50 °C on the sides, and the water temperature is about 51 °C in the middle of the channel and about 44 °C at the corners.

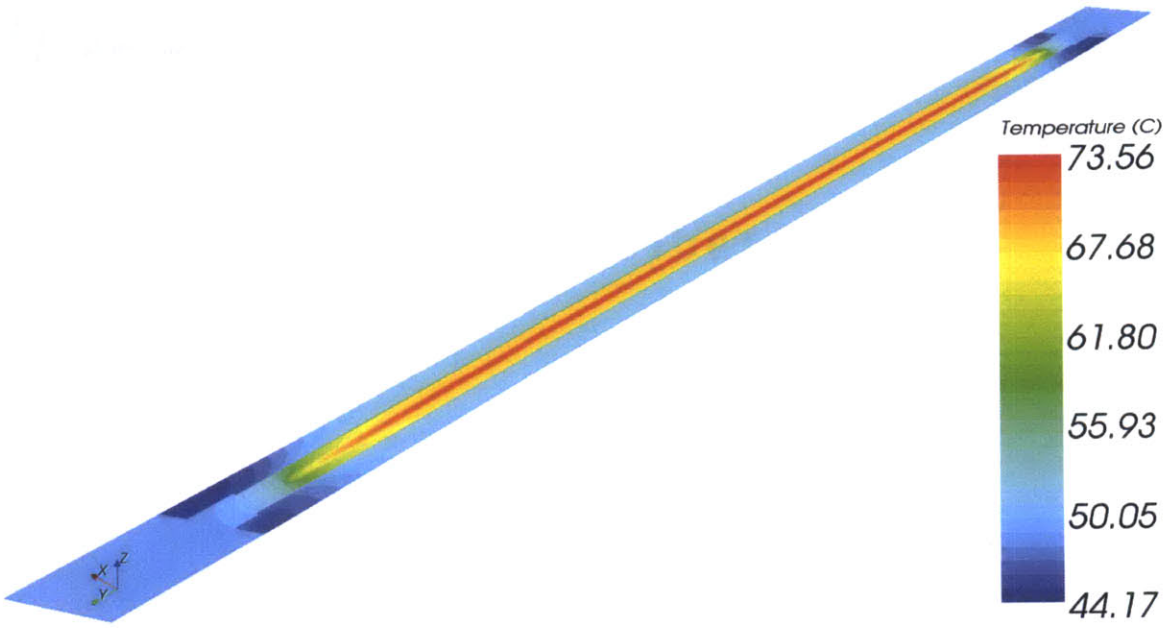

Figure 5.17 Temperature cross section at z=20 in

At a height of 20 in, a zoomed in view of the same horizontal cross section is shown in Figure 5.18.

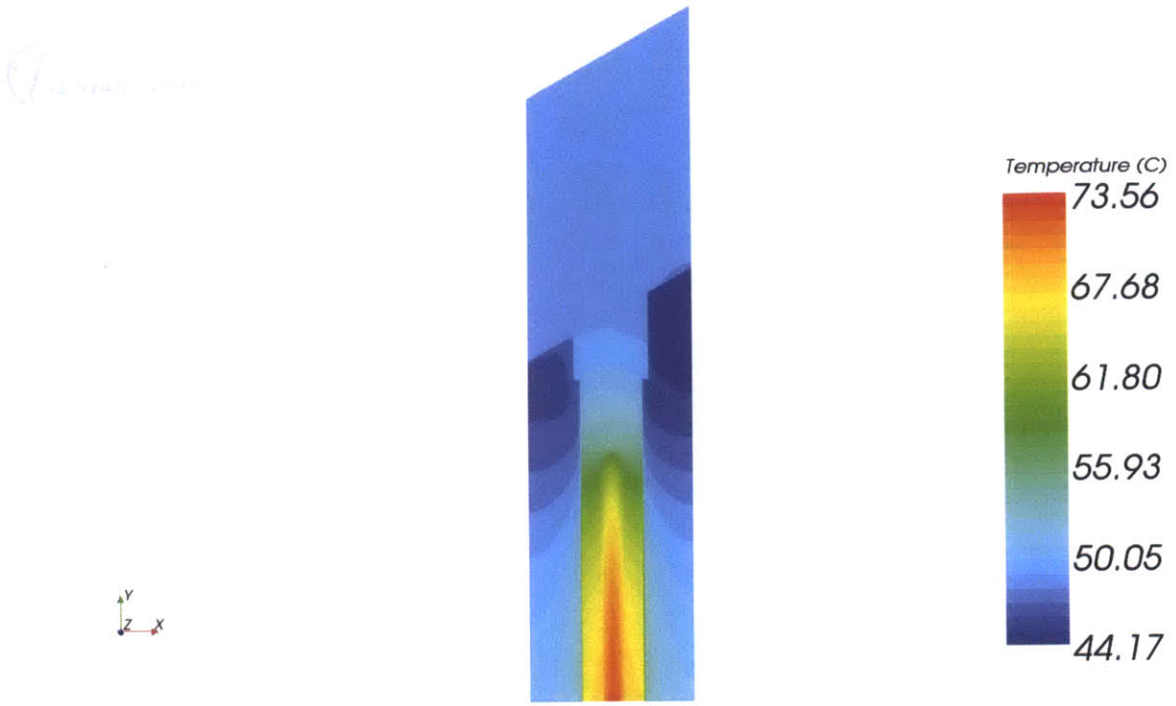

Figure 5.18 Temperature cross section at z=20 in

The water temperature in the radial direction of the line probe x at a height of 20 in (similar to the line probe from Figure 5.10) is plotted in Figure 5.19. It should be noted that the middle of the water channel is located at position 0.

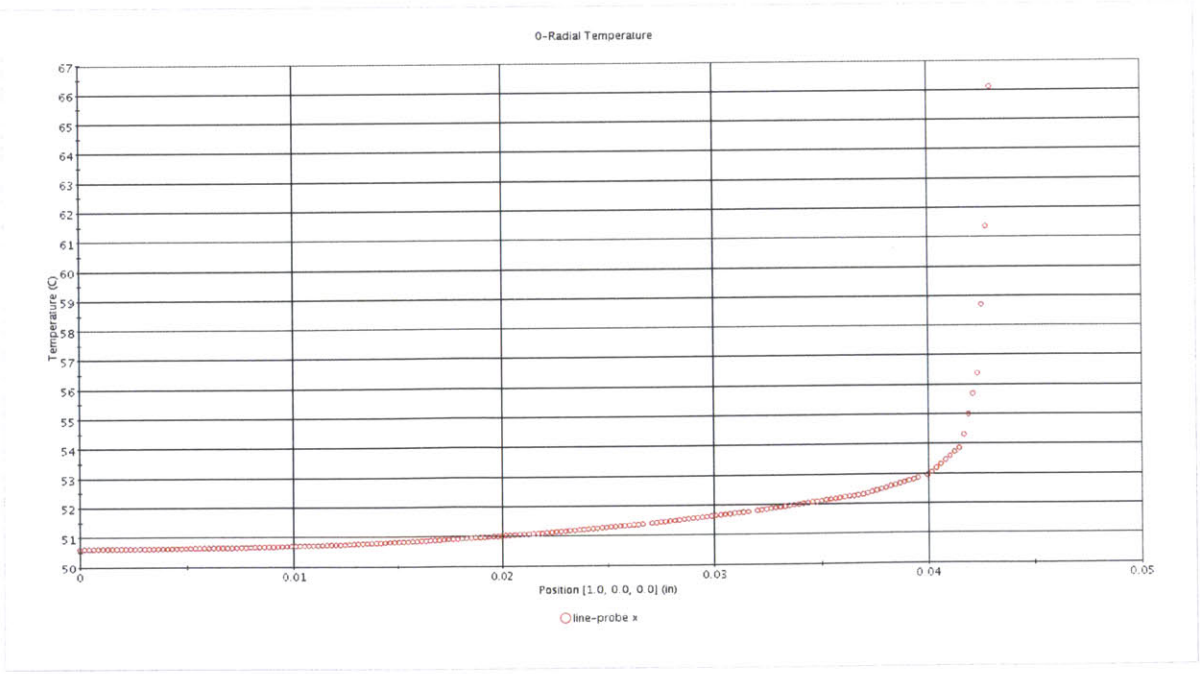

Figure 5.19 Radial water temperature for the line probe x

A set of radial line probes along the y direction (horizontal) were created at various axial locations: 5, 10 and 20 in. One was cut through the middle of the coolant half-channel, one along the cladding and the other one through the middle of the fuel meat (Figure 5.20).

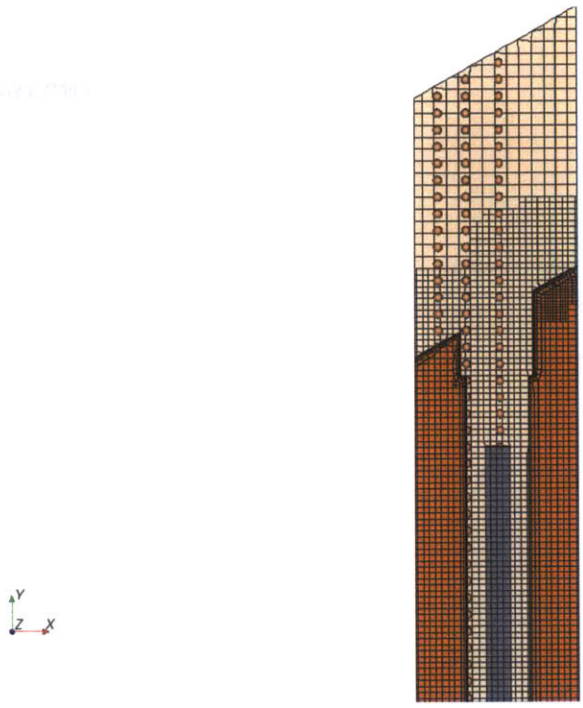

Figure 5.20 Three radial line probes along the y direction with 200 points

The cladding temperature profiles along the y direction are given in Figure 5.21, the temperature profiles along y cutting through the middle of the fuel meat are given in Figure 5.22, while the temperature profiles through the middle of the coolant half-channel are plotted in Figure 5.23. It can be noted that the temperature values on the sides in the y direction are not symmetrical due to the anti-symmetric geometry. Moreover, a gradual increase in the temperature profiles as the height increases can be observed in both figures.

Next, the heat flux at the cladding along the lateral direction is plotted at various axial locations (Figure 5.24).

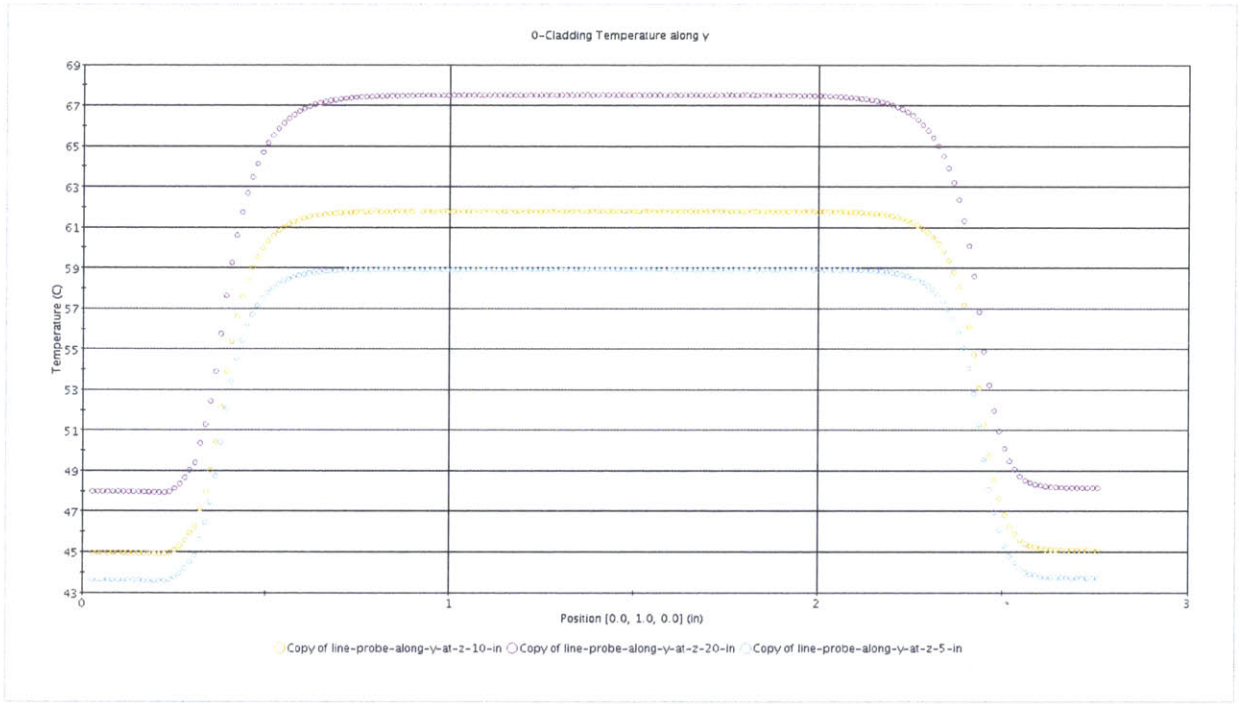

Figure 5.21 Cladding temperature along the y direction at various axial locations

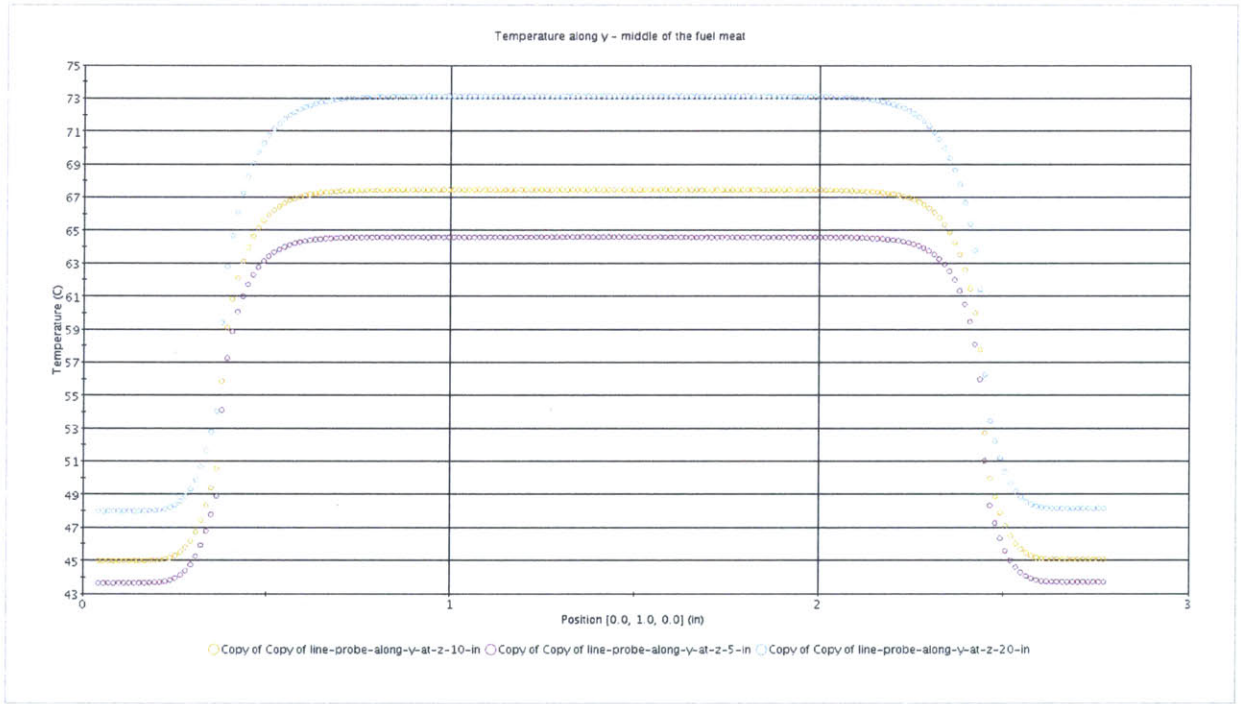

Figure 5.22 Temperature along the y direction in the middle of the fuel meat at various axial locations

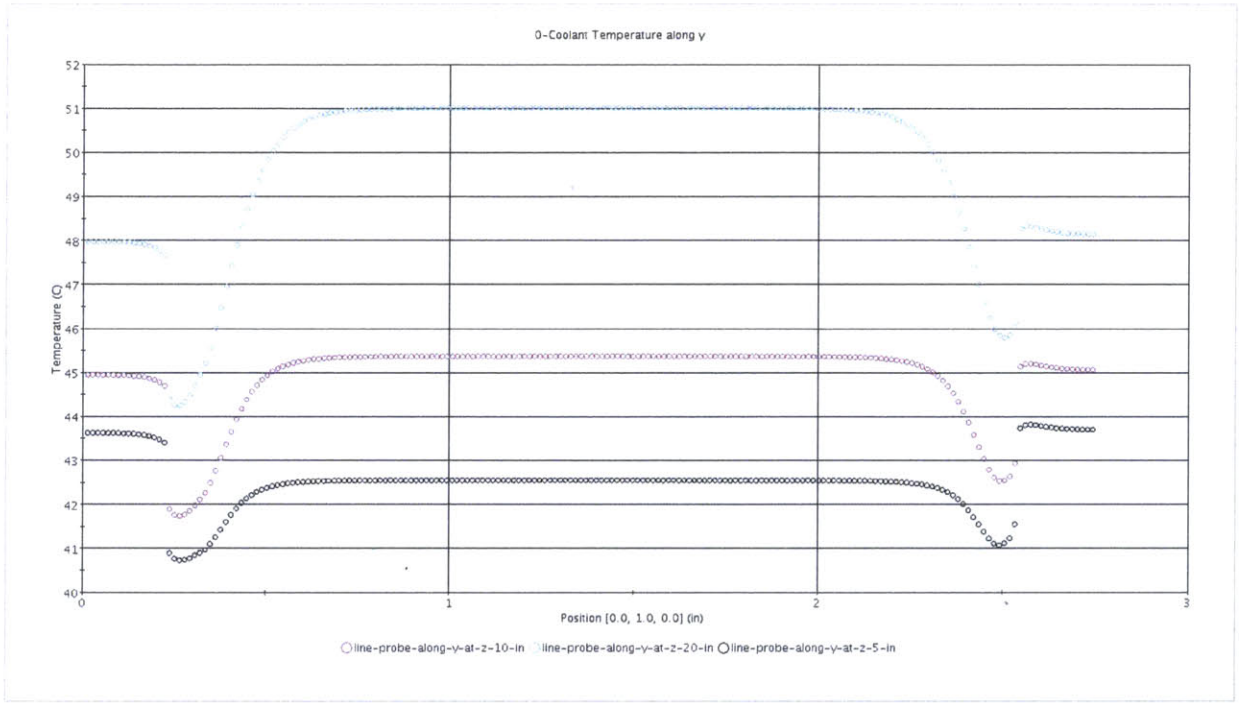

Figure 5.23 Temperature along the y direction in the middle of the half-coolant channel at various axial locations

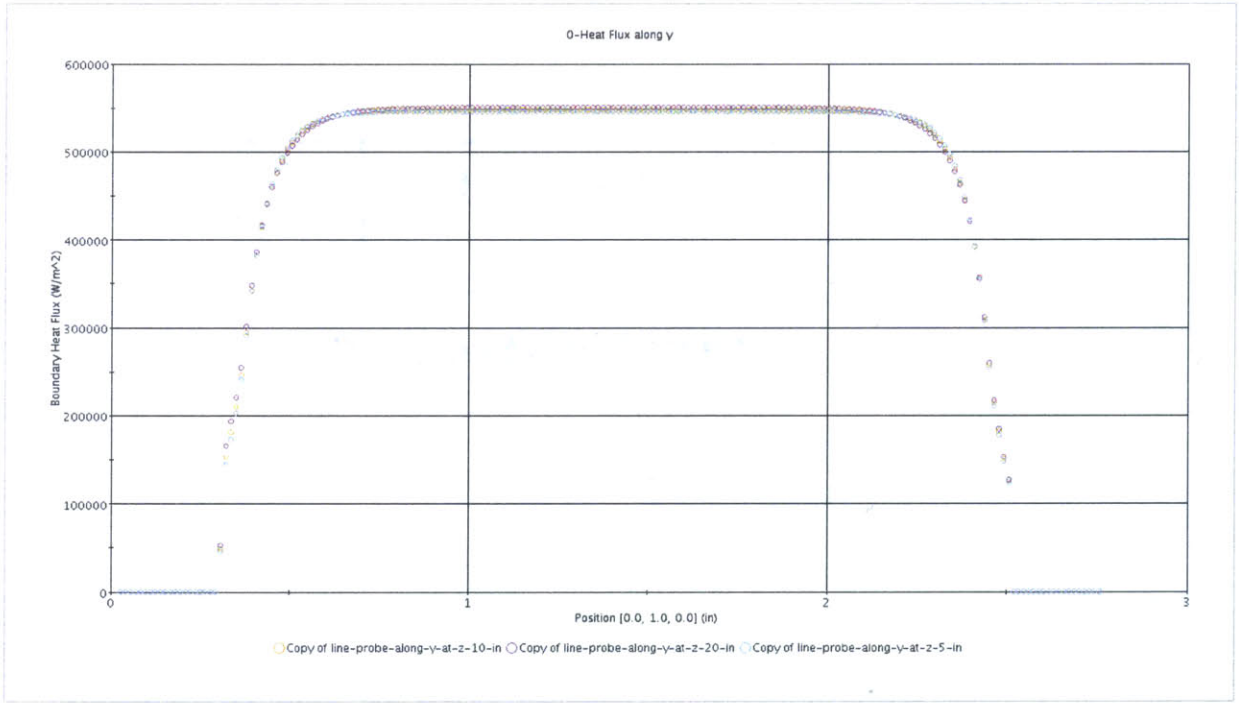

Figure 5.24 Heat flux along the y direction at various axial locations

Since the flow is already fully developed at z = 5 in (see Figure 5.16), the heat flux distribution does not change as the height is increased.

Finally, the heat transfer coefficient based on the bulk coolant temperature of the whole channel is plotted along the y direction (following the line probe from Figure 5.20 restricted only to the cladding) at z = 20 in (Figure 5.25).

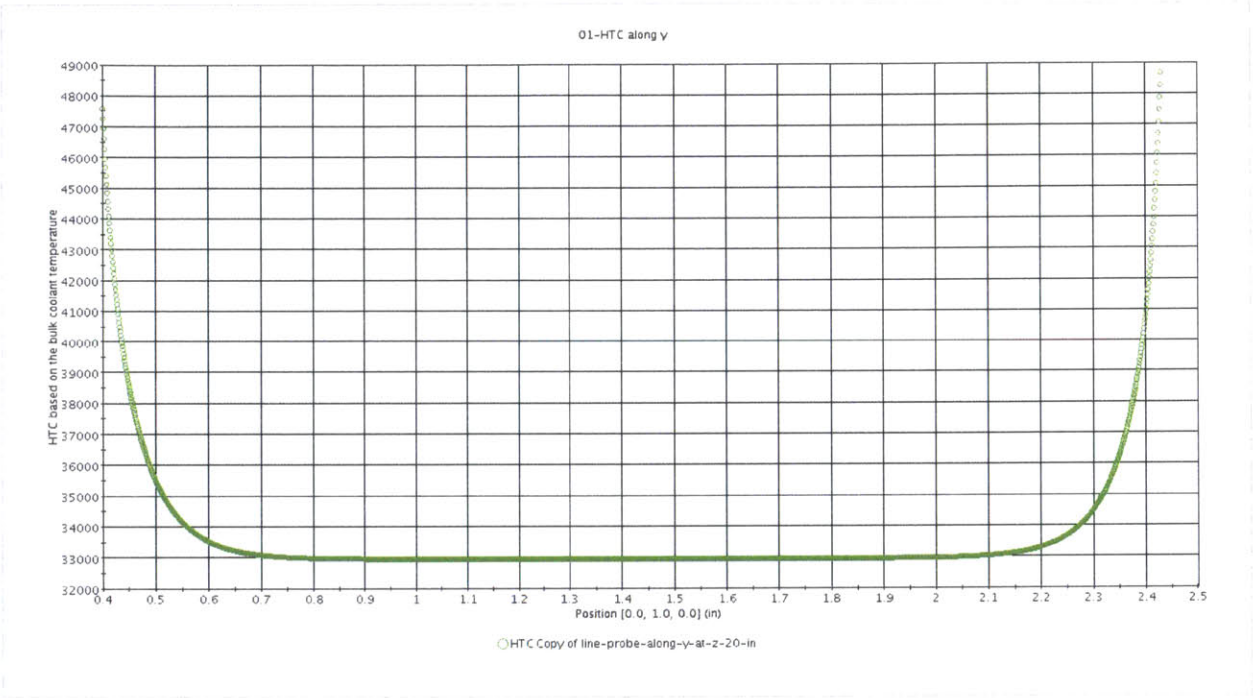

Figure 5.25 Heat transfer coefficient in the radial direction at at z = 20 in (T_{bulk} = 50.7 °C)

5.4.2 Non-Uniform Lateral Power Distribution

Again, the lateral cladding temperature patterns along the axial direction are plotted in order to check the convergence of the simulation up to the outlet for the non-uniform lateral power distribution case (Figure 5.26). As in the uniform case, it can be seen that the cladding temperature profile in the lateral direction is the same along the full length of the channel.

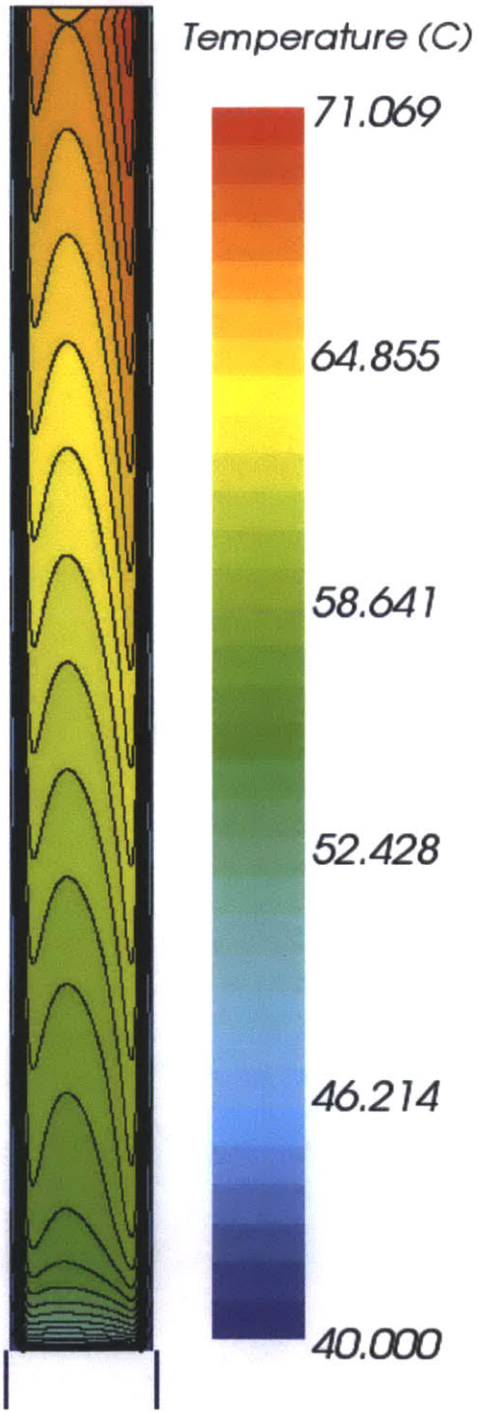

Figure 5.26 Lateral cladding temperature along the axial direction

In order to see the heating patterns in all the materials, a cross section was cut radially at a height of 20 in (Figure 5.27). The fuel meat has a peak temperature of 75 °C, the aluminum plate has a temperature of about 50 °C on the sides, and the water temperature is about 51 °C in the middle of the channel and about 44 °C at the corners.

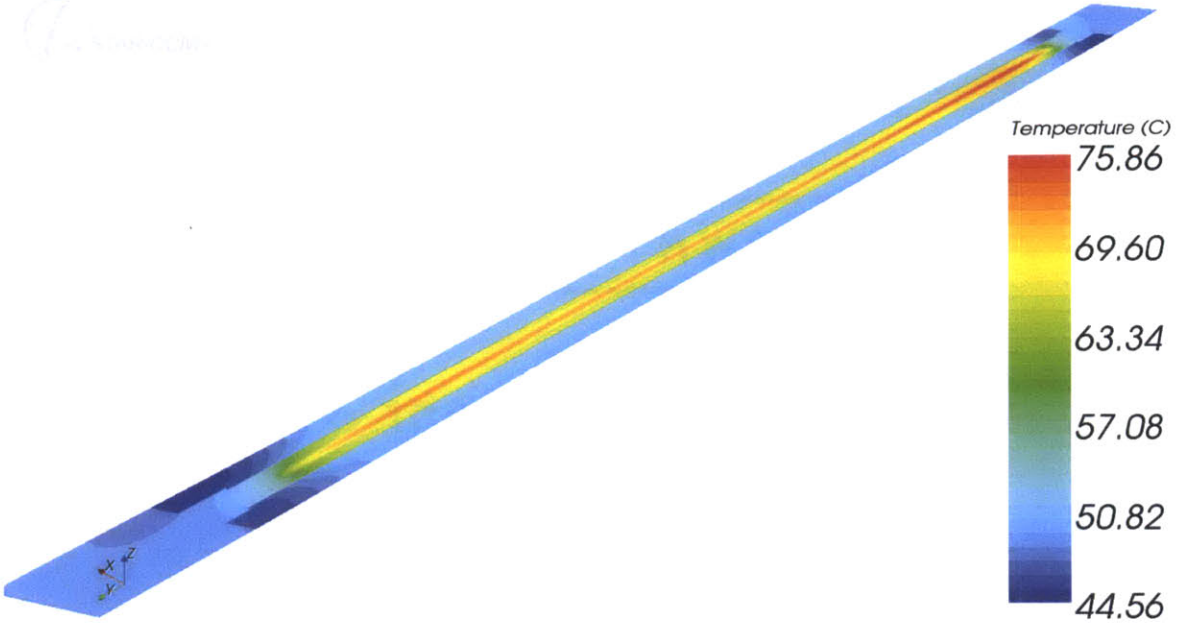

Figure 5.27 Temperature cross section at z=20 in

At z = 20 in, a zoomed in view of the same horizontal cross section is shown in Figure 5.28.

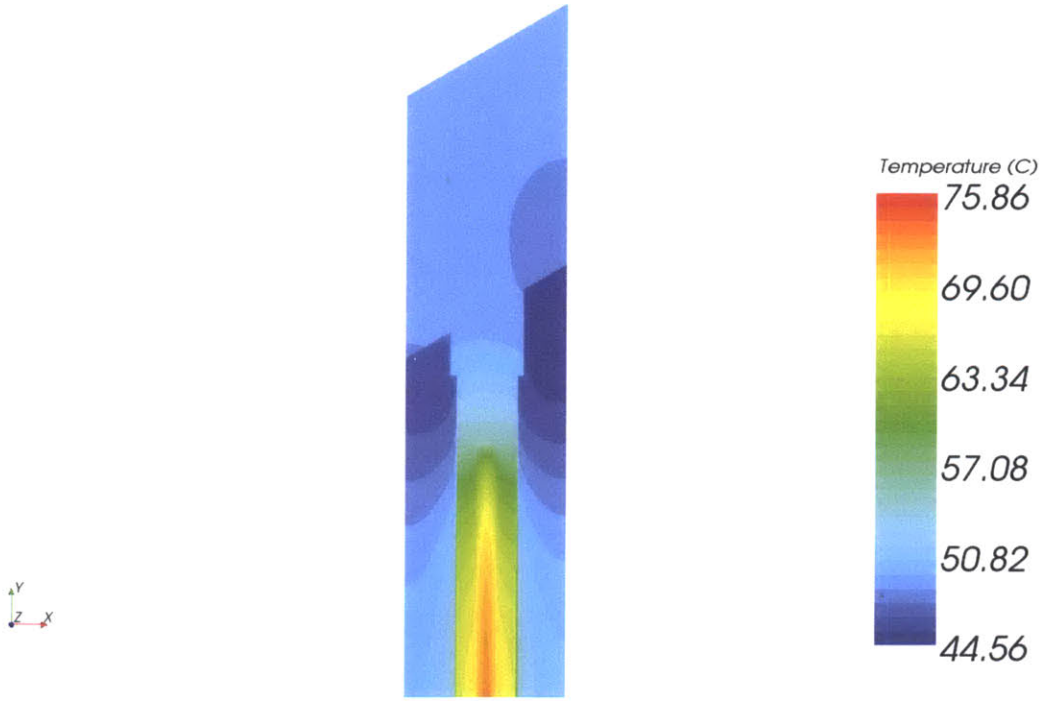

Figure 5.28 Temperature cross section at z=20 in

The water temperature in the radial direction of the line probe x at a height of 20 in (similar to the line probe from Figure 5.10) is plotted in Figure 5.29. The middle of the water channel is located at position 0.

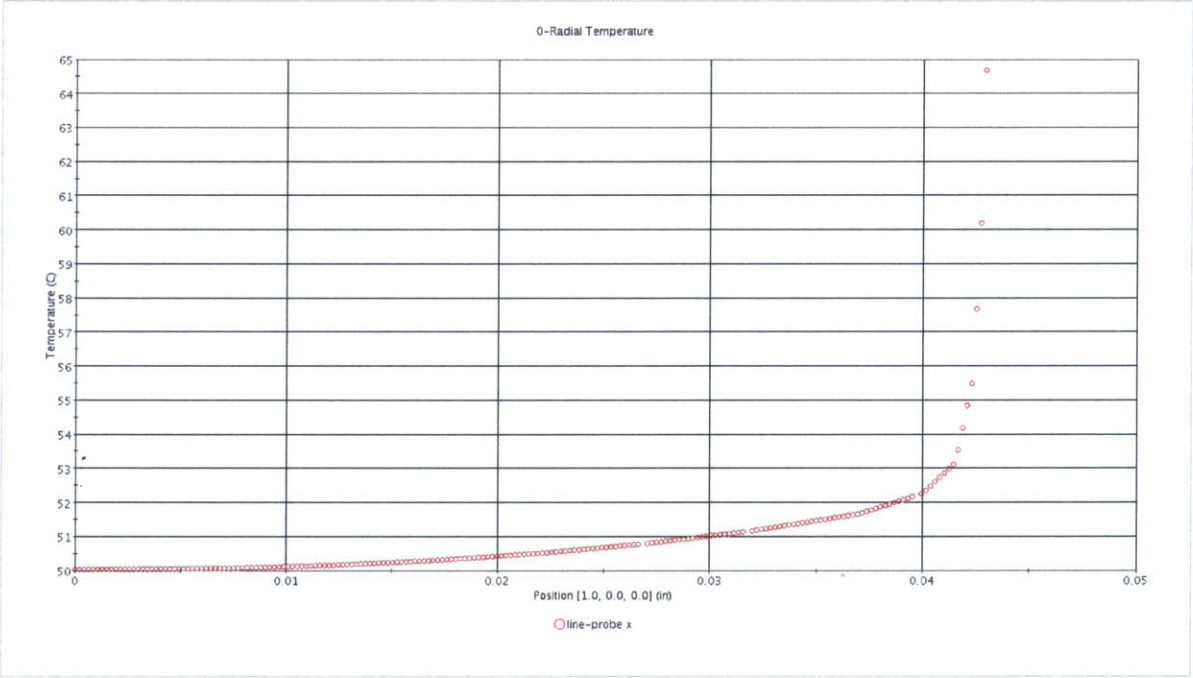

Figure 5.29 Radial water temperature for the line probe x

A set of radial line probes along the y direction (horizontal) was done at various axial locations (i.e. 5, 10 and 20 in) in the same way as in the uniform case from Figure 5.20.

The cladding temperature profiles along y are given in Figure 5.30, the temperature profiles along y cutting through the middle of the fuel meat are given in Figure 5.31, while the temperature profiles through the middle of the coolant half-channel are plotted in Figure 5.32. It can be noted that the temperature values on the sides in the y direction are not symmetrical due to the anti-symmetric geometry. Moreover, a gradual increase in the temperature profiles as the height increases can be observed in both figures.

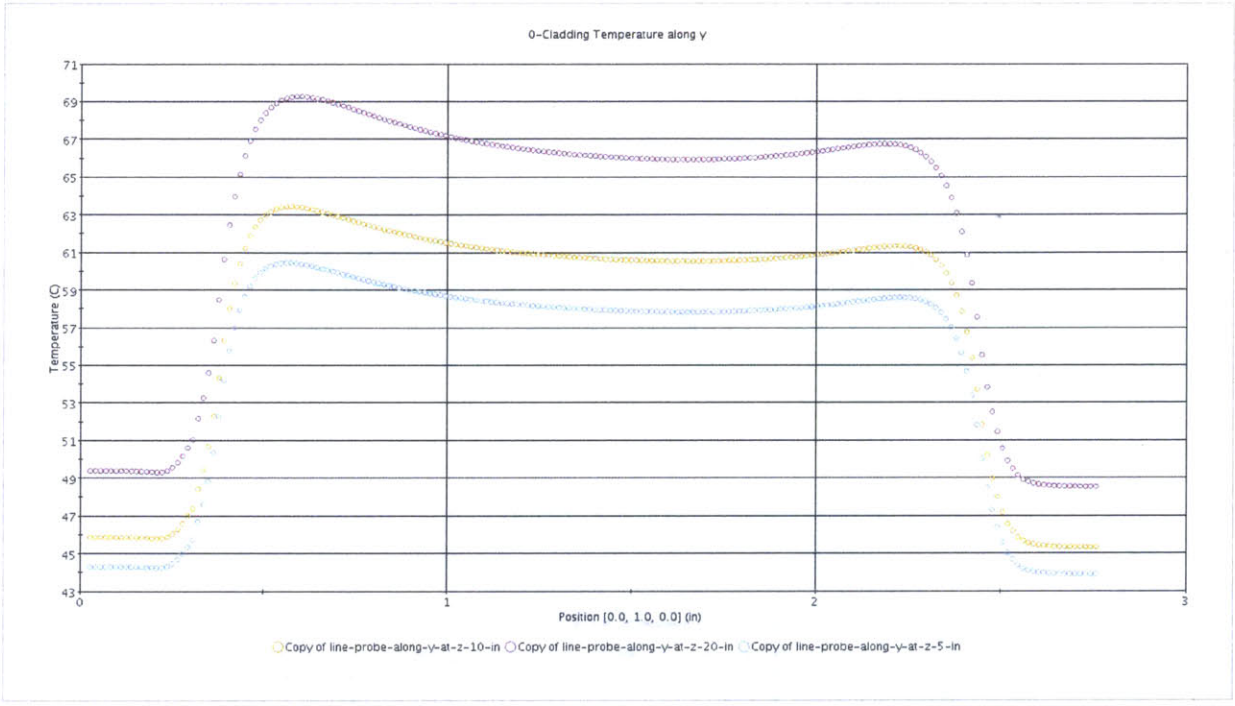

Figure 5.30 Cladding temperature along the y direction at various axial locations

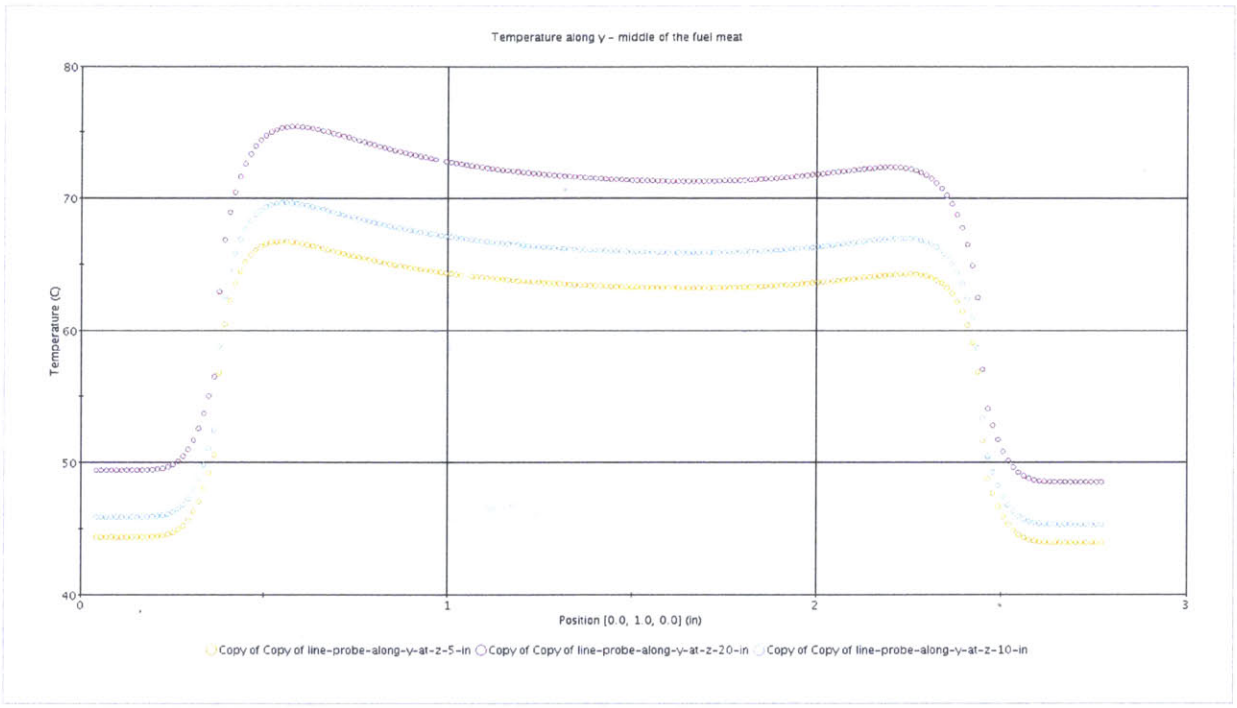

Figure 5.31 Temperature along the y direction in the middle of the fuel meat at various axial locations

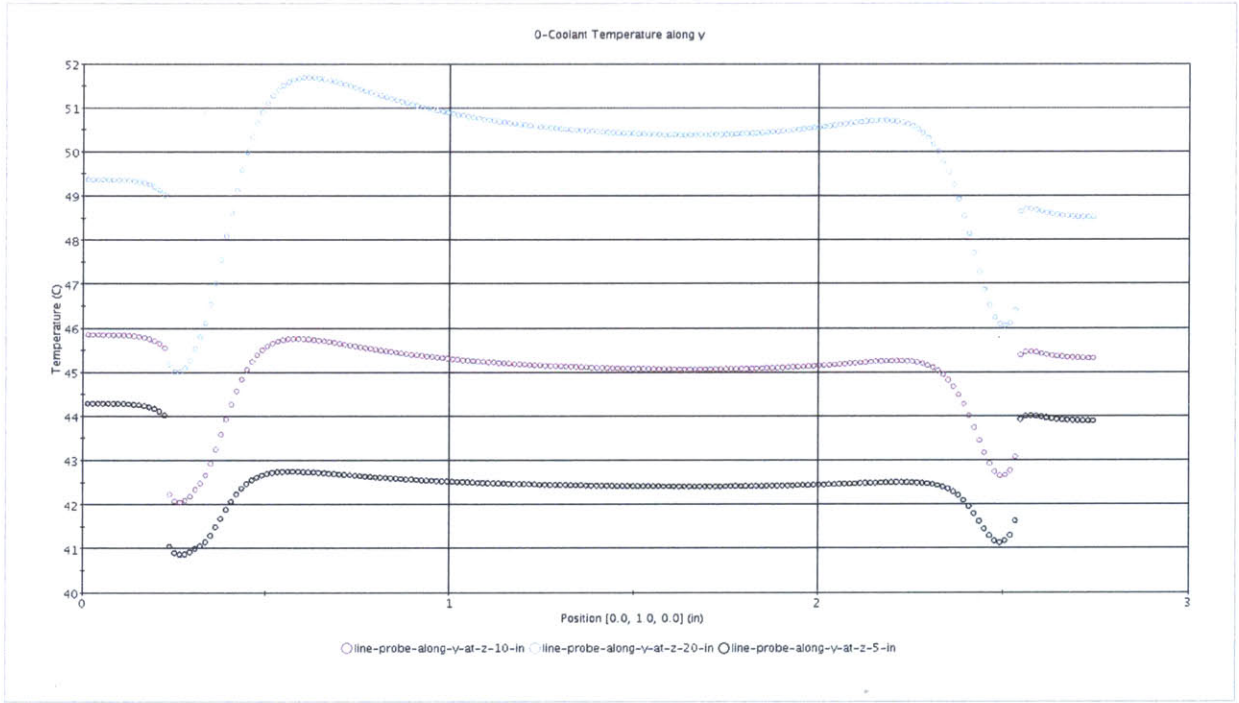

Figure 5.32 Temperature along the y direction in the middle of the half-coolant channel at various axial locations

Next, the heat flux at the cladding along the lateral direction is plotted at various axial locations (Figure 5.33). Since the flow is already fully developed at z = 5 in, the heat flux distribution does not change as the height is increased.

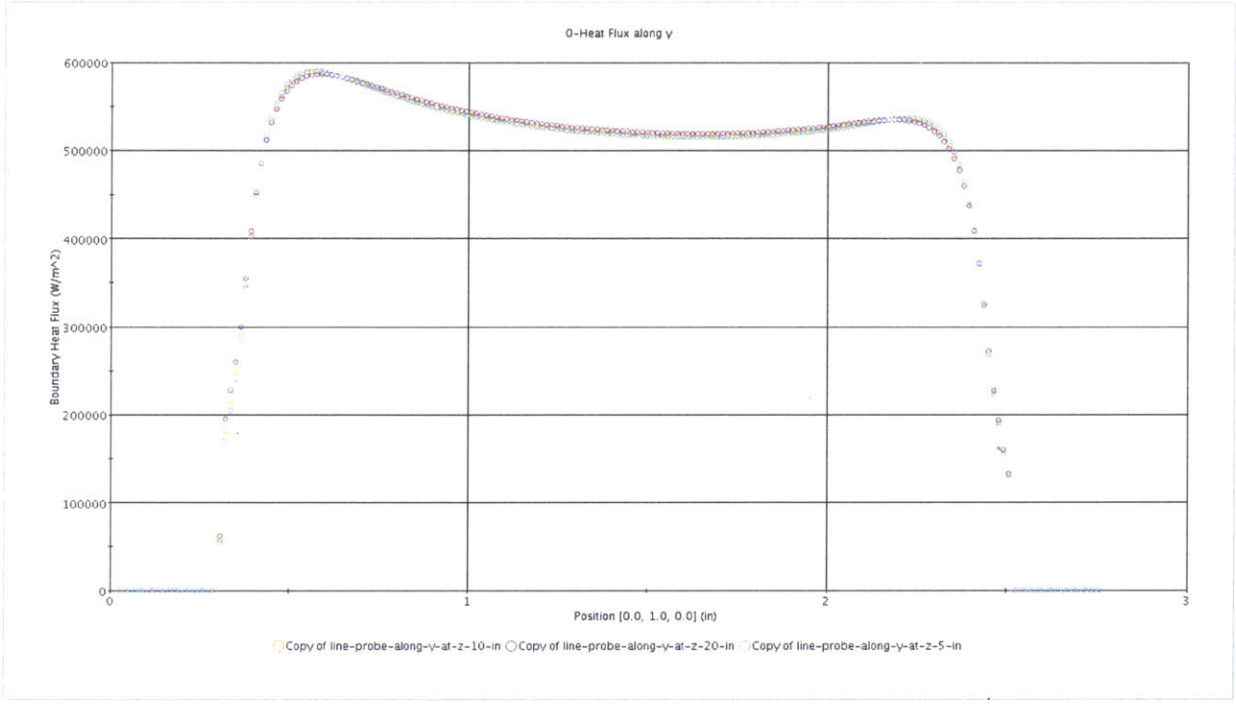

Figure 5.33 Heat flux along the y direction at various axial locations

Finally, the heat transfer coefficient based on the bulk coolant temperature of the whole channel is plotted along the y direction (following the line probe from Figure 5.20 restricted only to the cladding) at z = 20 in (Figure 5.34).

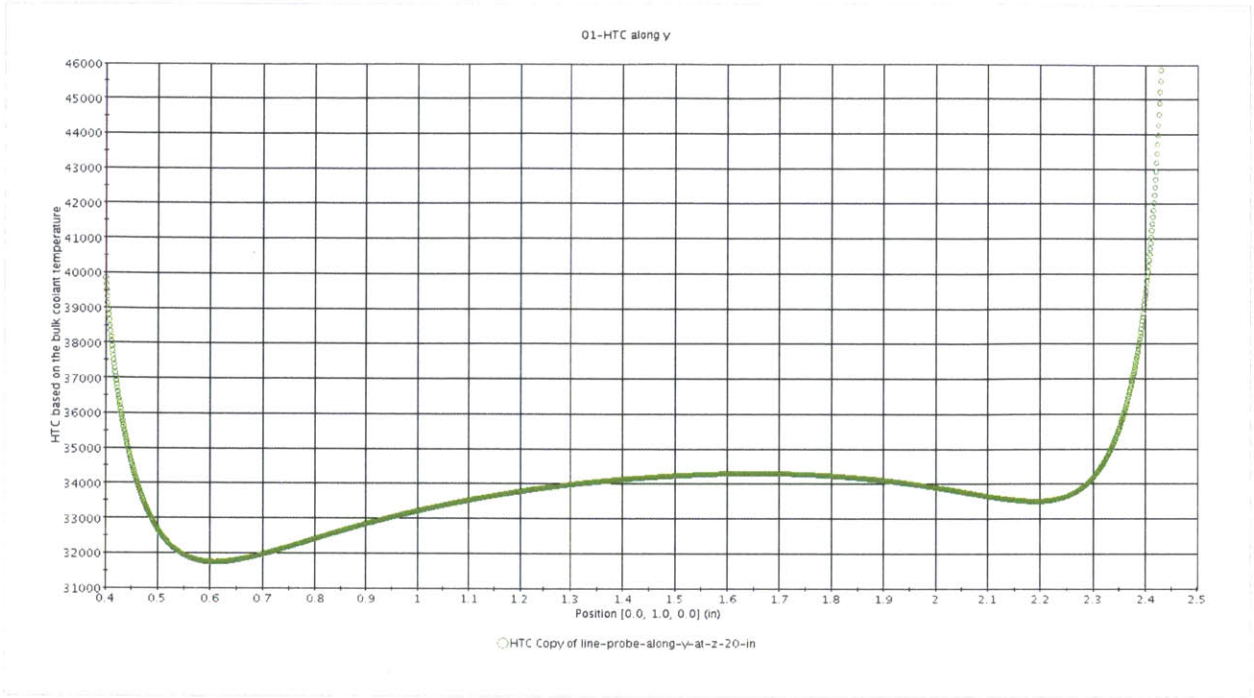

Figure 5.34 Heat transfer coefficient in the radial direction at z=20 in (T_{bulk} = 50.7 °C)

In order to better see the differences between the uniform and non-uniform cases, some of the plots are given side by side using the same scale (Figure 5.35). Also, the zoomed in sections are found in Figure 5.36.

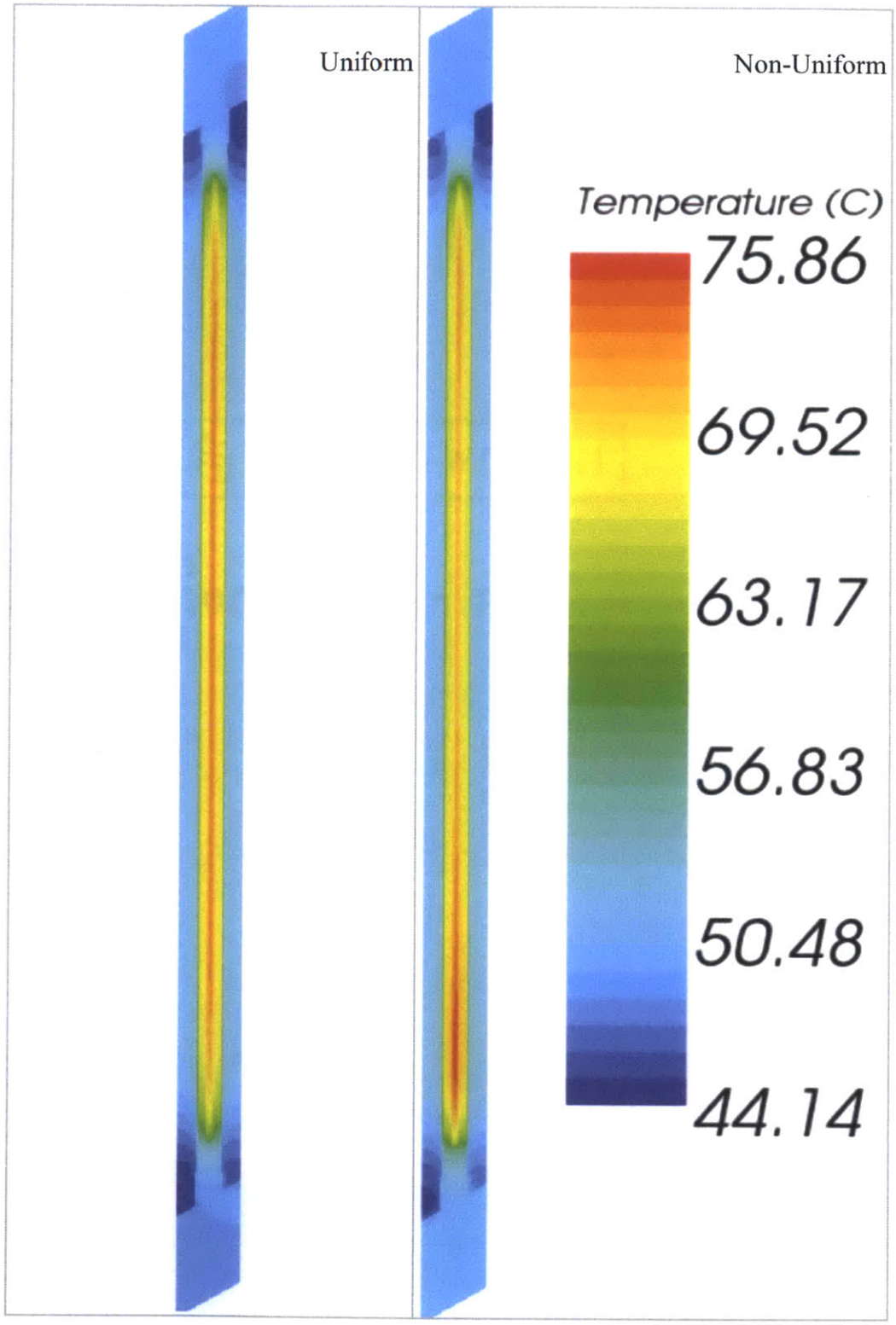

Figure 5.35 Temperature cross section at z = 20 in

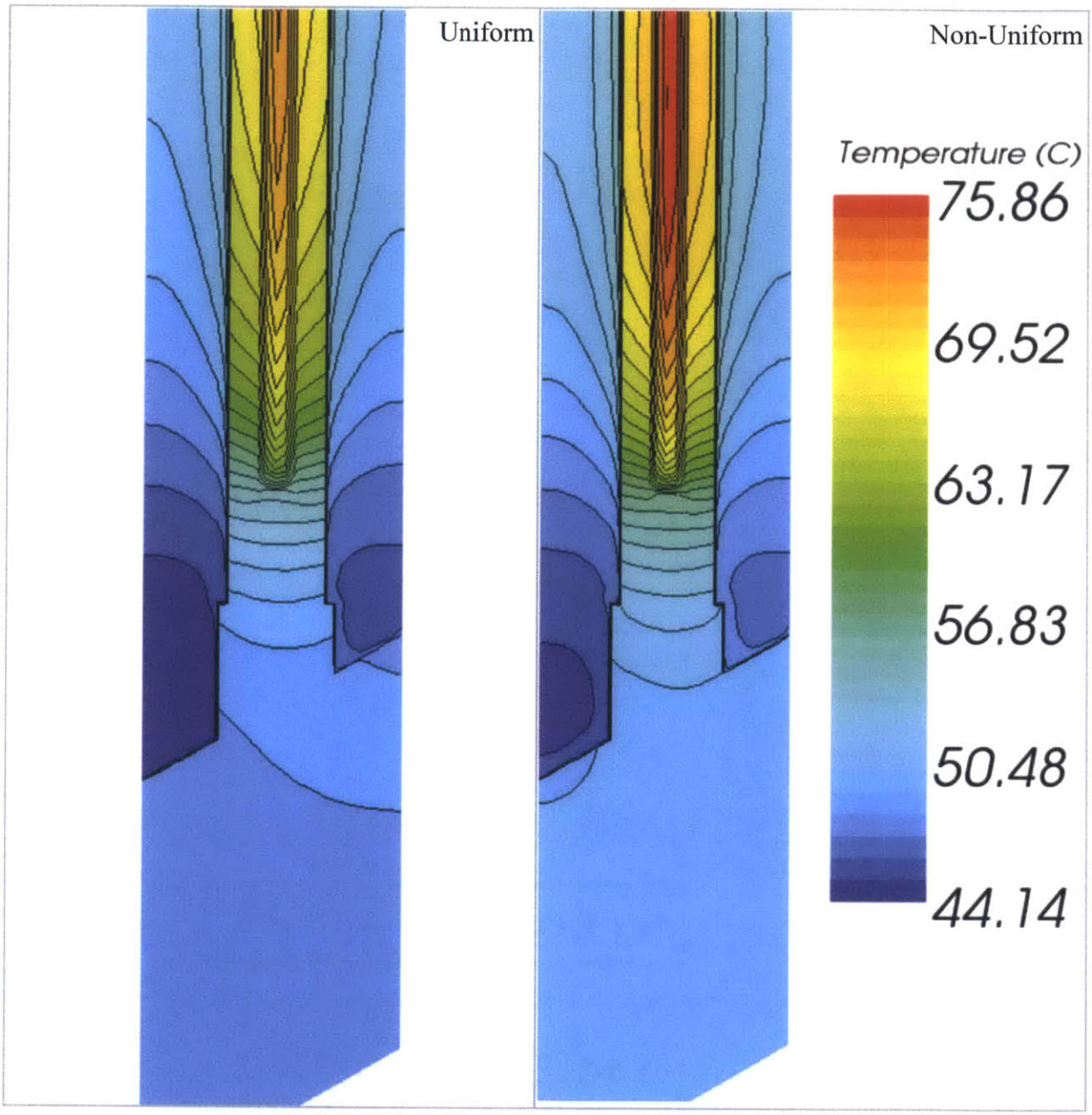

Figure 5.36 Zoomed in temperature cross section at z = 20 in

Next, the cladding temperature was plotted along the y-direction for both cases in Figure 5.37. The sensor line used for this plot was obtained by intersecting the cladding wall with a (x,y) plane perpendicular to it at z=20in.

Along the same line probe, the heat flux as a function of the y-direction was plotted for the uniform and non-uniform cases in Figure 5.38.

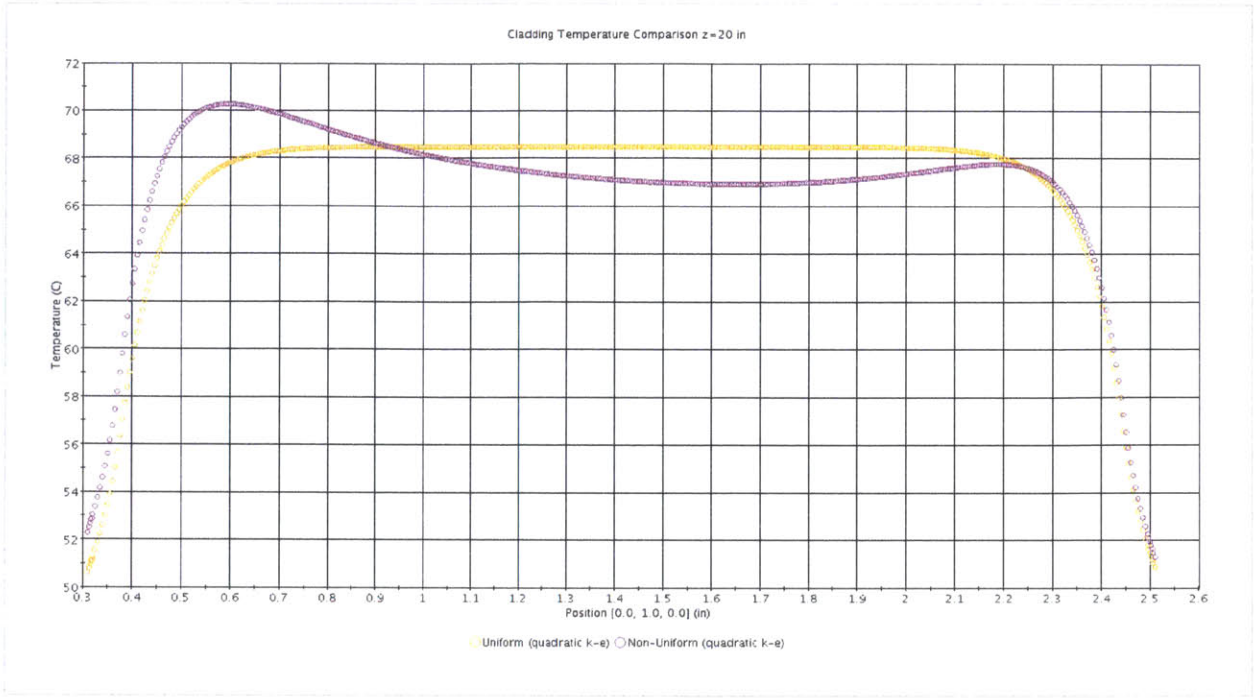

Figure 5.37 Cladding temperature along the y-direction at z = 20 in

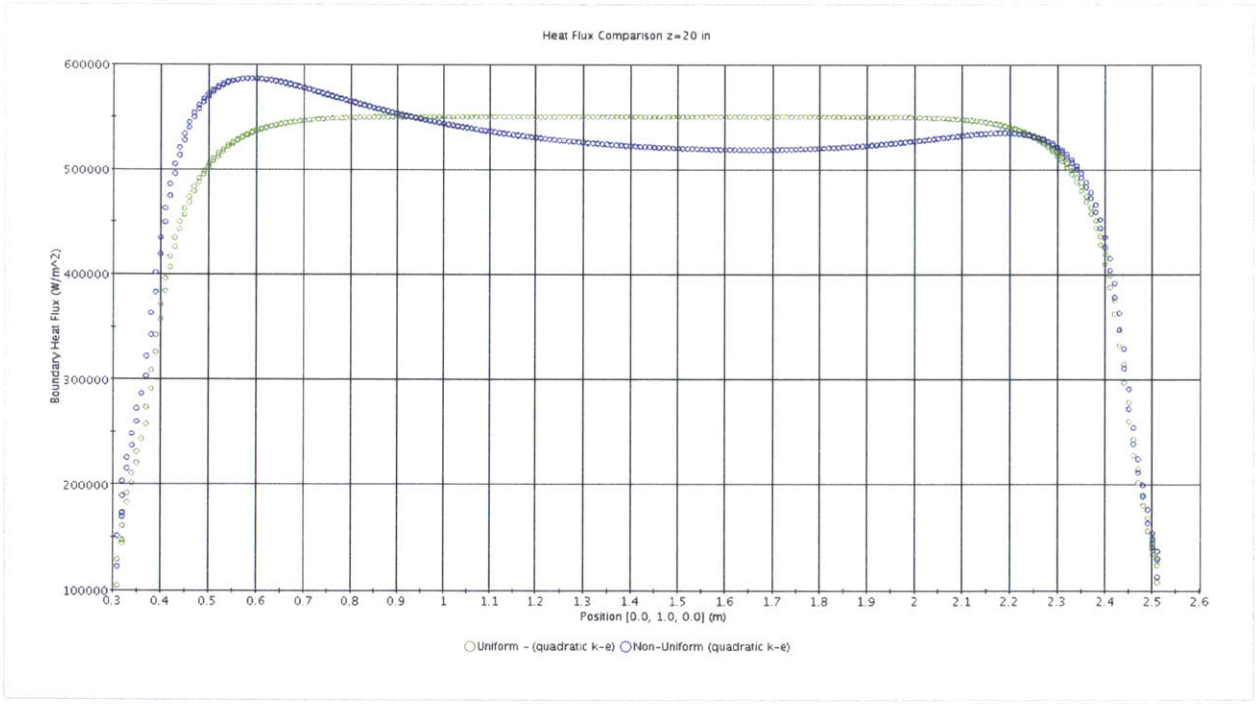

Figure 5.38 Heat flux along the y-direction at z = 20 in

Finally, the heat transfer coefficient based on the bulk coolant temperature (surface average over the whole coolant channel section at z=20in) and the local heat transfer coefficient were plotted

along the y-direction for both cases in Figure 5.39 and Figure 5.40. In Figure 5.39, the classic definition of the heat transfer coefficient was used:

$$h_{bulk} = \frac{q''}{T_w - T_{bulk}} \tag{6.1}$$

where T_W is the local cladding temperature.

Also, STAR-CCM+ has the built-in feature of plotting the local heat transfer coefficient evaluated at the centroid of the cell next to the boundary ($y=y_c$) as:

$$h_{local} = \frac{\rho_f(y_c) C_{p,f}(y_c) u^*}{T^+(y^+(y_c))} \tag{6.2}$$

where ρ_f and $C_{p,f}$ are the density and, respectively, the specific heat of the fluid.

The following non-dimensional quantities are also used in the definition:

$$y^+ = \frac{y u^*}{\nu} \tag{6.3}$$

$$t^+ = (T - T_w)\frac{\rho C_p u^*}{\dot{q}''} \tag{6.4}$$

where y is the normal distance from the wall to the wall-cell centroid, T is the wall-cell temperature, T_W is the wall-boundary temperature, q" is the wall heat flux, ν is the kinematic viscosity and u* is the reference velocity.

It is to be noted that, although the reference velocity is often related to the wall shear stress, $u^* = \sqrt{\tau_w/\rho}$, in practice, the reference velocity is derived from a turbulence quantity specific to the particular turbulence model.

Furthermore, Figure 5.39 includes the heat transfer coefficient, as defined in Appendix C, for the 16 stripes along the y-direction (for both uniform and non-uniform power distribution cases).

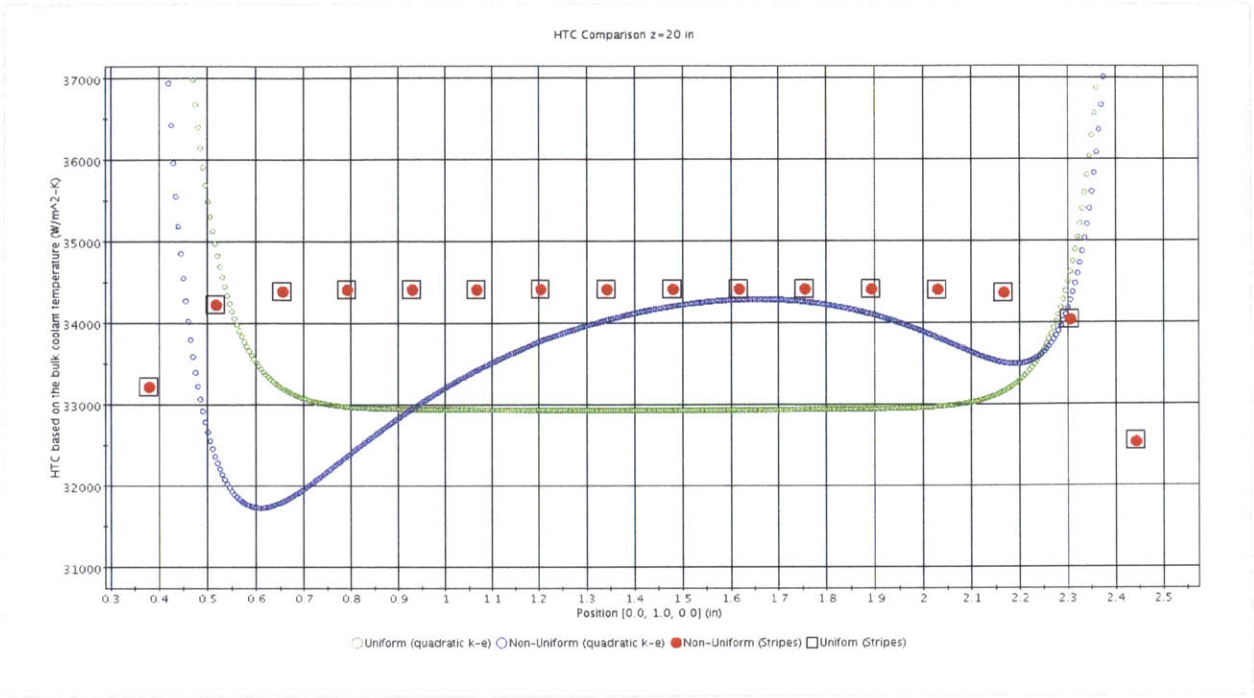

Figure 5.39 Heat transfer coefficient based on the bulk temperature of the full coolant channel along the y-direction at z = 20 in (T_{bulk} = 50.7 °C)

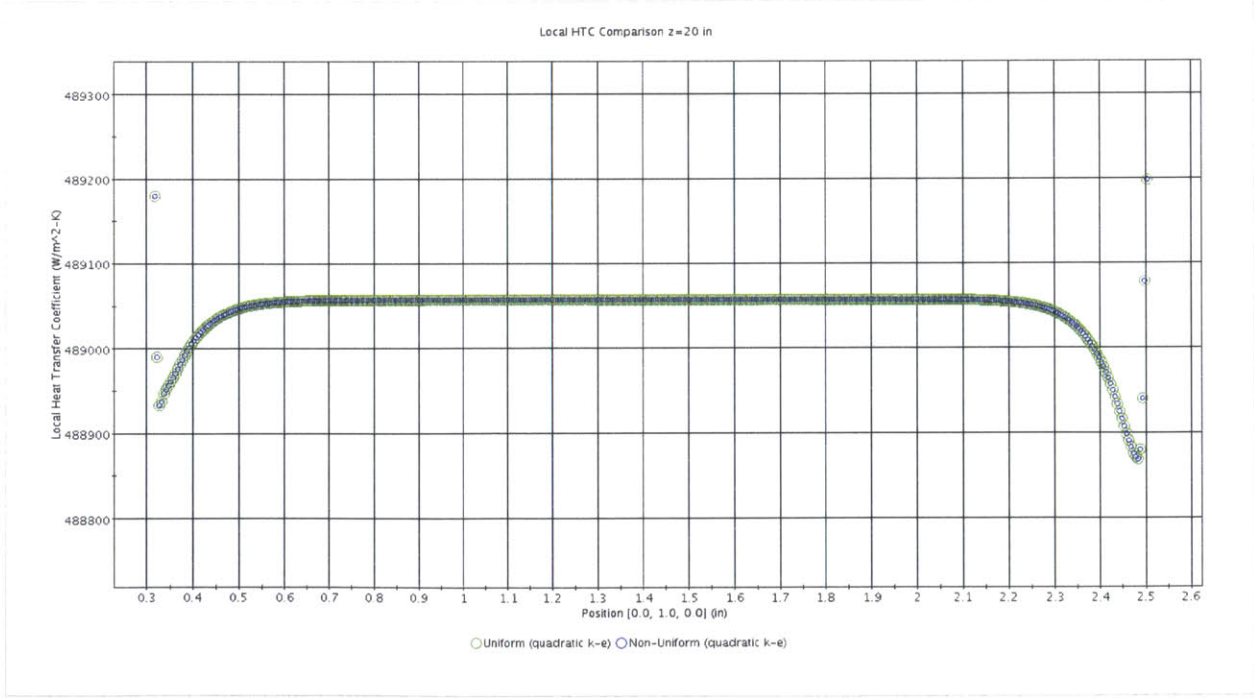

Figure 5.40 Local heat transfer coefficient along the y-direction at z = 20 in

It should be noted that the two heat transfer coefficient profiles for the 16 stripes from Figure 5.39 (uniform and non-uniform) overlap and show a similar behavior to the local heat transfer coefficient distributions from Figure 5.40. This is expected, as the local heat transfer coefficient is representative of the flow conditions (rather than the heating patterns), reflecting the lower velocity near the channel edges.

5.4.3 Fuel Meat Width Sensitivity Study

In order to observe the effects of the fuel meat width, its value was varied around the initial dimension derived from LEU81 (Table 5.6). Their geometry and mesh can be seen in Figure 5.41.

Table 5.6 Optimization of the fuel meat width

Simulation Number	Fuel meat width (in)
LEU81	2.082
LEU82	2.1385
LEU83	2.11025
LEU84	2.05375
LEU85	2.0255

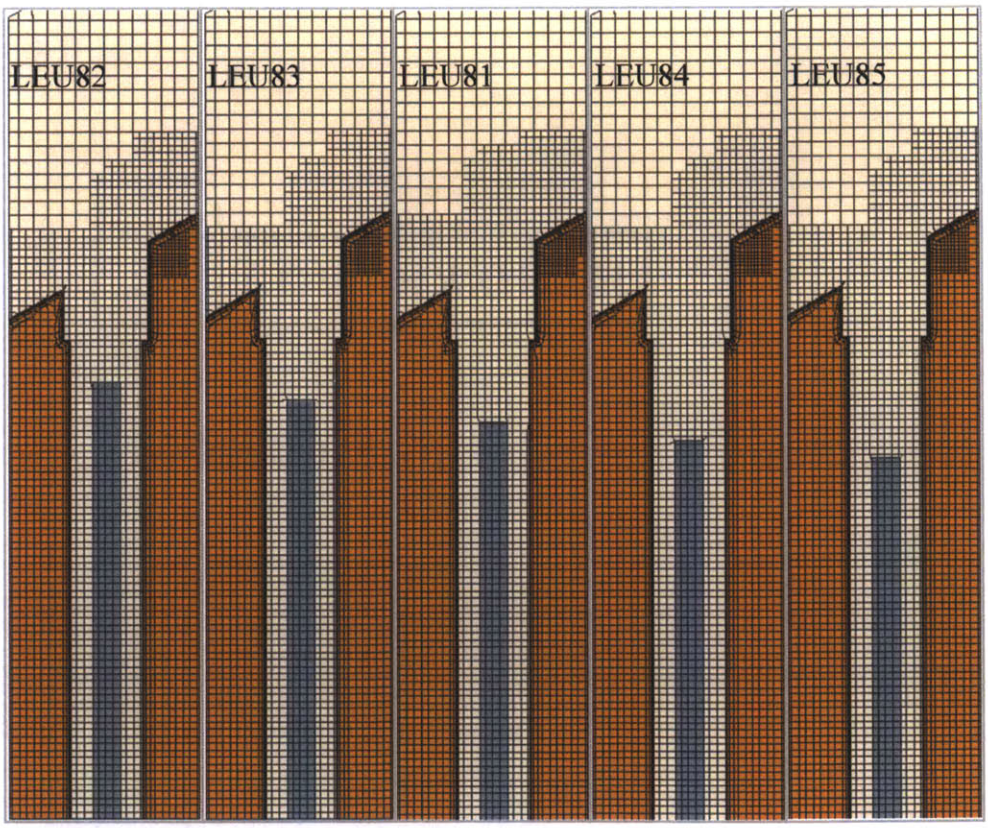

Figure 5.41 Zoomed in cross section in the (x,y) plane from the z direction (top)

The lateral power distribution was implemented as a function of the position y. Its plot can be seen in Figure 5.42. The biggest assumption made in this optimization process is that a small change in the geometry of the fuel meat is not reflected in the power distribution.

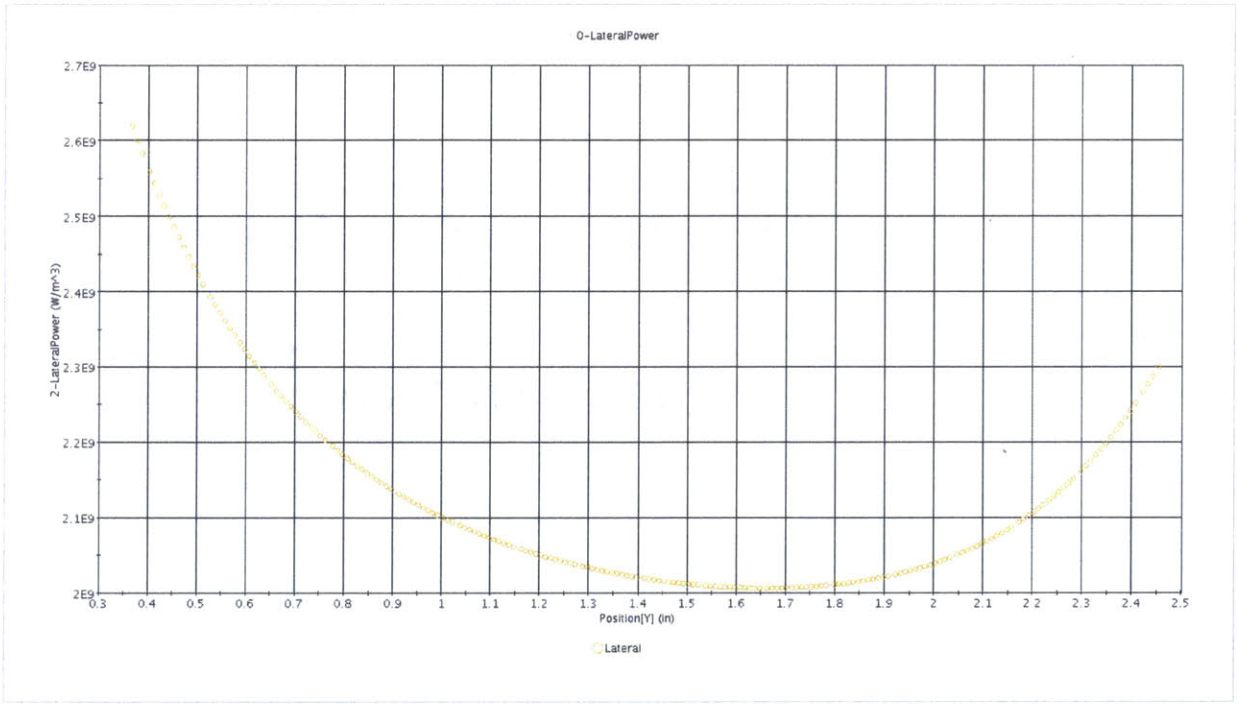

Figure 5.42 Lateral power distribution

The effects of the fuel meat width can be readily seen in the temperature profiles. Thus, in order to see the effect of conduction to the aluminum plate, a zoomed in temperature cross section is given in Figure 5.43.

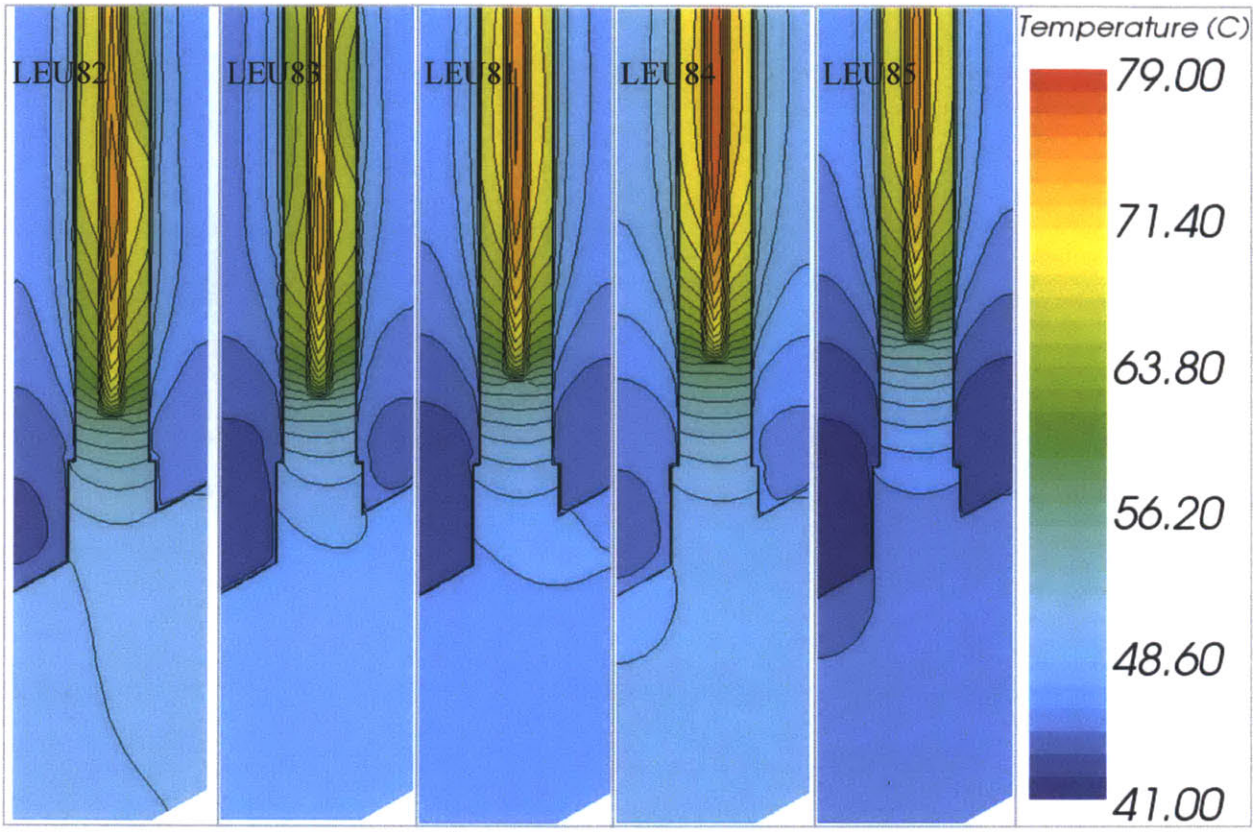

Figure 5.43 Zoomed-in temperature cross section at z=5 in

Next, the cladding temperature was plotted along the y-direction for four cases in Figure 5.44. The line probe used to obtain the data points goes through the aluminum plate at both ends (see Figure 5.20).

Along the same line probe, the heat flux as a function of the y-direction was plotted for three cases in Figure 5.45.

It can be concluded that a slight change in the fuel meat width does not significantly influence the temperature and heat flux patterns in the lateral direction. As shown in Table 5.6, the fabrication uncertainty of 0.1 inches fuel meat width would lead to <1 °C difference in peak cladding temperature.

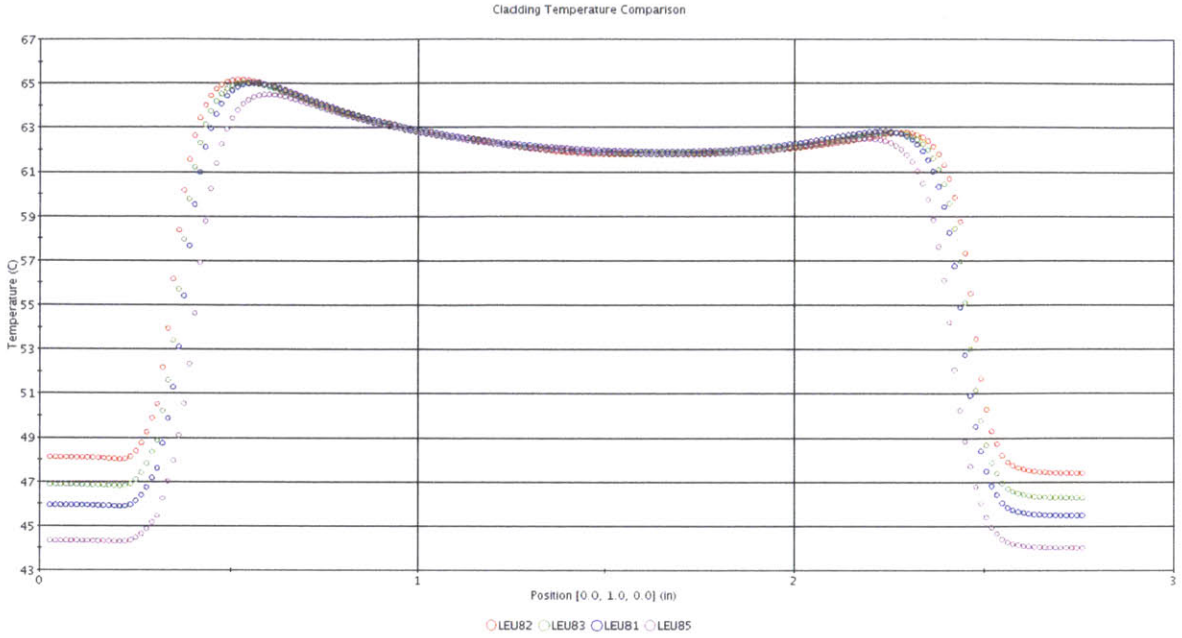

Figure 5.44 Cladding temperature along the y-direction at z=5in

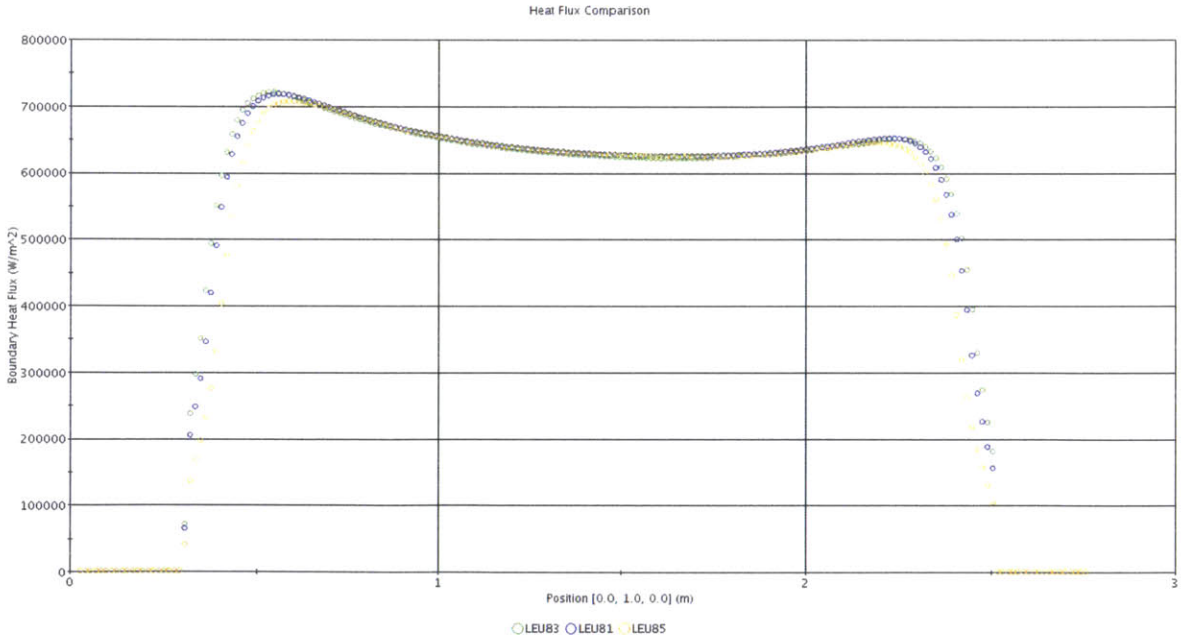

Figure 5.45 Heat flux along the y-direction at z=5in

6. Quasi Direct Numerical Simulation of smooth channel flow

The second objective of this project is to study and quantify the effect of the longitudinal grooves designed with the aim of improving the heat transfer from the cladding to the coolant. Given that the size of the grooves is comparable to the viscous sublayer thickness, it is extremely difficult to effectively quantify and validate the heat transfer improvement. The heat transfer augmentation is expected to be generated by an increased turbulence. Nonetheless, no quantification have been found in literature for the effect of the grooves; therefore, a direct numerical simulation approach is the only available alternative to detailed experiments.

The STAR-CCM+ code has used to simulate in a quasi-DNS fashion the effect of the grooves. In this section, a quasi-DNS calculation of a turbulent periodic smooth channel flow with non-conjugate heat transfer is shown to validate this approach against known databases.

6.1 Geometry and Meshing

A single rectangular parallelepipedic domain was used to simulate the flow between two infinite parallel plates. An essential part of an accurate and optimally fast DNS calculation is the selection of the minimal domain proportions. In order to accommodate two streamwise vortices, a computational domain (Figure 6.1) was chosen with the sizes: $L_x = 6.4 \times h$ (streamwise), $L_y = 2 \times h$ and $L_z = 3.2 \times h$ (spanwise) in the three directions, where h is the channel half-width or the channel characteristic length (Table 6.1).

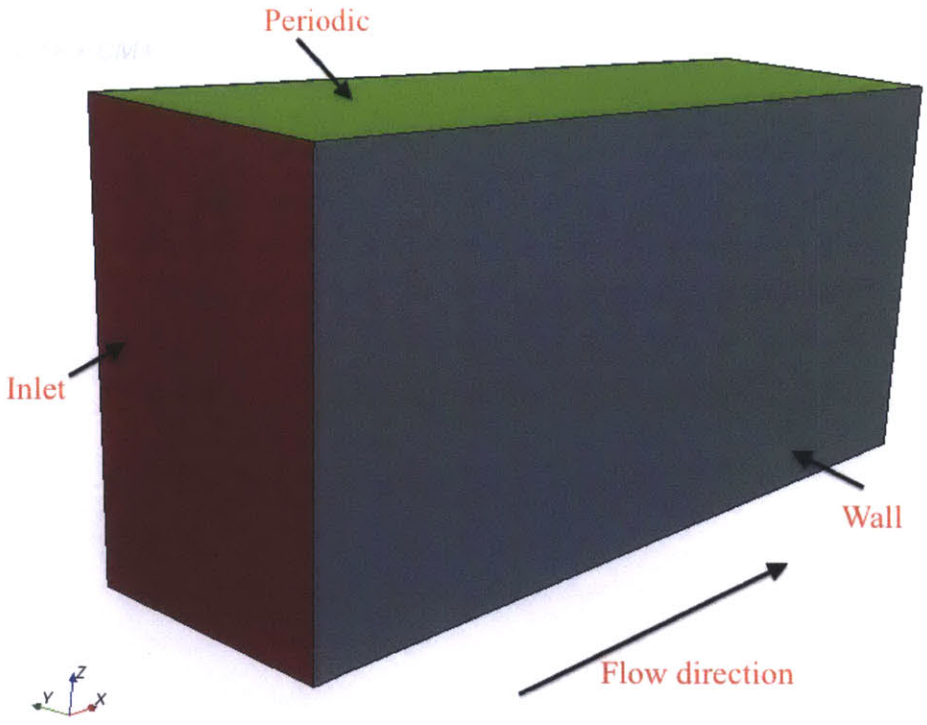

Figure 6.1 Smooth channel computational domain for quasi-DNS

Table 6.1 Geometry of smooth channel

Characteristic Length (m)	Wall Surface Area (m^2)	Cross Section Area (m^2)
1.0414	22.21	6.941

Moreover, aside from the domain and numerical schemes, the mesh is as important for an accurate DNS analysis. In order to have as little dissipative and dispersive error, a structured type mesh is desirable. The computational grid contained 253×96×253 points in the x-, y- and z-directions. The grid was uniform in the streamwise and spanwise directions, and the corresponding resolution, in dimensionless units, was $\Delta x^+=10$ and $\Delta z^+=5$ in order to resolve the smallest structures of turbulence. In the cross-direction, a non-uniform mesh based on a two-sided hyperbolic function was used, with the overall stretching factor F constant such that $\Delta y^+(min)=0.8$ at the wall and the ratio between two neighboring cells would not larger than 1.1. This requirement gives F=2.31 and $\Delta y^+(max)=19.41$ near the centerline. This can be seen in Figure 6.2 with a close up near the wall in Figure 6.3. This approach resulted in a grid with approximately 6.1 million cells.

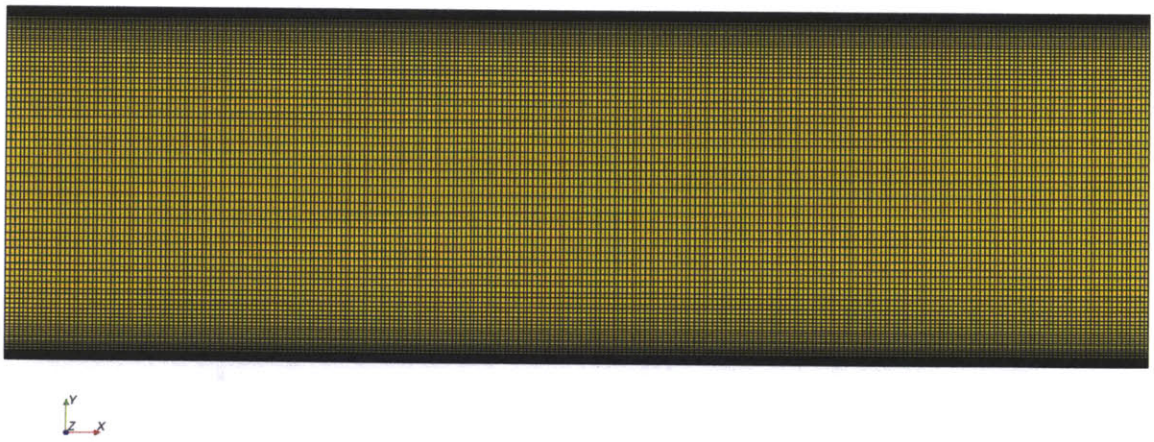

Figure 6.2 Grid used for the smooth channel quasi-DNS simulation

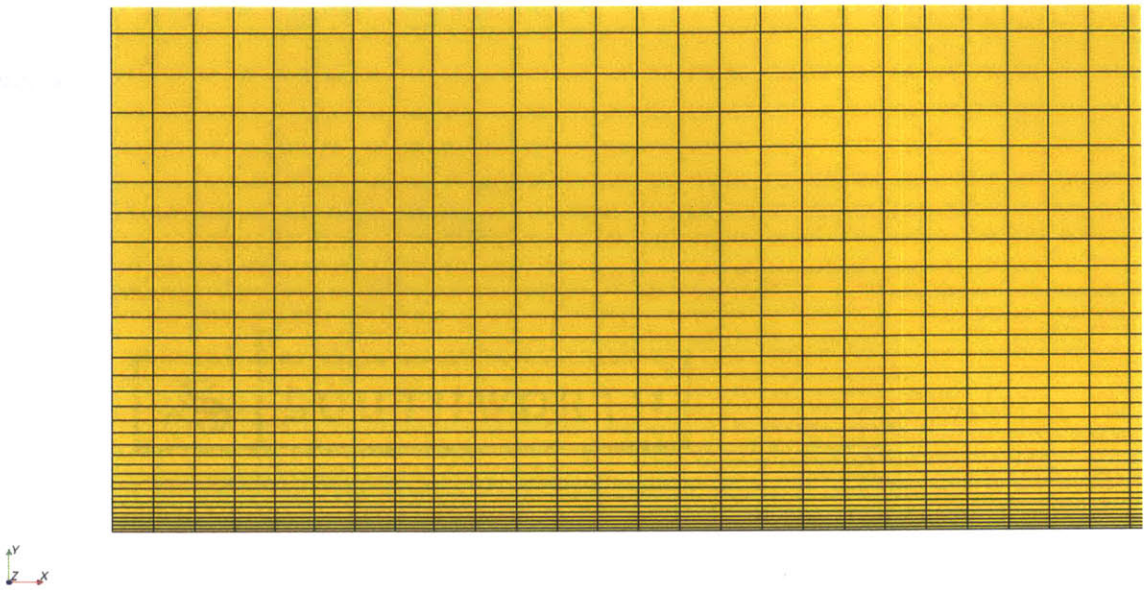

Figure 6.3 Near the wall close up of the grid used for the smooth channel quasi-DNS simulation

6.2 Boundary conditions

Firstly, no slip with constant uniform heat flux boundary conditions were imposed at the walls (Figure 6.1).

Secondly, in the z-direction, a periodic internal interface boundary condition was set in order to replicate two-infinite parallel walls (the walls being perpendicular to the y-direction).

Finally, in the x-direction, that is the streamwise direction, the periodic boundary conditions are very important for sustaining turbulence in a DNS simulation. Given that the flow is periodic in the streamwise direction and heat is added to the wall as constant heat flux, the pressure and temperature are not periodic. For example, since a constant heat flux was added to the wall, a constant increase in the temperature of the fluid from the inlet to the outlet is expected. Therefore, for periodicity, the amount of heat added to the fluid needs to be subtracted at the outlet boundary and the same fluid temperature profile needs to be used as input back at the inlet. Also, the drag from the wall will cause a drop in pressure in the streamwise direction. STAR-CCM+ allows for such modeling capability by setting the interface between the inlet and outlet boundaries as fully developed and by imposing a specific mass flow rate though the channel and a bulk inflow temperature. In order to validate this approach against the known DNS databases (e.g. Kasagi, Kawamura) a reference Reynolds number (Re) of 14000 (equivalent to a shear Reynolds number (Re_τ) of 396) was set by imposing a mass flow rate appropriate for the fluid properties used (Table 6.1). This Reynolds number is also characteristic of the MIT Reactor flow conditions, while the heat flux was rescaled from the RANS analysis.

6.3 Initial conditions

The desired flow for this test case is a fully developed turbulent wall-bounded flow where it is verified that the transient effects have been lost. In order to achieve this requirement, the initial flow field must be carefully chosen in order to speed up the solution time. One way to solve this problem is to take an instantaneous field from a previous simulation, but STAR-CCM+ has a built in feature which creates synthetic turbulence given two specific parameters: the turbulence intensity and the turbulence length scale. In this case, a turbulent intensity of 0.2 and turbulence length scale of h/5 were chosen (Table 6.2).

Table 6.2 Initial flow conditions parameters and fluid properties for smooth channel

Parameter	Value
Re_τ	395.76
Re	13924.9
Pr	6
h [m]	1.0414
Density [kg/m^3]	997.561
Dynamic Viscosity [kg/(s-m)]	8.8871E-4
Thermal Conductivity [W/(m-K)]	0.620271
Specific Heat [J/(kg-K)]	4181.72
Turbulence Intensity	0.2
Turbulence Length Scale	h/5
Wall Heat Flux [W/m^2]	481994.7
Streamwise Cross Section Area [m^2]	6.940889
Mass Flow Rate [kg/s]	41.24
Bulk Inflow Temperature [°K]	300

6.4 Results and Validation

The domain was chosen to resemble the domain and mesh used by Kawamura [13], except that more cells were used in the wall-normal direction. The time step chosen, the start-up and averaging procedure are the result of a sensitivity analysis. A few flow throughs were used for start-up and were neglected when statistics were collected, as a statistically steady state was achieved relatively quickly.

For the convergence verification analysis, the following mean (time-averaged) quantities were point monitored at the center of the domain: U, V, W, UU, UV, UW, VV, VW, WW. Also, the turbulent kinetic energy of the entire domain was monitored for convergence. Initially, it was estimated that about 50 flow-throughs would be required for convergence; the simulation was stopped after 53 flow-throughs. For example, the convergence of U and V are shown in Figures 6.4-6.5, where the streamwise velocity converges to a fixed positive value, while the transversal velocity reaches zero as expected (no flow in the direction between the walls).

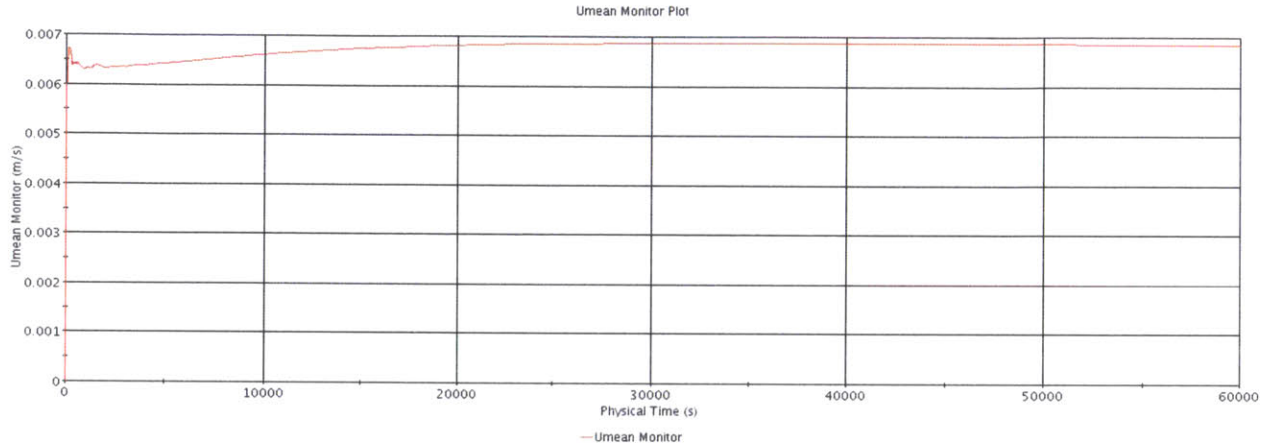

Figure 6.4 Monitor plot of the mean streamwise velocity (U) at the center of the flow domain

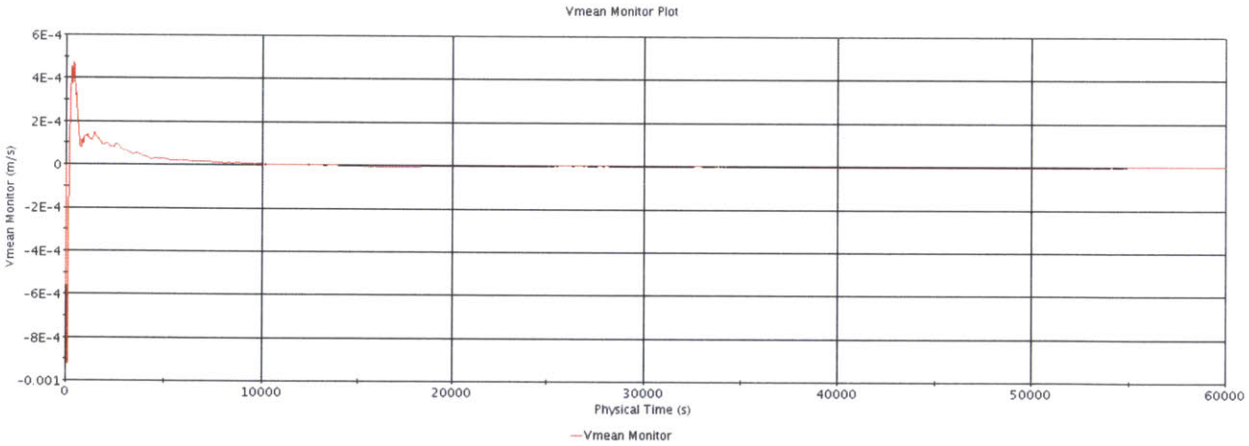

Figure 6.5 Monitor plot of the mean transversal velocity (V) at the center of the flow domain

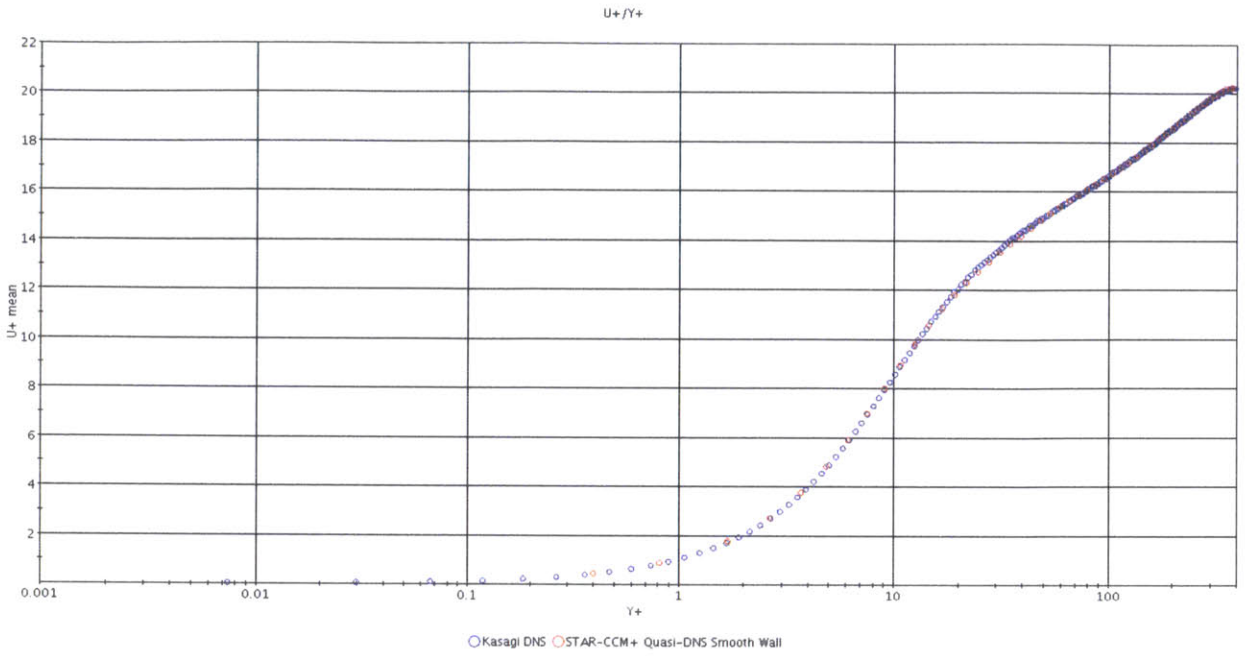

Figure 6.6 Mean streamwise velocity profile from quasi-DNS at Re_τ=395.76

For validation, the mean streamwise velocity profile from the quasi-DNS simulation is compared to the DNS results of Kasagi that were obtained under the same conditions (Figure 6.6). It can be seen that the quasi-DNS results are in agreement with the DNS database with a maximum deviation at the center of the channel of 0.2%.

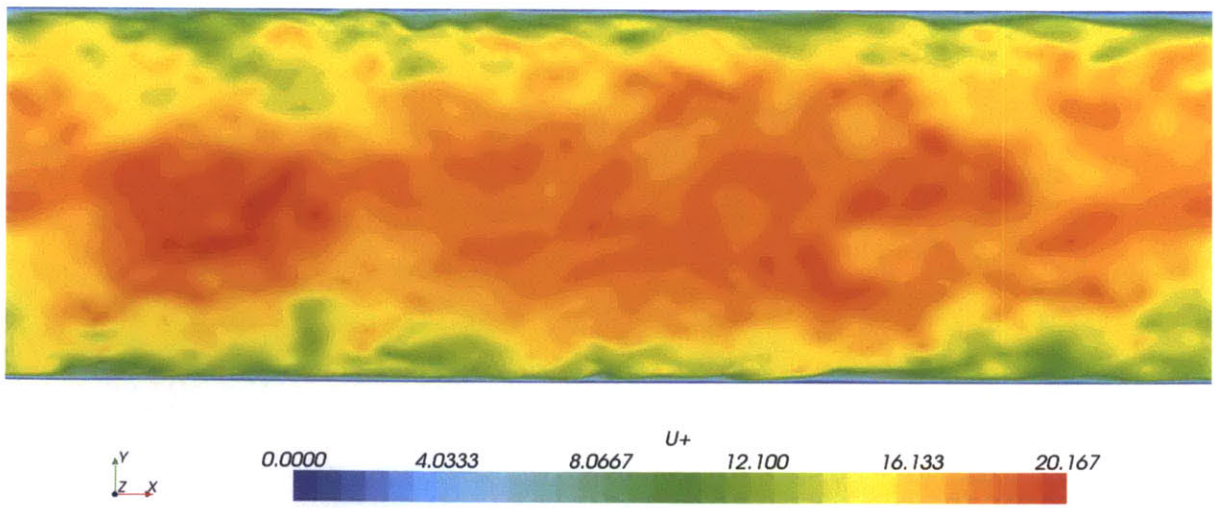

Figure 6.7 Instantaneous non-dimensional streamwise velocity in the entire domain for smooth channel

A cross section in the wall-normal direction of the instantaneous non-dimensional streamwise velocity is shown in Figure 6.7.

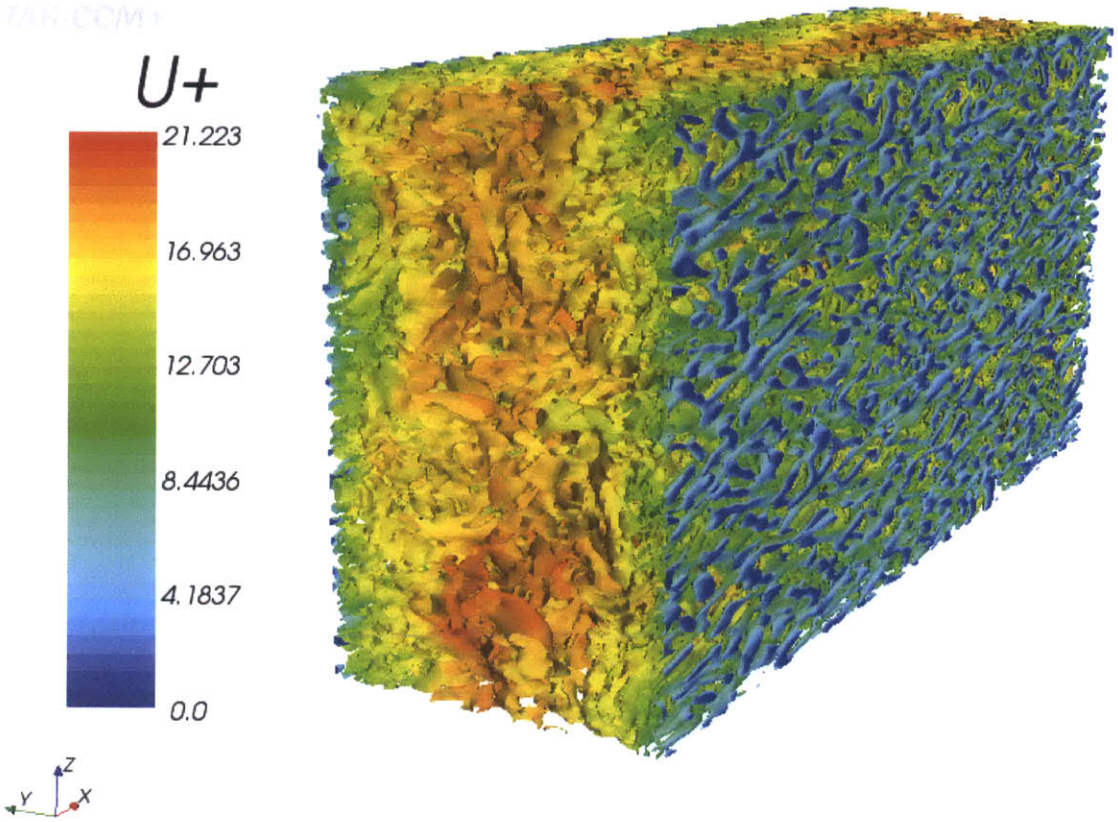

Figure 6.8 Iso-surface of Q-criterion colored with U+

In Figure 6.8, the iso-surfaces of Q-criterion colored with U+ are shown in order to qualitatively show the mixing of the flow structures. Hair pin vortices can be observed along the flow direction.

In Table 6.3, a few flow relevant quantities were post-processed in order to be further used in comparison with the grooved channel case.

Table 6.3 Flow results for smooth channel

Average Velocity (m/s)	Pressure Drop (Pa)	Skin friction coefficient	Mass flow rate (kg/s)	τ-wall
5.96E-03	**7.24E-04**	**0.0051**	**41.20**	**1.138E-04**

The skin friction coefficient is defined as:

$$C_f \equiv \frac{\tau_w}{\frac{1}{2}\rho U_\infty^2} \tag{6.1}$$

where τ_W is the local wall shear stress, and $\mathbf{U}_\infty$ is the free-stream velocity, that is the velocity outside the boundary layer.

Given the non-conjugate heat transfer approach, the temperature profile could not be accurately simulated; however, the average thermal properties (i.e. the aim of this analysis) could still be obtained. In Table 6.4, the temperature difference between the wall and bulk fluid, the heat transfer coefficient and the Nusselt number are given. For additional validation, the Kawamura database [13] was used to confirm the results: as is shown in Table 6.4, the quasi-DNS result is off by only 2% from the DNS result obtained under the same conditions.

Table 6.4 Thermal results for smooth channel

ΔT (°K)	quasi-DNS HTC	quasi-DNS Nu	DNS Nu*
15.7	30,700	103	101

***Kawamura Re=14124, Pr=6 (4th order central difference scheme)**

Moreover, an experiment performed at MIT in which a thermal hydraulic loop with a heated, full-scale, smooth coolant channel at the operating conditions of the MITR was used to measure the single phase heat transfer coefficient for different Re number regimes [14]. In the paper, the results were also compared to the existing correlations commonly used in the literature. In Figure 6.9, it can be seen that the quasi-DNS result falls between the uncertainty boundaries of the experimental data. Therefore, the quasi-DNS approach was not only validated against DNS databases, but also against an experiment that was run under similar conditions.

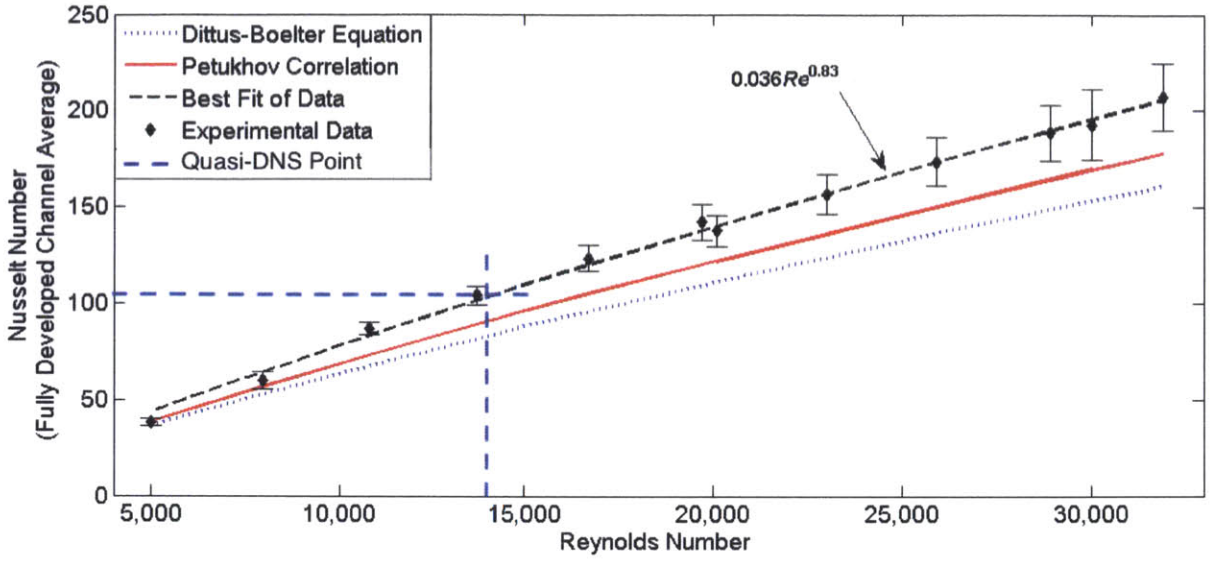

Figure 6.9 Fully developed, channel average Nusselt number for a narrow rectangular channel [14] and the data point obtained from the quasi-DNS for smooth channel

7. Quasi Direct Numerical Simulation of grooved channel flow

Having validated the quasi-DNS approach for a smooth channel flow in the previous section, a quasi-DNS calculation of the grooved channel flow will be used in order to compare it to the smooth channel flow case and, ultimately, quantify the heat transfer augmentation.

7.1 Geometry and Meshing

In Figure 7.1, the grooved channel computational domain is shown. The groove width and height correspond to the MIT Reactor real size of 10 mil, but scaled up 1000 times to match the dimensions of the smooth channel (Table 7.1). The characteristic length (h) is measured in the y-direction from the middle of the channel up to the middle of the groove. Moreover, in order to keep the periodicity in the z direction, the edge was cut through the middle of the groove.

Table 7.1 Geometry of grooved channel

Characteristic Length (m)	Groove Width/Height (m)	Wall Surface Area (m^2)	Cross Section Area (m^2)
0.98425	**0.0254**	**50.58**	**6.998**

The domain proportions from the smooth channel case were appropriately conserved: $L_x = 6.4 \times h$ (streamwise), $L_y = 2 \times h$ and $L_z = 3.2 \times h$ (Figure 7.1).

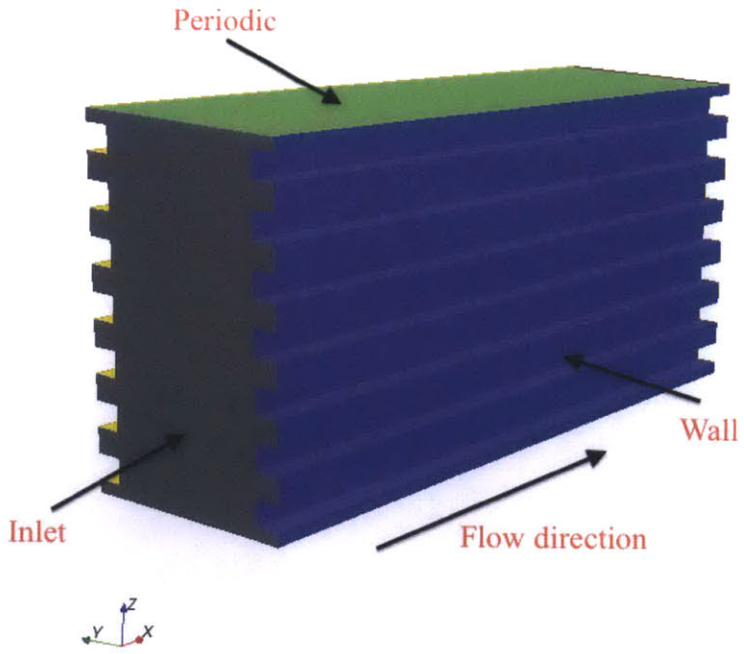

Figure 7.1 Grooved channel computational domain for quasi-DNS

The computational grid is more complicated than in the smooth channel case because the addition of the grooves at the wall requires more refinement. The grid was uniform in the streamwise direction, and the corresponding resolution, in dimensionless units, was $\Delta x^+=10$. In the spanwise direction in the groove and between the grooves, a non-uniform mesh based on a two-sided hyperbolic function was used, with the overall stretching factor F constant such that $\Delta z^+(min)=0.8$ at the wall and the ratio between two neighboring cells would not be larger than 1.1. This requirement gives F=1.3 and $\Delta z^+(max)=2.96$ near the centerline. This can be seen in Figure 7.2, with a close up near the groove in Figure 7.3. Finally, in the cross-direction, two different grids were used in the groove and between the grooves. In the grooves, a uniform grid with $\Delta y^+=0.8$ was used giving 113 cells and, between the grooves, a non-uniform mesh based on a two-sided hyperbolic function with the overall stretching factor F constant such that $\Delta y^+(min)=0.8$ at the wall and the ration between two neighboring cells would not be larger than 1.1. This requirement gives F=1.8 and $\Delta y^+(max)=7.63$ near the centerline.

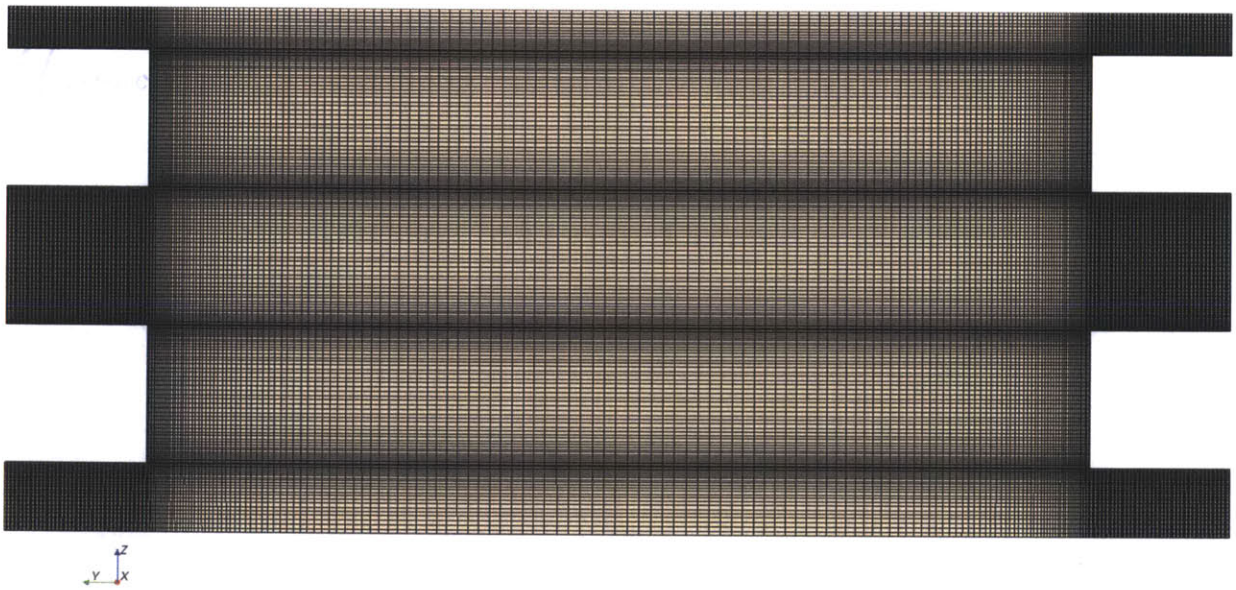

Figure 7.2 Grid used for the grooved channel quasi-DNS simulation

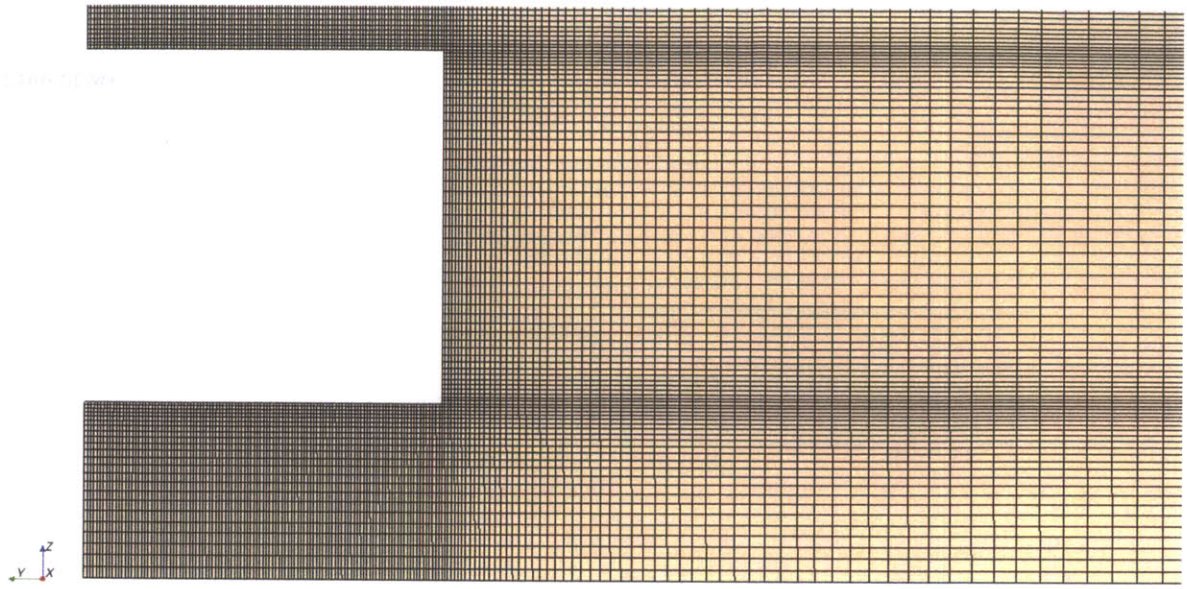

Figure 7.3 Near the groove grid used for the grooved channel quasi-DNS simulation

Overall, the total number of cells was approximately 43 millions cells.

7.2 Initial and boundary conditions

The initial and boundary conditions were preserved from the smooth channel simulation such that they accommodate the addition of grooves to the computational domain.

Table 7.2 Initial flow conditions parameters and fluid properties for grooved channel

Parameter	Value
Re_τ	395.76
Re	13924.9
Pr	6
h [m]	0.98425
Groove Width [m]	0.0254
Number of Grooves	14
Density [kg/m^3]	997.561
Dynamic Viscosity [kg/(s-m)]	8.8871E-4
Thermal Conductivity [W/(m-K)]	0.620271

Parameter	Value
Specific Heat [J/(kg-K)]	**4181.72**
Turbulence Intensity	**0.2**
Turbulence Length Scale	**h/5**
Wall Heat Flux [W/m^2]	**481994.7**
Streamwise Cross Section Area [m^2]	**6.998**
Mass flow Rate [kg/s]	**44.01**
Bulk Inflow Temperature [°K]	**300**

7.3 Results

The start-up and averaging procedure were similar to the smooth channel case and the same quantities were used to check for convergence: U, V, W, UU, UV, UW, VV, VW, WW. The simulation was run for 150 flow-throughs. For example, the convergence of U is shown in Figure 7.4.

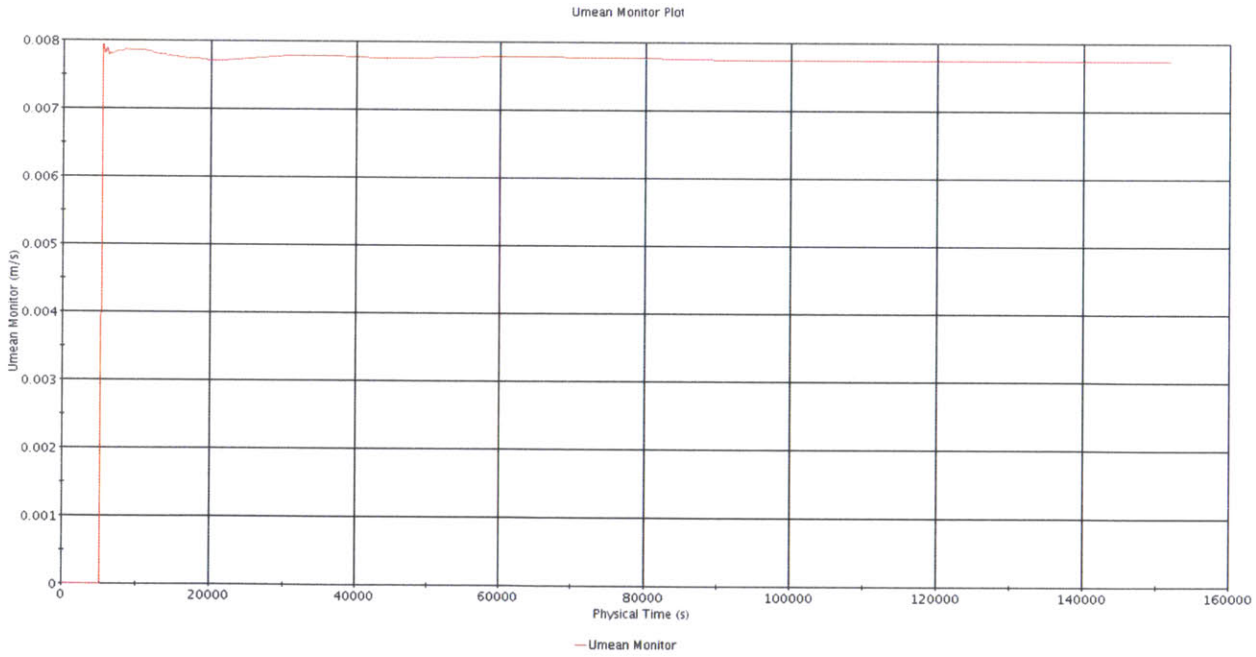

Figure 7.4 Monitor plot of the mean streamwise velocity (U) at the center of the flow domain

In Figure 7.5, the iso-surfaces of Q-criterion colored with U+ are shown in order to show the mixing of the flow structures on a qualitative basis. The same hair pin vortices as in the smooth

channel simulation can be observed along the flow direction; however, these vortices become constrained in the grooves. This leads to the creation of small stagnation zones in the transversal corners of the grooves (Figure 7.7).

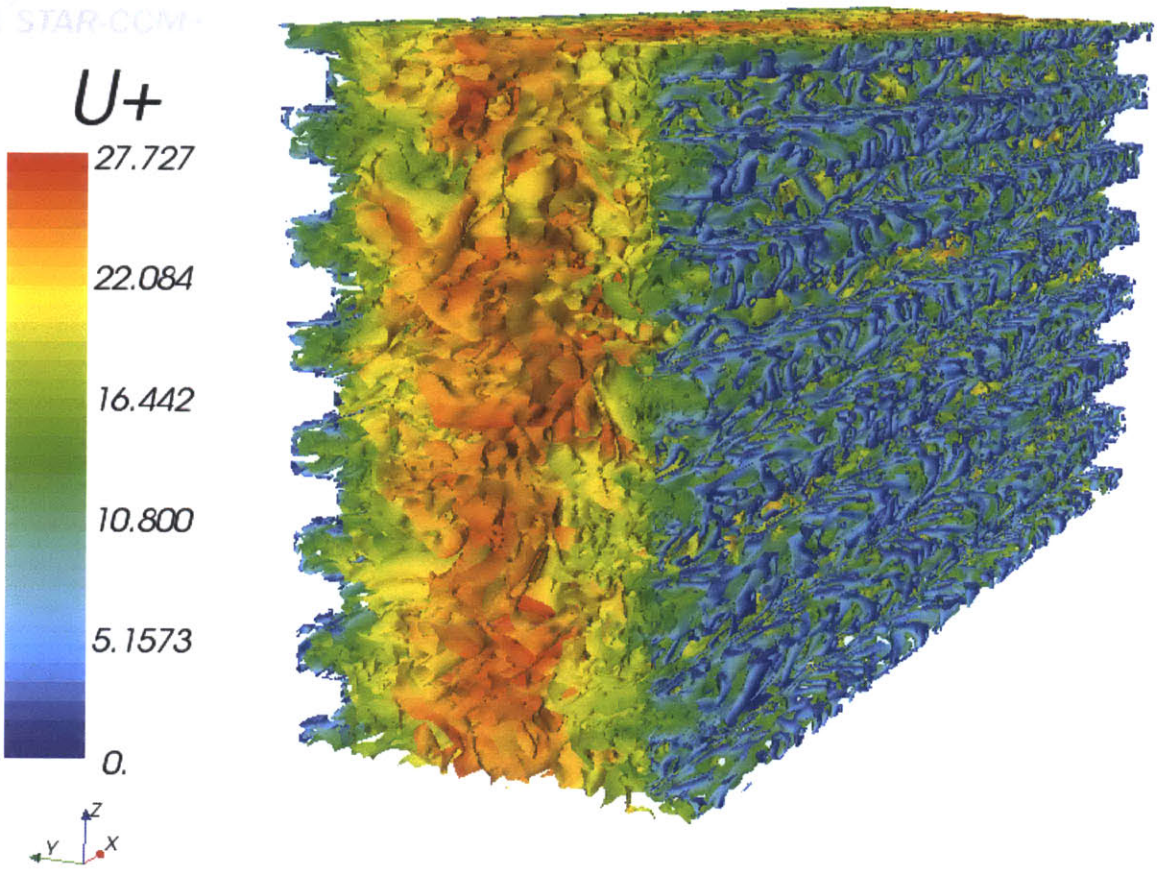

Figure 7.5 Iso-surface of Q-criterion colored with U+

A cross section in the wall-normal direction of the instantaneous non-dimensional streamwise velocity is shown in Figure 7.6, while in Figure 7.7 the mean non-dimensional streamwise velocity in a plane perpendicular to the streamwise direction is shown. It can be seen that the presence of grooves leads to an effective decrease in the flow velocity near the walls, especially in the corners of the grooves.

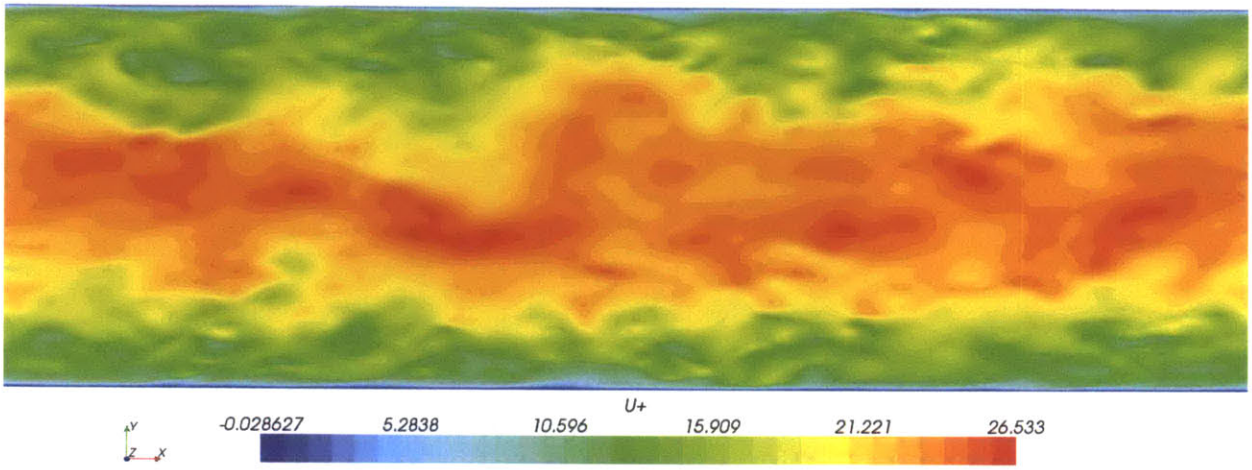

Figure 7.6 Instantaneous non-dimensional streamwise velocity in a plane perpendicular to the spanwise direction cutting through the middle of the groove for grooved channel

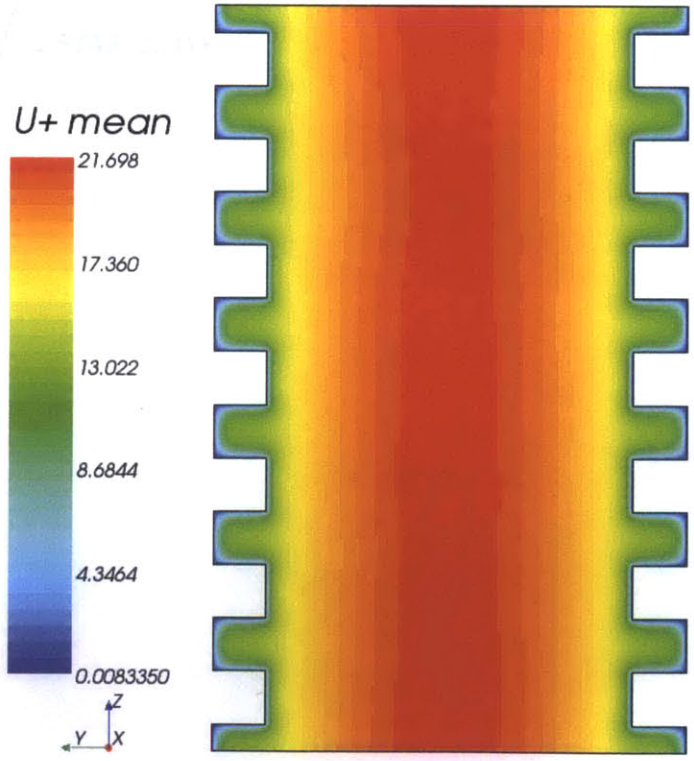

Figure 7.7 Mean non-dimensional streamwise velocity in a plane perpendicular to the streamwise direction for grooved channel

In Table 7.3, a few flow relevant quantities were post-processed for further use in the comparison with the smooth channel case.

Table 7.3 Flow results for grooved channel

Average Velocity (m/s)	Pressure Drop (Pa)	Skin friction coefficient	Mass flow rate (kg/s)	τ-wall
6.30E-03	1.71E-03	0.00407	44.01	1.199E-04

In Table 7.4, the temperature difference between the wall and bulk fluid, the heat transfer coefficient and the Nusselt number are given.

Table 7.4 Thermal results for grooved channel

ΔT (°K)	quasi-DNS Nu	quasi-DNS HTC
17.8	86	27,070

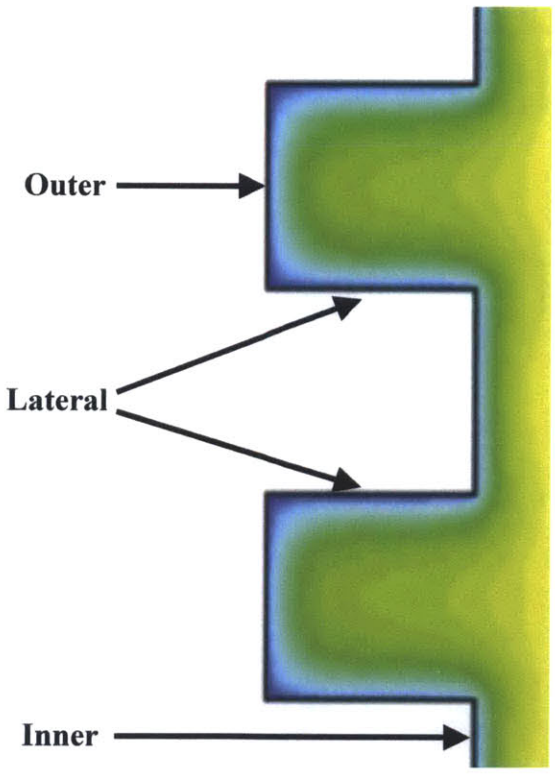

Figure 7.8 Types of walls for grooved channel - zoomed in section from Figure 7.7

The stagnation zones formed in the corners of the grooves (the intersection between the lateral and outer walls in Figure 7.8) locally reduce the heat transfer coefficient considerably as is seen

in Table 7.5. The local heat transfer coefficient on the inner wall is about 4.3 times higher than on the outer wall.

Table 7.5 Thermal comparison between wall types in the grooved channel case

Wall Type	Local HTC	Local Nu
Inner	**43035**	**136**
Lateral	**24717**	**78**
Outer	**10640**	**33**

8. Comparison between Quasi-DNS results of smooth and grooved channels

In this chapter, the quasi-DNS results of the smooth and grooved channels are compared side by side. To investigate more carefully the flow behavior in the vicinity of the grooves, parallel planes to the wall (Figure 8.1) of instantaneous streamwise velocity contours at various y+ location from the wall were obtained (Figure 8.2).

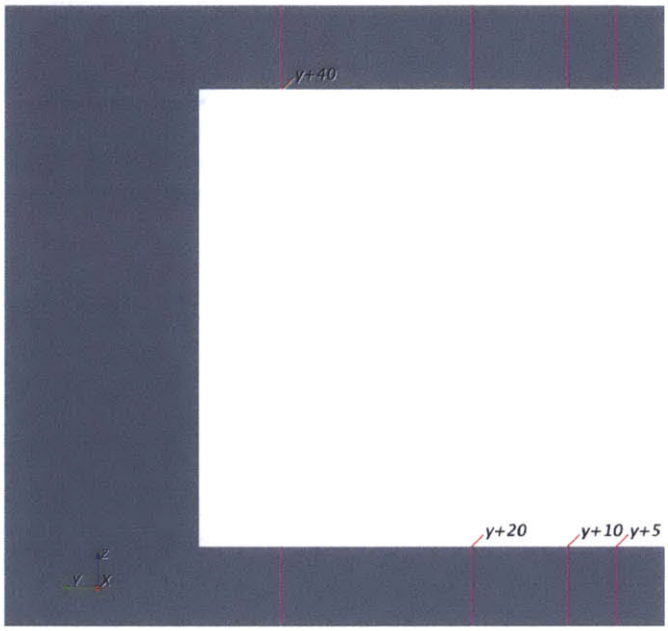

Figure 8.1 Parallel planes from the wall

The grooves, as expected, create smaller turbulent structures inside the flow compared to those in the smooth wall channel case.

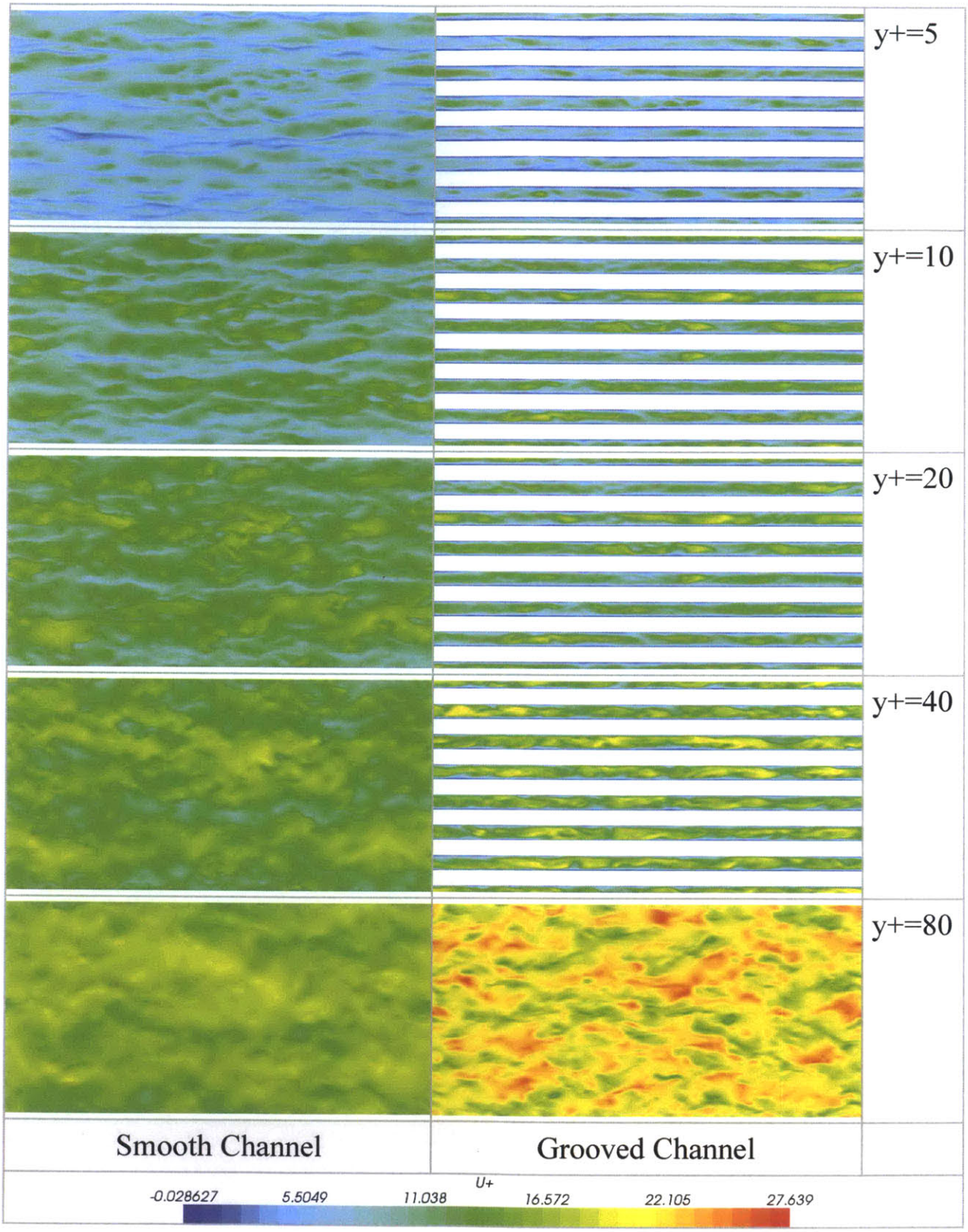

Figure 8.2 Parallel planes to the wall of instantaneous non-dimensional streamwise velocity contours at various y+ locations from the wall

In Table 8.1, relevant geometry values are given. It can be seen that the cross section area was preserved, while the addition of grooves increases the wall surface area by a factor of about 2.3.

Table 8.1 Geometry comparison between smooth and grooved wall cases

Channel Type	Wall Surface Area (m^2)	Cross Section Area (m^2)	Characteristic Length (m)
Smooth	**22.21**	**6.941**	**1.0424**
Grooved	**50.58**	**6.998**	**0.98425**

Table 8.2 Flow comparison between smooth and grooved wall cases

Channel Type	Average Velocity (m/s)	Pressure Drop (Pa)	τ-wall	Skin friction coefficient	Mass flow rate (kg/s)
Smooth	**5.96E-03**	**7.24E-04**	**1.138E-04**	**0.00510**	**41.20**
Grooved	**6.30E-03**	**1.71E-03**	**1.199E-04**	**0.00407**	**44.01**

In the grooved channel case, the skin friction coefficient is smaller than in the smooth case, as can be seen in Table 8.2. Moreover, the pressure drop in the grooved case is higher than in the smooth case as the drag is increased, but mainly because the wall surface area is increased. The pressure drop of the grooved case is about 2.4 times higher than in the smooth case, while the ratio between the wall surface areas of the grooved channel and smooth channel is about 2.3, and the ratio between the wall shear stress of the grooved channel and smooth channel is about 1.05.

Table 8.3 Thermal comparison between smooth and grooved wall cases

Channel Type	Pr	Re	DNS Nu*	ΔT (°K)	quasi-DNS Nu	quasi-DNS HTC
Smooth	**6**	**13,925**	**101**	**15.7**	**103**	**30,700**
Grooved	**6**	**13,920**	**N/A**	**17.8**	**86**	**27,070**

***Kawamura Re=14124, Pr=6**

Also, the Nusselt number and the heat transfer coefficient in the grooved channel case are about 1.2 times lower than in the smooth channel case (Table 8.4).

Based on the increase in the channel pressure drop, and also slight decrease in the local heat transfer coefficient, it can be concluded that the choice for a grooved wall channel instead of a smooth wall channel is not necessarily optimal, particularly if fabrication issues are taken into account or the fact that the grooved walls may promote oxide growth and crud formation during fuel operation.

8. Conclusions and Recommendations

The effect of lateral power distribution of the MITR LEU fuel design was analyzed using Computational Fluid Dynamics code STAR-CCM+. Coupled conduction and convective heat transfer were modeled for uniform and non-uniform lateral power distributions. The most limiting lateral power distribution was obtained from MCODE modeling for MITR core configuration #189EOC. The CFD simulation results are summarized as follows:

a) Due to conduction, the maximum heat flux ratio on cladding surface is 1.16, compared to the maximum volumetric power generation ratio of 1.23. Thermal conduction attributes to a 7% difference between the maximum power generation ratio and maximum heat flux ratio.

b) The maximum cladding temperature occurs roughly 0.5 inches from the edge of the support plate while the peak volumetric power generation is at the end of the fuel meat about 0.1 inches from the edge of the support plate.

c) Although the heat transfer coefficient is lower in the corner of the coolant channel, it has a negligible effect on the peak cladding temperature, i.e. the peak cladding temperature is attributed to heat flux only, and a channel average heat transfer coefficient can be adopted.

d) Coolant temperatures in the radial direction are fairly uniform, which is indicative of good lateral mixing.

The CFD results indicate that when a sub-channel method is adopted for simulation, the coolant temperature rise is overly conservative. For the case of MITR core#189EOC, it is recommended that a 4-stripe model with a hot stripe factor of 1.1 is adopted to reduce the conservatism.

Moreover, a quasi-DNS study was performed to accurately evaluate the effect of the fuel grooves. As expected the grooves lead to an increase in pressure drop, but also, less expectedly the grooves have a considerable influence on the near wall turbulent streak movement, which lead to the formation of low turbulence zones in the corner of the grooves. The latter effect leads to an effective decrease in the heat transfer coefficient locally. Further work could be completed with quasi-DNS to optimize the geometry of the grooves in such a way that a smaller decrease or even increase in the local heat transfer coefficient would become possible. Moreover, this would lead to a more considerable increase in the heat transfer coefficient, which may be significant enough to offset the increase in pressure drop and fabrication issues. For example, triangular grooves or dimples could be used instead of the square grooves.

Given that this study considered only non-conjugate heat transfer from the metal to the fluid, accurate temperature profiles could not be obtained. Consequently, for an analysis of the local temperatures it is recommended that a conjugate heat transfer should be performed under the same conditions.

9. References

[1] The Reduced Enrichment for Research and Test Reactor (RERTR) program http:// www.rertr.anl.gov Argonne National Laboratory, (2012)

[2] Hu, L., G. Kohse, "MITR User's Guide" Rev.1 June, (2008)

[3] Newton, T.H., "Development of a Low Enrichment Uranium Core for the MIT Reactor", PhD Dissertation, Nuclear Science and Engineering Department, MIT, (2006)

[4] Kim,S.J., Y. Ko, L. Hu, "Loss of Flow Analysis of the MIT Research Reactor HEU-LEU Transitional Cores Using RELAP5-3D", proceedings of ICAPP '10, San Diego, CA, USA, June 13-17, (2010)

[5] Wang, Y.D., "Evaluation of the Thermal-Hydraulic Operating Limits of the HEU-LEU Transition Cores for the MIT Research Reactor", MSc Dissertation, Nuclear Science and Engineering Department, MIT, (2009)

[6] Wong, S.,"Friction pressure drop measurements and flow distribution analysis for LEU conversion study of MIT Research Reactor", MSc Dissertation, Nuclear Science and Engineering Department, MIT, (2008)

[7] Ferziger, J.H., M. Peric, "Computational Methods for Fluid Dynamics", Springer, (2001)

[8] Baglietto, E., H. Ninokata, "Anisotropic Eddy Viscosity Modeling for Application in Industrial Engineering Internal Flows", Int. J. Transport Phenomena, 8, (2006)

[9] Kim, S. J., L. Hu, F. Dunn, "Thermal-hydraulic analysis for high enrichment uranium (HEU) and low enrichment uranium (LEU) transitional core conversion of the MIT Research Reactor" Nuclear Technology In Press

[10] STAR-CCM+ User Manual

[11] Shams, A., F. Roelofs, E.M.J. Komen, E. Baglietto, "Optimization of a pebble bed configuration for quasi-direct numerical simulation", Nuclear Engineering and Design 242, 331-340, (2012)

[12] Kasagi, DNS Database of Turbulence and Heat Transfer http://thtlab.jp/index-orig.html

[13] Kawamura, DNS Database of Kawamura Lab http://murasun.me.noda.tus.ac.jp/turbulence/poi/poi.html

[14] Forrest, E., J. Buongiorno, T. McKrell, L. Hu, "Thermal Hydraulic Study of Utilizing Unfinned Plate Fuel in the MITR"

APPENDIX A: MIT LEU Design Dimensions

Table A-1 LEU Element Dimensions [9]

Plate and channel dimensions	HEU	LEU
Fuel plate length (inch)	23	23
Fuel meat length (inch)	22.375	22.375
Fuel plates per assembly	15	18
Full-channels per assembly	14	17
Fuel meat thickness (mil)	30	20
Fuel meat width (inch)	2.082	2.082
Clad thickness (mil)	15	10
Plate to plate pitch, CL to CL (mil)	158	132
Water gap (fin tip-to-tip) (mil)	78	72
Effective channel thickness (mil)	88	82
Finned width (inch)	2.2	2.2
Number of find per plate	220	220
Fin height (mil)	10	10
Fin width (mil)	10	10
Width without meat to side plate (mil)	113	113
Width without fins to side plate (inch)	54	54
Channel width (inch)	2.308	2.308
Side plate thickness (mil)	188	188
Side plate flat-to-flat, outer edge of one side plate to outside of the other side plate (inch)	2.375	2.375
Element flat-to-flat or length of side plate (inch)	2.380	2.380
Actual flow area (m^2)	1.3103E-04	1.2210E-04
Wetted equivalent diameter (m)	2.1887E-03	2.0421E-03
Heated equivalent diameter (m)	2.4778E-03	2.3089E-03

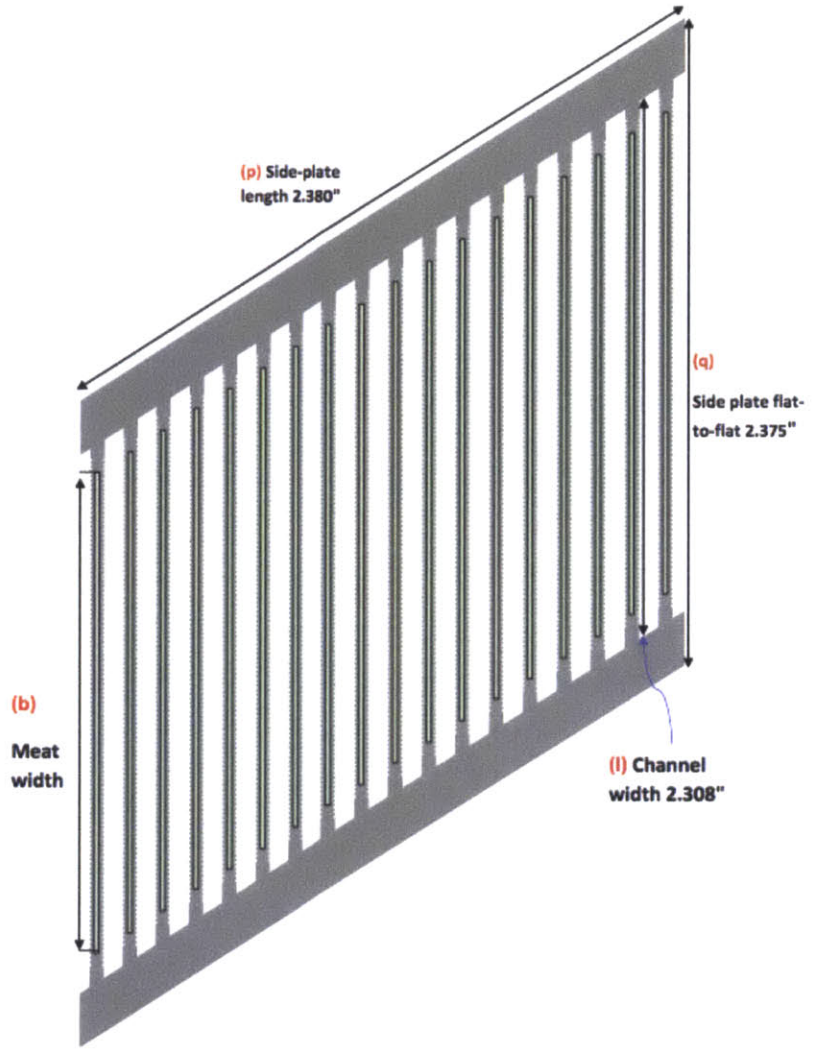

Figure A-1 A schematic of MITR LEU element drawn with 18 fuel plates [9]

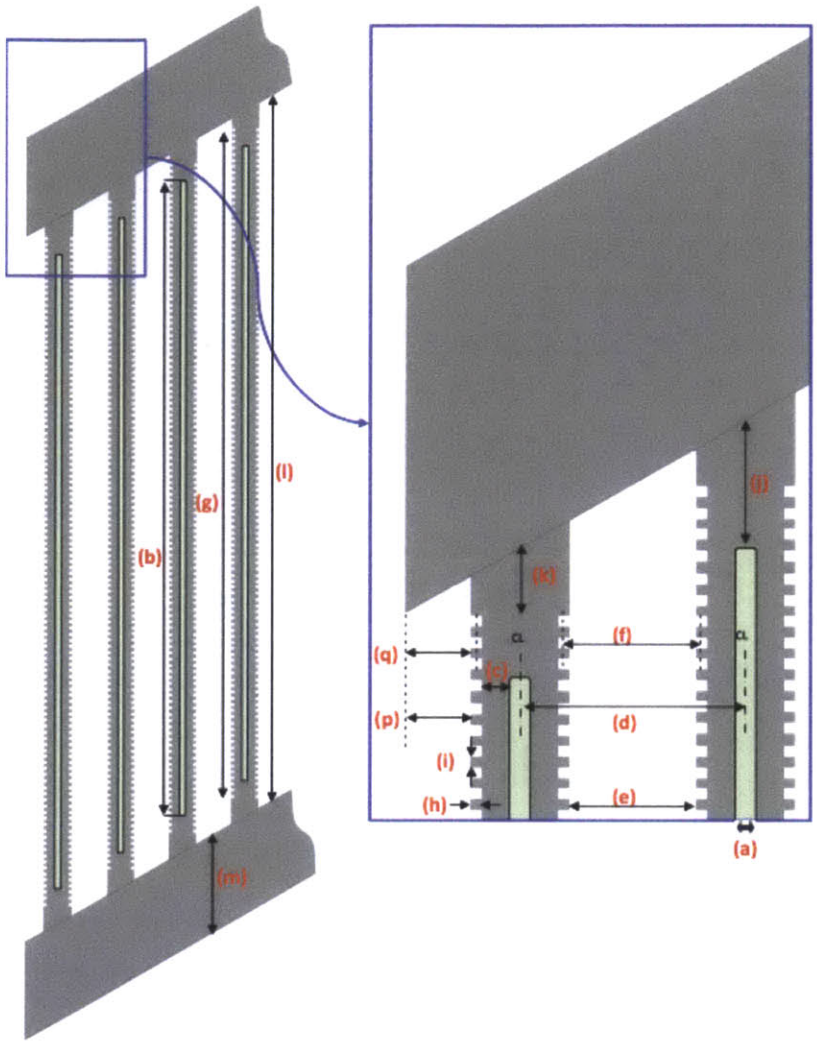

Figure A-2 A schematic of MITR LEU element drawn with 4 fuel plates [9]

APPENDIX B: Material properties

The temperature-dependent material properties used are based on the ones proposed for the LEU design [9].

Table B-1 Fuel properties [9]

Fuel Properties	LEU
Compound form	U-10Mo
Fuel compound density (kg/m^3)	17000
Uranium density (kg/m^3)	15500
Melting point (°C)	1135

The thermal conductivity, specific heat and density of the LEU fuel meat were implemented as field functions based on the data from Table B-2 and Table B-3.

Table B-2 Temperature-dependent thermal conductivity of LEU fuel meat [9]

Temperature (°K)	Thermal conductivity (W/m-K)
293.15	11.3
373.15	13.2
473.15	17.1
593.15	20.3
673.15	23.7
773.15	27.6
893.15	31.9
973.15	35.4
1073.15	37.5

Table B-3 Temperature-dependent specific heat and density of LEU fuel meat [9]

Temperature (°K)	Specific Heat (J/kg-K)	Density (kg/m^3)
273.15	137	17125
373.15	142	16833
473.15	147	16750
593.15	154	16663
673.15	161	16577
773.15	169	16493
893.15	175	16300
973.15	181	16215

Also, the material properties of the Al6061 cladding material used in the model are provided in Table B-4.

Table B-4 Thermal conductivity, specific heat and density of Al6061 cladding [9]

Temperature (°K)	Thermal conductivity (W/m-°K)	Specific Heat (J/kg-°K)	Density (kg/m^3)
373.15	180	896	2700

APPENDIX C: Heat transfer coefficient definition for RELAP

In order to export the heat transfer coefficients from the CFD simulations in a manner consistent with the usage in the RELAP code, the lateral (y) direction is subdivided in 16 separate channels, as shown in Figure C-1. The channels were obtained by splitting the coolant region in 16 equally-sized sections in the y-direction; the sections' exact locations are reported in a separate excel file.

Figure C-1 Channels in the coolant region (only the odd ones are highlighted)

First, the coolant bulk temperature (surface average) for each stripe was computed. The results are given in Table C-1.

Table C-1 Coolant bulk temperature and y-location of each stripe point in Figure 45

Stripe	y-location (in)	T_{bulk}	T_{bulk}
1	**0.378989**	46.848	47.965
2	**0.516489**	50.347	51.616
3	**0.653989**	51.313	52.139

Stripe	y-location (in)	T_{bulk}	T_{bulk}
4	**0.791489**	51.462	51.824
5	**0.928989**	51.484	51.495
6	**1.066489**	51.488	51.250
7	**1.203989**	51.490	51.074
8	**1.341489**	51.491	50.952
9	**1.478989**	51.491	50.875
10	**1.616489**	51.490	50.840
11	**1.753989**	51.488	50.852
12	**1.891489**	51.483	50.920
13	**2.028989**	51.464	51.050
14	**2.166489**	51.327	51.162
15	**2.303989**	50.424	50.571
16	**2.441489**	47.249	47.529

Next, the average cladding temperature and heat flux for each stripe were evaluated. Finally, equation (5) was used for each stripe in order to obtain the heat transfer coefficient, and its values were plotted together with the heat transfer coefficient based on the bulk coolant temperature of the whole channel for both uniform and non-uniform heating distribution cases (Figure 5.39).

The cladding temperatures, heat fluxes and heat transfer coefficients were, respectively, given in Tables C-2, C-3 and C-4.

Table C-2 Cladding temperature for 16-stripe lateral power distribution

Stripe	y-location (in)	T_{clad}	T_{clad}
1	**0.378989**	55.983	58.652
2	**0.516489**	65.183	68.305
3	**0.653989**	67.092	69.050

Stripe	y-location (in)	T_{clad}	T_{clad}
4	**0.791489**	67.411	68.257
5	**0.928989**	67.461	67.479
6	**1.066489**	67.470	66.894
7	**1.203989**	67.473	66.474
8	**1.341489**	67.474	66.182
9	**1.478989**	67.475	65.997
10	**1.616489**	67.473	65.914
11	**1.753989**	67.471	65.943
12	**1.891489**	67.462	66.105
13	**2.028989**	67.414	66.410
14	**2.166489**	67.108	66.695
15	**2.303989**	65.265	65.632
16	**2.441489**	56.151	56.809

Table C-3 Heat flux for 16-stripe lateral power distribution

Stripe	y-location (in)	Heat Flux (W/m^2) - Uniform	Heat Flux (W/m^2) - Non-Uniform
1	**0.378989**	303505	354990
2	**0.516489**	507852	571221
3	**0.653989**	542613	581587
4	**0.791489**	548789	565515
5	**0.928989**	549840	550064
6	**1.066489**	550010	538395
7	**1.203989**	550034	529976
8	**1.341489**	550031	524101

Stripe	y-location (in)	Heat Flux (W/m^2) - Uniform	Heat Flux (W/m^2) - Non-Uniform
9	**1.478989**	550038	520388
10	**1.616489**	550042	518741
11	**1.753989**	550027	519322
12	**1.891489**	549871	522529
13	**2.028989**	548819	528502
14	**2.166489**	542377	533834
15	**2.303989**	505236	512642
16	**2.441489**	289757	301907

Table C-4 Heat transfer coefficient (HTC) for 16-stripe lateral power distribution

Stripe	y-location (in)	HTC - Uniform	HTC - Non-Uniform
1	**0.378989**	33227	33218
2	**0.516489**	34230	34228
3	**0.653989**	34390	34392
4	**0.791489**	34411	34413
5	**0.928989**	34414	34414
6	**1.066489**	34414	34414
7	**1.203989**	34414	34414
8	**1.341489**	34414	34414
9	**1.478989**	34414	34413
10	**1.616489**	34414	34413
11	**1.753989**	34414	34413
12	**1.891489**	34413	34413
13	**2.028989**	34409	34408
14	**2.166489**	34368	34367

Stripe	y-location (in)	HTC - Uniform	HTC - Non-Uniform
15	**2.303989**	34045	34039
16	**2.441489**	32549	32533

APPENDIX D: Vortex Test

A setup of four vortices (Figure D-1) in a 2π by 2π domain was implemented in order to test the energy conservation of various grids. The initial flow conditions are obtained from the following equations:

$$p = -\frac{1}{4}\left[\cos(2x_1) + \cos(2x_2)\right] \tag{D-1}$$

$$u_1 = -\cos(x_1)\cdot\sin(x_2) \tag{D-2}$$

$$u_2 = \sin(x_1)\cdot\cos(x_2) \tag{D-3}$$

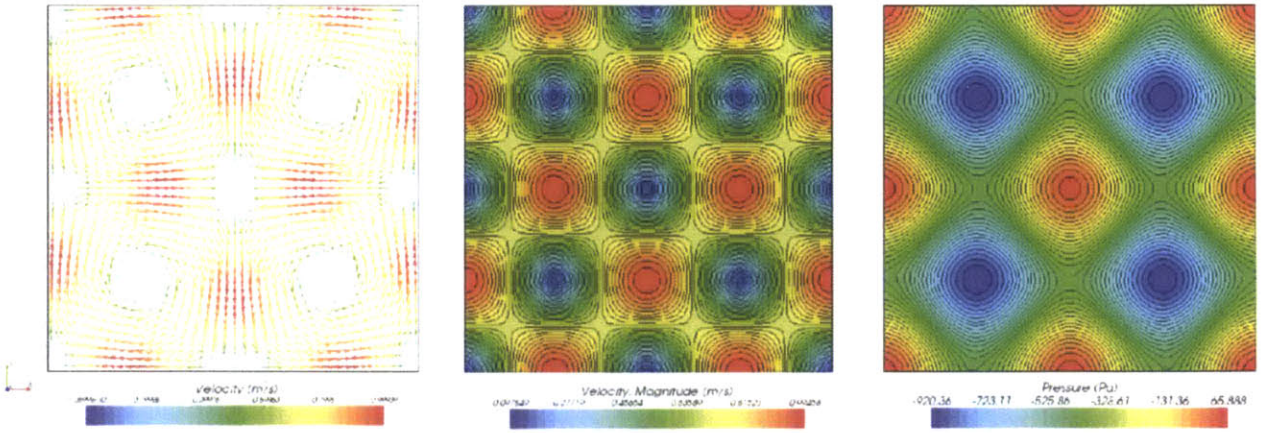

Figure D-1 Initial setup of four vortices (Grid made of 2025 quad cells 2D)

The final results are shown in Figure D-2. We can see that the central differencing scheme of the quad cells gives the best conservation of kinetic energy, followed by central differencing of the tris cells, the second-order upwind of quads and tris, and, the last, first-order upwind of both tris and quad cells.

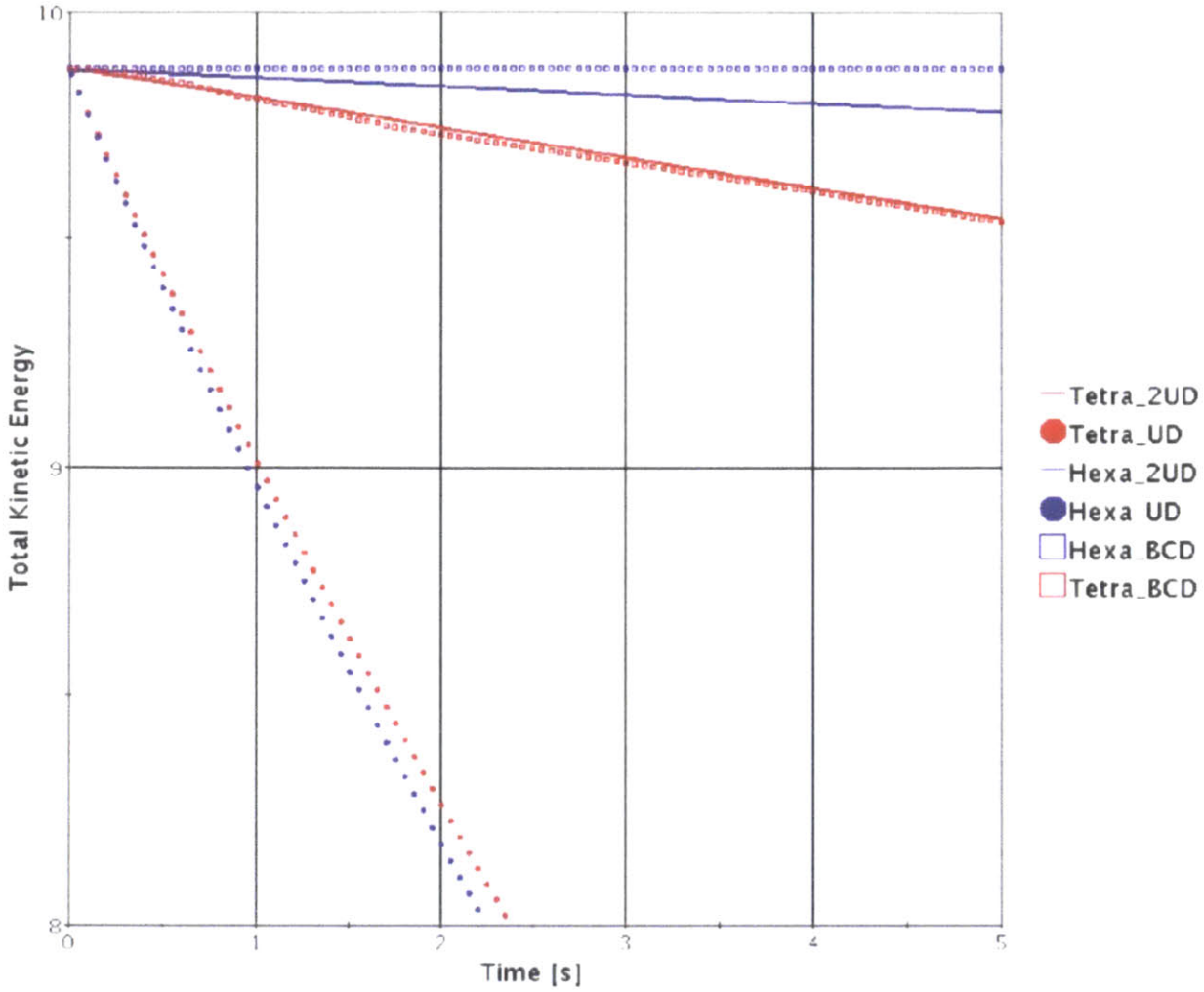

Figure D-2 Results of total kinetic energy dissipation for various grids and convection term discretization schemes